

UNIVERSITY OF BIRMINGHAM

Methane-Gasoline Dual Fuel Engine Combustion and Emissions Control Technologies

By

Ammar Wahbi

A thesis submitted to

The University of Birmingham

for the degree of

DOCTOR OF PHILOSOPY

Department of Mechanical Engineering

School of Engineering

The University of Birmingham

Aug 2022

UNIVERSITY OF
BIRMINGHAM

University of Birmingham Research Archive

e-theses repository

This unpublished thesis/dissertation is copyright of the author and/or third parties. The intellectual property rights of the author or third parties in respect of this work are as defined by The Copyright Designs and Patents Act 1988 or as modified by any successor legislation.

Any use made of information contained in this thesis/dissertation must be in accordance with that legislation and must be properly acknowledged. Further distribution or reproduction in any format is prohibited without the permission of the copyright holder.

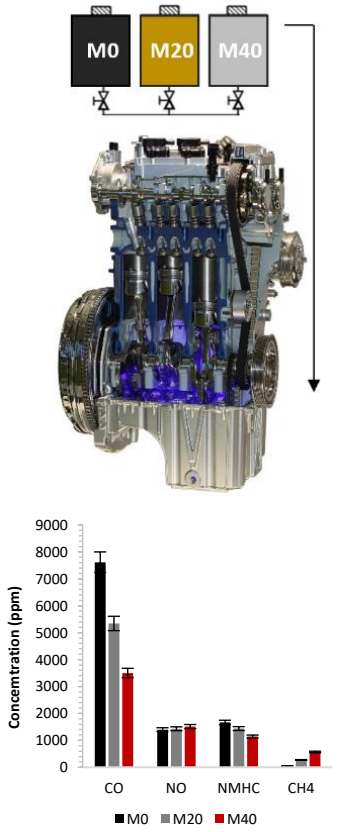
Abstract

Compressed natural gas (CNG) is currently one of the promising and more established alternative to liquid fossil fuels. The combined utilisation of CNG and gasoline in spark-ignition engines can provide strong synergies between the two fuels leading to lower fuel consumption and exhaust emissions. However, no study to date has investigated the performance of the aftertreatment system designed for dual-fuel engines, with all studies either limited to combustion analysis of the dual-fuel or for dedicated CNG fuelled engines.

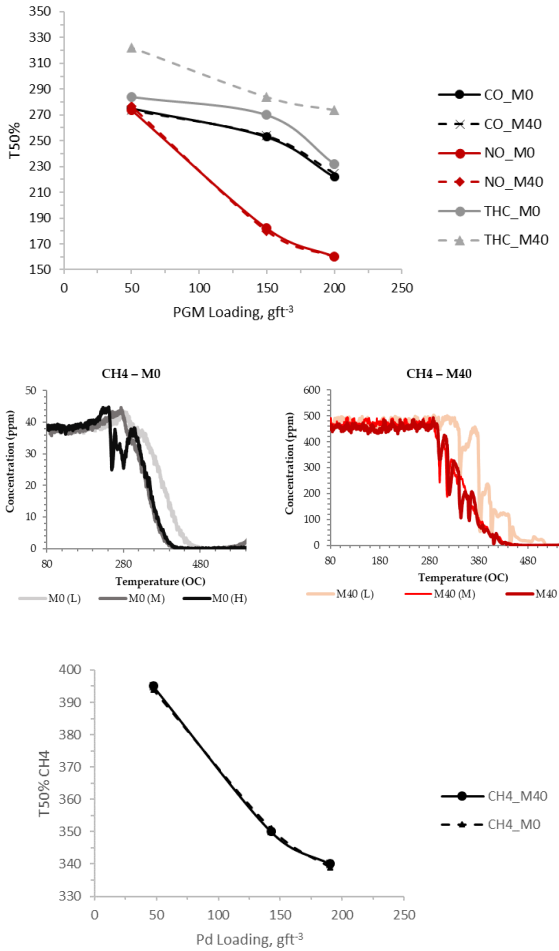
As such, the aftertreatment system of a dual-fuel gasoline-CNG engine is investigated in this study by the use of several dedicated CNG catalysts. A dual-fuel injection strategy was implemented where methane gas was port-injected into the intake in stoichiometric conditions at levels corresponding to 20 and 40% energy density replacement of gasoline. High, medium and low loaded Pd/Rh catalysts were used and compared to study the effect of PGM loading on the catalyst light-off activity for methane. Results indicate that increasing the Pd loading led to significantly earlier light-off temperatures achieved at relatively lower temperatures of 340, 350 and 395ºC respectively. However, the benefit diminishes above Pd loading >142.5 g ft^{-3}. To complement this work, the performance of two full-scale CNG catalysts with different PGM loadings under various engine lambda conditions and cyclic air/fuel ratio was investigated. In addition, cycles have been developed with the aim to enhance fuel economy while reducing exhaust emissions. Additional research into the usage of the dual-fuel injection system to reduce the higher particulate emissions produced by GDI engines, as well as reducing their gaseous exhaust emissions is included in the study. Various characteristics of the released particles, including their size distributions, reactivity, morphology, and nanostructure, were evaluated. Other benefits of the dual-fuel system are presented in this study in terms of 10% and 54% lower engine output CO_2 and CO emissions respectively and up to 90 to 98% reduction in particle number. However, high NH_3 levels were observed primarily formed from steam-reforming reactions due to the increased level of methane in the exhaust stream.

Graphical Abstract

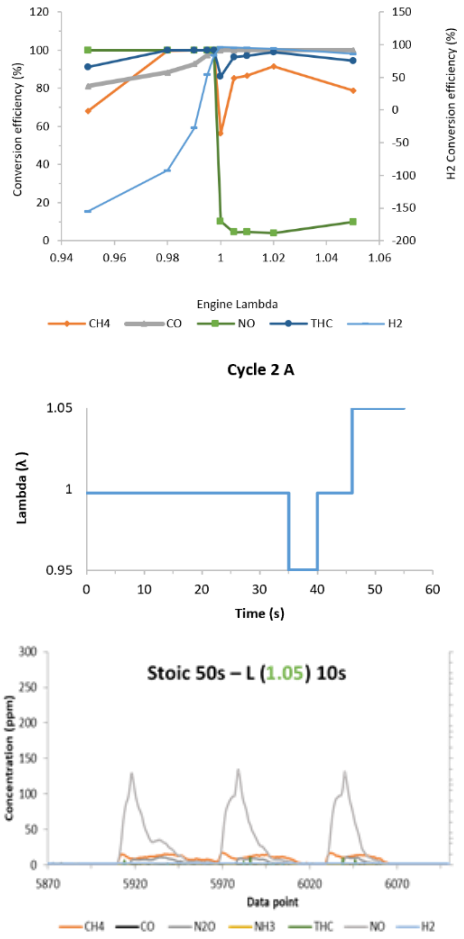
1 Dual-Fuel Combustion



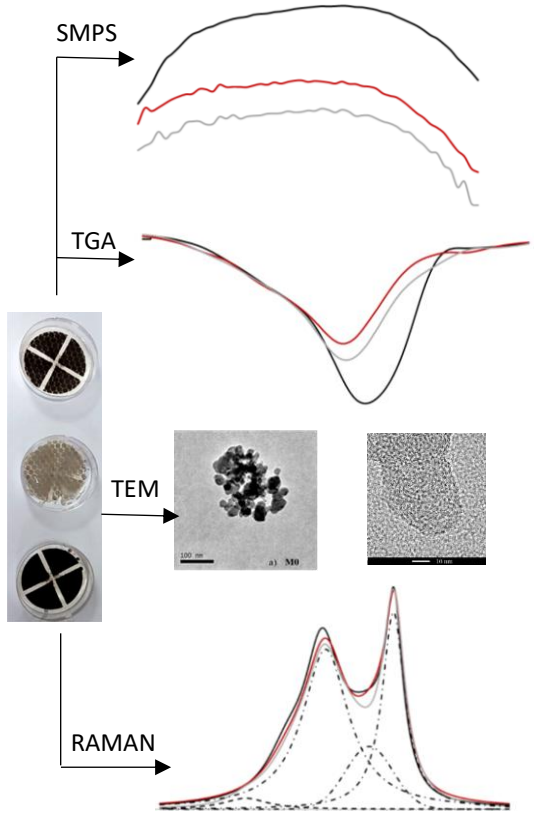
2 Impact of PGM content



3 Full-Scale Aftertreatment system



4 PM Characterisation



Acknowledgements

Here we go! 4 years (and COVID-19) later…

I would first like to express my immense gratitude to my lead supervisor Prof. Thanos Tsolakis for this opportunity and for his guidance and supervision of the research work. Thank you Thanos, as I not only have a Thesis to show for my time as a researcher, but also a number of consultancy projects from which I gained valuable experience. You helped pave the way for me, and I will be eternally grateful. I would also like to extend this gratitude to my co-supervisor Dr. Jose Martin Herreros for his invaluable technical input, feedback, guidance and constant support throughout this work. You are truly exceptional and generous, qualities I admire about you.

Thanks to the University of Birmingham and School of Engineering for awarding me the Postgraduate Scholarship for the duration of my PhD and for the Institution of Mechanical Engineers for their financial support. I am also grateful for Johnson Matthey for funding my research and for the JM team especially my supervisors, Dr. Paul Millington and Dr. Agnes Raj for their support and knowledge that guided this work, and for the materials provided in this Thesis. Special thanks to Dr. Francisco Martos and Dr. Soheil Zeraati Rezaei for their technical support and to all my colleagues Dr. Omid Doustdar, Dr. Cruz Hergueta, Dr. Nahil Serhan, Dr. Hadi Nozari, Dr. Jun Chan and soon-to-be Dr. Sak Sittichompoo for all the good and bad times we endured together. It is an honour to close this chapter of my life among such brilliant scholars.

Finally, I want to say a huge thank you to my mom, my life-mentor, and my rock, Mai Shahin. You gave your life selflessly so that your children would have a better future, and I pray that we are living up to your expectations. Your strength is an inspiration and I hope to become half the parent you are. To my family, my brothers Ali, Yasir, Salih, Ahmed and to my father, thank you all for being there for me. It was a trying time for all of us, so take pride in what you achieved, the sky is your limit. Also shout-out to Ali for making me an Uncle to baby-Saif! To my other-half and fiancée Zina Mohamed, thank you for all your love and support and for keeping me sane over the past years. A heartfelt "thank you" for sticking by me through the hard times.

Table of Contents

Abstract ..... **i**

Graphical Abstract ..... **ii**

Acknowledgements ..... **iii**

Table of Contents ..... **iv**

List of Figures ..... **viii**

List of Tables ..... **xi**

Nomenclature ..... **xii**

1. Introduction **1**

1.1. Overview 1

1.2. PhD Aim and Objectives 4

1.3. Thesis Outline 5

2. Literature Review **7**

2.1. Overview of Natural Gas (methane) Engines 7

2.1.1. Natural Gas as an Alternative Fuel 7

2.1.2. Combustion and Emissions of Natural Gas SI Engines. 10

2.1.3. Dual-Fuel NG-Gasoline Engines 12

2.2. Current NG Emission Control Technologies in SI Engines 16

2.2.1. Lean-burn vs Stoichiometric Natural Gas Engines 16

2.2.2. Exhaust Gas Recirculation 17

2.2.3. Spark Timing 18

2.2.4. Hydrogen Enriched Natural Gas Engines 18

2.2.5. Aftertreatment System 20

2.3. Particulate Matter Characterisation 27
2.3.1. Particle Size Distribution 28
2.3.2. PM Oxidation 30
2.3.3. PM Nanostructure and Morphology 30
3. Experimental Setup and Methodology 36
3.1. Four-Cylinder Engine Test Bench 36
3.2. Three-Cylinder Engine Test Bench 38
3.3. Fuels Used 39
3.4. Gaseous and Particulate Emission Analysers 39
3.4.1. FTIR 39
3.4.2. SMPS 40
3.4.3. TGA 41
3.4.4. RAMAN 42
3.4.5. TEM/HRTEM 43
3.5. Catalyst Cores 44
4. Performance of Different Loaded PGM Catalysts for Dual-Fuel Engines 45
4.1. Introduction 45
4.2. Experimental Procedure 45
4.3. Results and Discussion 47
4.3.1. Combustion Studies 47
4.3.2. Emissions Upstream the Catalysts 49
4.3.3. Impact of PGM ratio and Methane Replacement on Catalytic Activity 51
4.4. Summary 60

5. Full-Scale Aftertreatment Technologies for Dual-Fuel Engines 61

5.1. Introduction 61

5.2. Experimental Procedure 62

5.3. Results and Discussion 66

5.3.1. Emissions Upstream the Catalyst 66

5.3.2. Catalyst Efficiency – Comparison of Different PGM Loaded Catalysts 67

5.3.3. Effect of Air/Fuel Variation on Catalyst Performance 70

5.3.4. Effect of Cyclic Lambda Variation on Emissions and Fuel Economy 77

5.4. Summary 84

6. Impact of Dual-Fuel Methane-Gasoline Combustion on PM Emissions 85

6.1. Introduction 85

6.2. Experimental Procedure 85

6.3. Results and Discussion 87

6.3.1. Engine Combustion and Gaseous Emissions 87

6.3.2. Particle Size Distribution 89

6.3.3. Soot Oxidative Reactivity (TGA) 90

6.3.4. Particle Morphology Analysis 92

6.3.5. Primary Particle Nanostructure Analysis 97

6.3.6. Raman Spectroscopy 99

6.4. Summary 101

7. Conclusion and Future Work 103

7.1. Conclusion 103

7.2. Future Work 105

Appendix 1: Publications, Projects and Awards **106**

References **108**

List of Figures

Figure 1.1: World's consumption by type of energy source. 1

Figure 1.2: a) Global natural gas reserves (tcm), b) Regional production share of natural gas. Reproduced from [3,4]. 3

Figure 1.3: Result Chapters. 6

Figure 2.1: A detailed composition of natural gas. Reproduced from [5]. 8

Figure 2.2: Performance of an aged Pd:Rh TWC at 450 ^{o}C as a function of lambda on: a) Stoichiometric Gasoline engine, b) Stoichiometric NG engine [35]. 21

Figure 2.3: Typical engine exhaust size distribution. 28

Figure 2.4: Particle size distribution for different injection configurations, adapted from [16]. 29

Figure 2.5: Typical morphological parameters associated with soot particles 31

Figure 2.6: TEM images showing particles collected from Diesel and CNG dual fuelling. 32

Figure 2.7: Physical nanostructure parameters (adapted from Gaddam et al. [19]) 33

Figure 2.8: HRTEM image of soot collected from dual-fuel combustion with 70% CNG. Adapted from [18]. 34

Figure 2.9: Typical Raman spectrum representative of gasoline soot. 35

Figure 3.1: 4-cylinder GDI engine test bench. 37

Figure 3.2: Three-cylinder gasoline DI/PFI engine test bench. 38

Figure 3.3: MultiGas FTIR 2100 MKS analyser. 40

Figure 3.4: Scanning Mobility Particle Sizer (SMPS) 3969. 41

Figure 3.5: Perkin Elmer Pyris 1 TGA analyser. 41

Figure 3.6: Renishaw inVia confocal Raman microscope. 43

Figure 3.7: JEOL JEM-2100 Electron Microscope. 43

Figure 3.8: Full scale catalysts used in this research 44

Figure 4.1: Engine apparatus, testing and analysis schematic. 46

Figure 4.2: Tubular furnace and reactor used in the experiments. 47

Figure 4.3: Corresponding in-cylinder pressure and HRR for M0, M20 and M40 test conditions. 48

Figure 4.4: Engine-out emissions with different methane % replacement. 50

Figure 4.5: Catalyst light-off activity for regulated emissions for M0 and M40. 52

Figure 4.6: Regulated emissions light-off temperature vs PGM loading. 53

Figure 4.7: Light-off activity of CH_4 for M0 and M40 at different PGM loadings. 54

Figure 4.8: CH_4 light-off temperature vs Pd loading. 55

Figure 4.9: NMHC light-off activity for M0 and M40: a) High PGM, b) Med PGM and c) Low PGM. 56

Figure 4.10: Ammonia slippage and by-products for M0 and M40: a) High PGM, b) Med PGM, c) Low PGM. 58

Figure 5.1: Experimental setup. 62

Figure 5.2: Stoichiometric to Lean/Rich cycle duration and ratio. 64

Figure 5.3: Combined Stoichiometric-Rich-Lean cycle for fuel efficiency. 65

Figure 5.4: Exhaust concentration upstream the catalyst as a function of engine lambda for M40. 66

Figure 5.5: Pd-Rh Catalyst: Oxidation performance as a function of engine lambda. 67

Figure 5.6 Pt-Rh Catalyst: Oxidation performance as a function of engine lambda. 69

Figure 5.7: M40 engine-out emissions under Stoic to Lean lambda cycle. 70

Figure 5.8: Effect of Stoic to Lean cycle on Cat A for M40 71

Figure 5.9: Comparison between M0 and M40 fuelling conditions for Cat B. 72

Figure 5.10: Effect of Stoic to Lean cycle on Cat B for M40. 73

Figure 5.11: M40 engine-out emissions under Stoic to Rich lambda cycle. 74

Figure 5.12: Effect of Stoic to Rich cycle on Cat A for M40. 75

Figure 5.13: Effect of Stoic to Rich cycle on Cat B for M40. 76

Figure 5.14: Comparison between M0 and M40 fuelling conditions for Cat B. 76

Figure 5.15: Effect of test cycles on catalyst-A performance; a) Cycle 1, b) Cycle 2. 79

Figure 5.16: Effect of test cycles on catalyst-A performance; a) Cycle 3, b) Cycle 4. 80

Figure 5.17: Fuel flow profile highlighting the effect of switching between different lambda states. 81

Figure 5.18: a) Engine-out emissions, b) Effect of cycle 5 on post-catalyst-A emissions. 82

Figure 5.19: Effect of cycle on post-catalyst-B emissions using a) M40 fuelling, b) M0 fuelling. 83

Figure 6.1: Experimental apparatus. 86

Figure 6.2: Loaded soot filters for M0, M40 and M20 respectively. 86

Figure 6.3: Engine-out emissions resulted from the different methane % replacement 88

Figure 6.4: SMPS measurements of particle size distribution. 89

Figure 6.5: Mass profile and weight loss rate of the collected soot samples. 90

Figure 6.6: Impact of the fuelling condition on soot activation energy. 92

Figure 6.7: TEM micrographs collected from a-b.) M0, c-d.) M20 and e-f.) M40. 93

Figure 6.8: Log-normal primary particle distribution for M0, M20 and M40 cases. 94

Figure 6.9: Data count for the respective morphological parameters with M0, M20 and M40. 96

Figure 6.10: HR-TEM micrographs of primary particle nano-structure: a) M0, b) M20, and c) M40. 97

Figure 6.11: Associated nanostructure parameters of the three samples a) fringe separation distance, d002 b) Tortuosity, Tf and c) Fringe length, La. 98

Figure 6.12: Average Raman spectrum representative for each fuelling condition. 101

List of Tables

Table 1.1: The European emission standards for heavy-duty Gas engines..... 3

Table 2.1: Typical physiochemical properties of natural gas, gasoline and diesel fuels [5]..... 9

Table 2.2: Combustion properties of hydrogen [33]..... 19

Table 3.1: 4-cylinder GDI engine specification..... 37

Table 3.2: GDI Engine specifications and associated apparatus..... 38

Table 3.3: Fuel properties for gasoline and methane gas..... 39

Table 3.4: TGA defined program..... 42

Table 3.5: Catalyst specifications 44

Table 4.1: Engine parameters for the different CNG replacements..... 49

Table 5.1: CNG catalyst specifications and their PGM loading 63

Table 5.2: Cycle tests showing ratio of stoic, lean and rich used and fuel efficiency for each case. 77

Table 6.1: Combustion data resulted from different methane replacement. 88

Table 6.2: Start of oxidation, MMLRT and elemental soot fraction of the different samples..... 91

Table 6.3: Statistical normality of distribution 95

Table 6.4: Median values of the nano structural parameters for the different fuelling conditions.. 98

Table 6.5: Representative Raman spectra fittings for each fuel condition. 99

Nomenclature

AFR	Air Fuel Ratio
aTDC	After Top Dead Centre
ATI	Accurate technologies
BMEP	Break Mean Effective Pressure
BSFC	Break Specific Fuel Consumption
bTDC	Before Top Dead Centre
BTE	Brake thermal efficiency
CAD	Crank angle degree
Ce	Ceria
CH_4	Methane Gas
CNG	Compressed Natural Gas
CO	Carbon Monoxide
CO_2	Carbon Dioxide
COV	Coefficient of Variance
CPC	Condensation Particle Counter
d	distance between the ends of the fringe length
d_{002}	Interlayer Spacing

DAQ	Data acquisition
D_f	Fractal Dimension
DI	Direct Injection
DMA	Differential mobility analyser
d_{p0}	Primary particle diameter
DPF	Diesel Particulate Filter
E_a	Activation energy
EGR	Exhaust Gas Recirculation
FTIR	Fourier Transform Infrared
FWHM	Full width at half-maximum
G	Gaussian
GDI	Gasoline Direct Injection
GPF	Gasoline Particulate Filter
H/C	Hydrogen to carbon ratio
HCs	Hydrocarbons
HEGO	Heated exhaust gas oxygen
HRTEM	High Resolution Transmission Electron Microscope
IMEP	Indicated Mean Effective Pressure

L_a	Crystallite width
L_c	Crystallite height
LHV	Lower heat value
m	Sample mass
MEP	Mean effective pressure
NG	Natural Gas
NEDC	New European Driving Cycle
NMHC	Non-methane hydrocarbons
NO_2	Nitrogen dioxide
NOx	Nitrogen Oxides
n_p	Number of primary particles
O_2	Oxygen
p_{02}	Oxygen partial pressure
PAHs	Polyaromatic Hydrocarbons
Pd	Palladium
PFI	Port Fuel Injection
PGM	Platinum group metals
PM	Particulate Matter

PN	Particulate Number
PSD	Particle Size Distribution
Pt	Platinum
r	Oxygen reaction order
R	Universal Gas Constant
R_g	Radius of gyration
Rh	Rhodium
RON	Research Octane Number
SMPS	Scanning Mobility Particle Sizer
SPSS	Statistical Package for Social Sciences
TEM	Transmission Electron Microscope
TGA	Thermogravimetric analysis
THC	Total hydrocarbons
TWC	Three Way Catalyst
VE	Volumetric efficiency
VOC	Volatile Organic Compounds
WGS	Water gas shift
WLTC	Worldwide harmonised light vehicle test procedure

Greek Characters

κ	Number of layers per stack
λ	lambda
τ	Tortuosity
ϕ	Diameter

1. Introduction

1.1. Overview

Despite technological advancements, there is rising concern over environmental pollution in recent years, with the transportation sector being a major contributor of emitted pollutants and greenhouse gases. Carbon dioxide (CO_2), unburned hydrocarbons (HC), oxides of nitrogen (NOx), ammonia (NH_3) and particulate matter emissions (PM) are all by-products of burning fossil fuel. Since their release into the atmosphere has a negative effect on global warming and people's health, stricter regulations have been put in place to limit these harmful car emissions. To that end, the auto industry is constantly researching and rapidly developing new emission control technologies that not only meet the rigorous emission standards introduced worldwide such as that set by the Environmental Protection Agency (EPA), and the EURO 6 standards but also exceed these standards, thereby satisfying consumer demands for reduced fuel consumption and increased power and manoeuvrability.

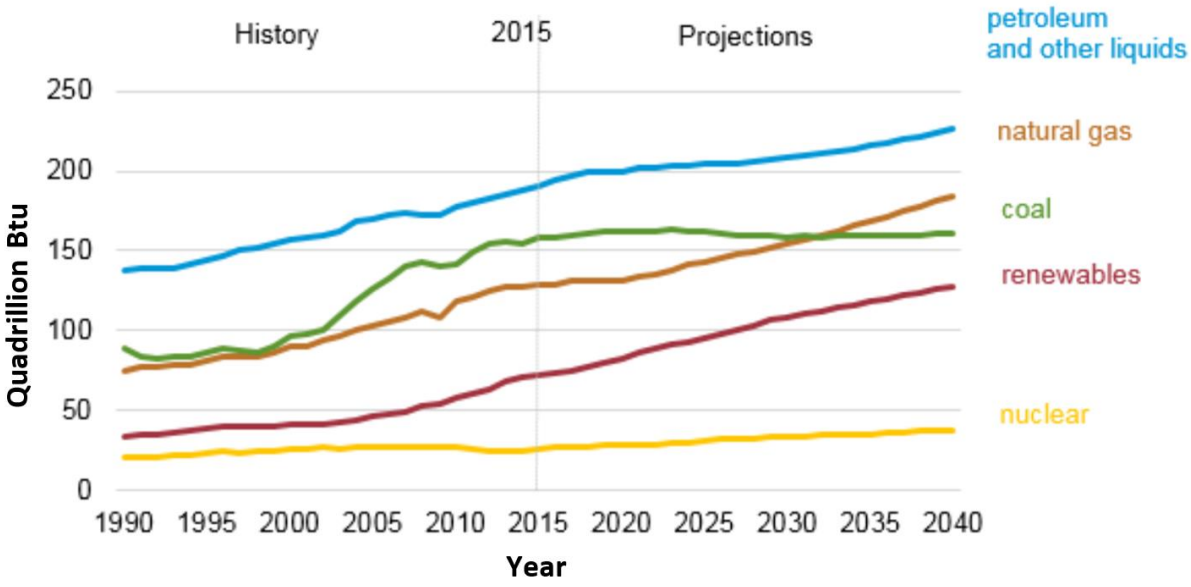


Figure 1.1: World's consumption by type of energy source.

Despite the environmental deterioration and global warming effect caused by the burning of fossil fuels, their use is projected to account for 77% of energy utilisation in 2040 (Figure 1.1)Figure **1.1** [1]. Thus, in the last decade, there has been a rise in the popularity of gaseous and alternative fuels for use in internal combustion engines due to their lower exhaust emissions. It is possible that natural gas will

play a pivotal role in the global shift to cleaner energy sources. The world's consumption of natural gas (NG) is expected to increase by 1.4% annually, making it the only fossil fuel whose share of primary energy consumption is expected to grow [1, 4].

Figure **1.2** displays the abundant proved reserves and increased production of NG, which contribute to its rising popularity and position as a strong alternative to liquid fuels. Globally there were 186.6 thousand cubic meters (tcm) of proven NG reserves in 2016, an increase of 19.2% from 2004 levels, which is sufficient to meet more than 50 years of current global production of NG. By region, Middle-East leads the proved reserves followed by Europe with 30% of the total reserve shares while Europe has the highest global production shares commanding up to 28.2%. Low carbon economy maps are set out worldwide. For instance, the European Commission has proposed a low-carbon economy road map with the goal of reducing greenhouse gas emissions in the transportation sector by more than 60% by 2050 compared to 1990 levels [2]. Using NG as vehicle fuel can contribute to meeting this goal. The Euro 5 and Euro 6 emissions standards for Diesel and Gas engines studied on a transient test cycle are detailed in Table 1.1. The new Euro VId emission standards for heavy-duty vehicles led to a 77% decrease in NOx emissions compared to the previous Euro V standards. Methane emission from NG engines was reduced by 55%, while non-methane HCs were reduced by 71%; therefore, methane emission control after treatment devices will be necessary if natural gas vehicles are to meet both limits. The current Euro VI emission standard additionally introduced a particle number limit for the first time, and decreased the particle mass limit by 67% (not applicable for gas fuelled engines).

The introduction of new engine technologies and after-treatment systems, or a combination of the two, will be necessary for automakers to conform to these global regulations and ensure the lowest emissions possible, even in the most extreme driving conditions. In the following sections, engine combustion and performance of natural gas in spark ignition engines is reviewed. In addition, an analysis of the exhaust products emitted from these engines and the various engine technologies and after-treatment systems currently used to control them are described.

Table 1.1: The European emission standards for heavy-duty Gas engines.

Emission limits (g kWh^{-1})	Euro V	Euro VId
CO	4.0	4.0
NOx	2.0	0.46
NMHC	0.55	0.16
CH_4	1.1	0.5
PM	0.03	0.01
PN (#/kWh^{-1})	-	$6.0x10^{11}$
Test Cycle	European Transient Cycle	World Harmonised Transient Cycle

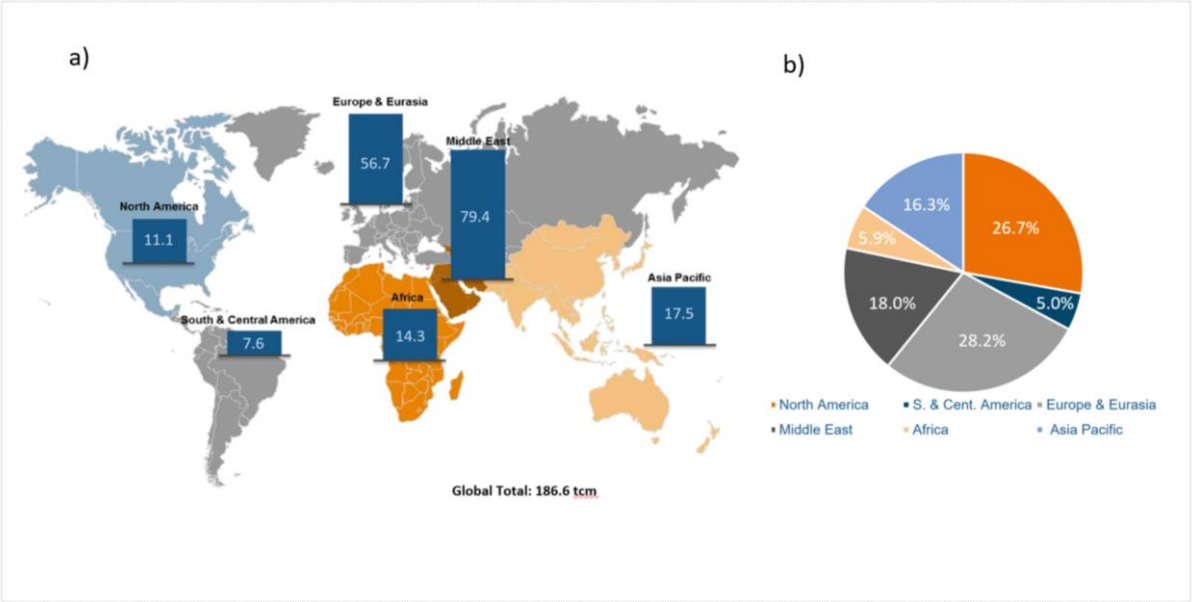


Figure 1.2: a) Global natural gas reserves (tcm), b) Regional production share of natural gas. Reproduced from [3,4].

1.2. PhD Aim and Objectives

The aim of this research is to enhance the catalytic activity through the discovery of synergies between novel combustion modes and catalyst design in unconventional IC engines fuelled with methane. A comprehensive investigation on the effect of methane-gasoline dual fuelling in a GDI engine on combustion and gaseous emissions and the subsequent performance of several catalytic after-treatment technologies will be conducted. In addition, the physico-chemical properties, in terms of nanostructure and morphology, and quantity of the particulate matter (PM) emitted from the dual fuel combustion will also be investigated. The work presented will act as a benchmark for guiding further aftertreatment system design and improvement for dual fuelled Natural gas - Gasoline engines.

In order to meet this aim, natural gas dual-fuel injection and several catalytic after-treatment systems will be developed, and the following research objectives will be carried out:

1. Study the effect of different gasoline/methane blends and operating parameters on engine combustion, fuel consumption and engine-out emissions.
2. Investigate the performance of different PGM-loaded CNG catalysts in reducing exhaust gas emissions under different engine fuelling conditions and stoichiometric combustion
3. Investigate the effect of cyclic lambda variation on the performance of two full-scale CNG catalysts and their oxygen storage capacity and the subsequent effect on fuel economy to aid in further catalyst design optimisation.
4. Quantify the nanostructure, morphology and oxidative reactivity of the PM produced with methane/gasoline GDI engine combustion using various characterisation techniques such as Raman, TGA, TEM and SMPS.

1.3. Thesis Outline

This thesis comprises seven different chapters and a summary of the content and research objectives of each chapter is briefly outlined below:

Chapter 2 provides a concise overview of combustion and emission characteristics of dual-fuel natural gas - gasoline direct injection engine technology. This is followed by an overview of the after treatment system of natural gas and the performance of various oxidation catalysts with a particular attention on the impact of precious group metal loading and ratio on emission abatement. Finally, a review of particulate matter emitted by GDI and NG engines and characterisation techniques used was carried out.

Chapter 3 details the experimental facilities used in this research in terms of the different engine test rigs, data acquisition instrumentation, fuel properties, gaseous and PM emission analysers and catalyst specifications.

In **Chapter 4,** the main challenges of the dual-fuel strategy in terms of methane abatement in the aftertreatment system is addressed by the use of novel CNG catalysts. The study aims to enhance the catalytic activity through the discovery of synergies between novel combustion modes and catalyst design in IC engines fuelled with methane. High, medium and low loaded Pd/Rh catalysts were used and compared to study the effect of PGM loading on the catalyst light-off activity for methane. Ammonia slippage resulted from the novel CNG catalysts were analysed and examined.

In **Chapter 5,** the performance of Pd and Pt catalysts in reducing CH_4 emissions under different engine lambda conditions is analysed and compared to assess the feasibility of interchanging Pt and Pd in the aftertreatment system of CNG and gasoline vehicles. In addition, catalyst analysis study is extended to include their performance under different driving conditions, alternating from stoic to lean and stoic to rich. Finally, air/fuel cycles were developed to improve the engine's fuel economy while keeping tailpipe emissions to a minimum.

In **Chapter 6**, several spectroscopy techniques were utilised to characterise the PM emitted from the dual-fuel combustion. Three different gasoline-to-methane percentage replacement were used to obtain

soot samples. Size distributions, reactivity, morphology, and nanostructure of the collected particle samples were analysed and compared to understand the effect of methane addition on the PM oxidative reactivity and its impact on the different morphological and nanostructure parameters. The findings of this chapter are intended to stimulate further development of dual-fuelling strategies using natural gas and to provide insight into the performance of the produced particles and gaseous emissions in aftertreatment systems.

Chapter 7 summarises the main findings and conclusions of the research and suggests recommendations for further development of dual-fuel NG-GDI technology and its aftertreatment system.

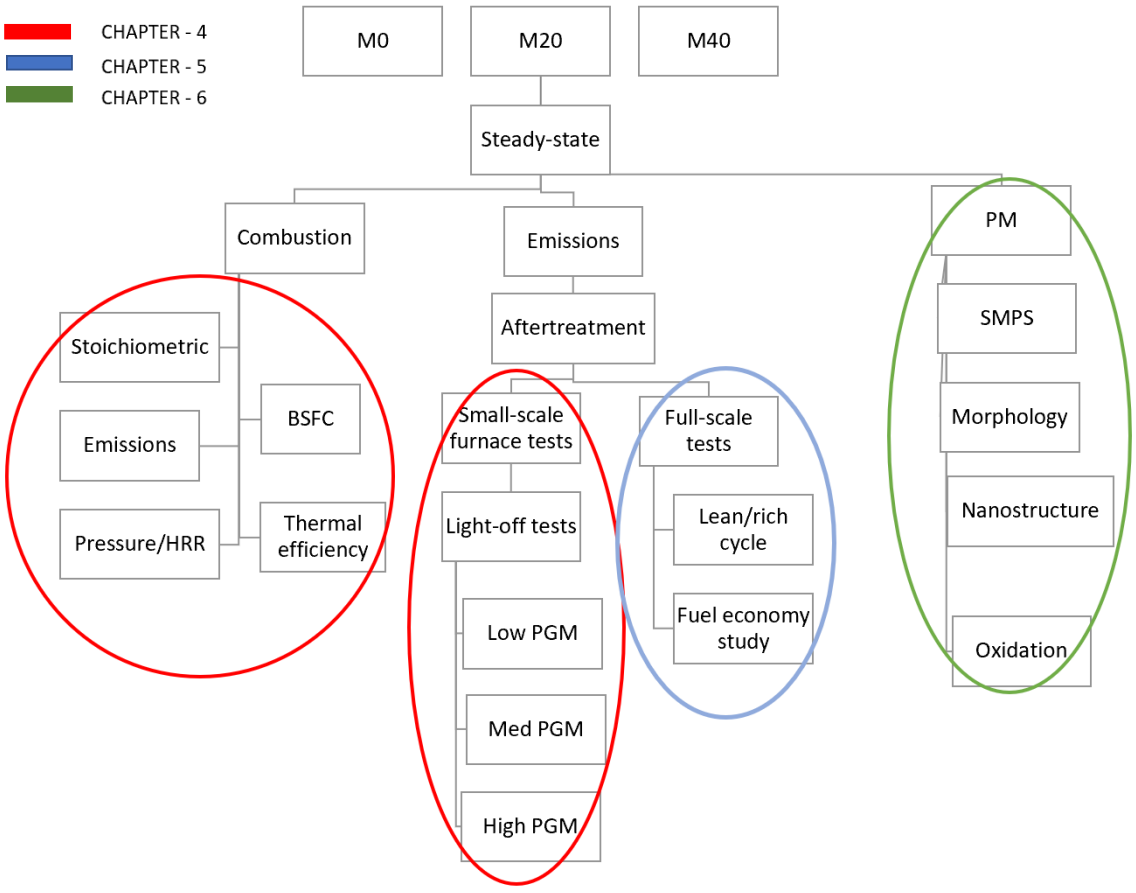


Figure 1.3: Result Chapters.

2. Literature Review

2.1. Overview of Natural Gas (methane) Engines

2.1.1. Natural Gas as an Alternative Fuel

In recent decades, gasoline-powered spark-ignition engines have become the standard power source for automobiles. SI engines have relatively high thermal efficiency and good fuel economy, however the atomization and mixing condition of gasoline limits these characteristics to a certain extent. In addition, as a result of the increasingly strict emission regulations and severe air pollution, regulating emissions from gasoline SI engines has become a major challenge. The most recent emission regulations places significant restrictions on the size and mass of the particles that can be emitted from SI engines making this an urgent problem to be handled. This highlights the critical requirement for SI engines to employ novel technology to reduce exhaust emissions, improve thermal efficiency and reduce fuel consumption.

Recent years have seen a surge in interest in the dual-fuel mode strategy that uses alternative fuels such as alcohols [5,6], hydrogen [9], and natural gas [10]. It is one of the most successful techniques to improve energy savings and pollution reduction in small internal combustion engines. Natural gas, thanks to its superior fuel properties, developed technical process, and low cost, is widely recognised as the best developed alternative fuel for cars [9], [10]. When compared to coal and petroleum, natural gas is considered a cleaner energy source due to its lower CO_2 emissions per unit of energy produced during combustion (by 20-30%) [5,13,14]. This is mainly due to the composition of natural gas with methane being its main constituent (typically 70-90%), leading to a low C/H ratio (1/4). Figure 2.1 provides a representative breakdown of the individual components that make up natural gas. Emissions from natural gas engines do not include harmful by-products like aldehydes and aromatics since the fuel is low in carbon content. This has significant implications for lowering emissions overall, but especially particulate emissions [13]. The high octane number of natural gas suppresses engine knock and enhances the performance of the engine [13]. In addition, natural gas, does not need to be atomized or evaporated before use, making it easier to mix with air and enhancing the efficiency of the

combustion process [14], [15]. Natural gas also outperforms gasoline in its lean burn limit, which is an important quality. When operating in lean combustion settings, gasoline fails to ignite due to uneven mixture distribution, while natural gas is helpful for igniting and spreading the flame on lean gasoline mixtures [17].

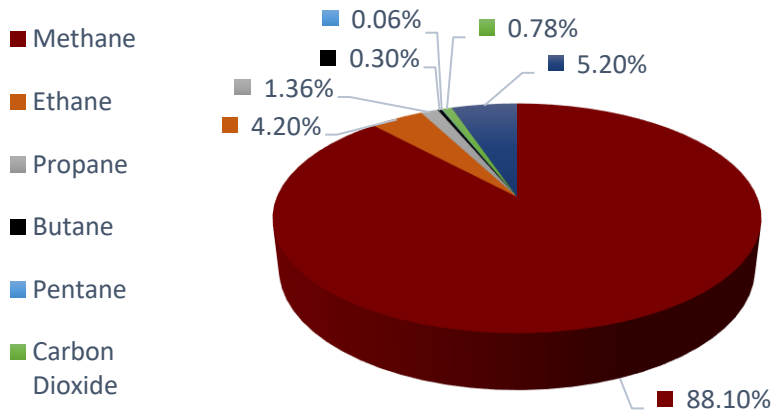


Figure 2.1: A detailed composition of natural gas. Reproduced from [5].

Natural gas is a viable alternative to petroleum-based fuels like gasoline and diesel because it can be burned in either spark-ignition or compression-ignition engines. A comparison of the physical and combustion characteristics of natural gas, gasoline, and diesel fuel is provided in Table **2.1**. The majority of natural gas vehicles currently in use are retrofitted or converted from gasoline spark ignition engines by adding a NG storage, supply and injection system, hence retaining the capability of being switched back to gasoline fuel [6]. Although the fuel energy content in terms of mass, indicated by the lower heating value (LHV), of natural gas is higher than that of gasoline (48.6 MJ/kg for NG compared to 43.5 MJ/kg for gasoline), the engines suffers power reductions in the magnitude of 10-15% [6]. This is attributed to several reasons. Natural gas-air mixtures have about 12% lower volumetric heating value (VHV) than gasoline-air mixtures, which determines the amount of heat converted into mechanical work in the engine cylinder [6]. Furthermore, because natural gas replaces a greater volume of air in the intake manifold upon injection, volumetric efficiencies are lower (by 10–15 percent) than they would be compared to liquid fossil fuels. This limits the amount of air that can be induced into the combustion chamber and consequently less fuel is burnt leading to a reduction in power output [7, 8].

Table 2.1: Typical physiochemical properties of natural gas, gasoline and diesel fuels [5].

Fuel Properties	Natural gas	Gasoline	Diesel
Low heating value (MJ/kg)	48.6	43.5	42.5
Heating value of stoichiometric mixture (MJ/kg)	2.67	2.78	2.79
Cetane number	-	13-17	52.1
Octane number	130	85-95	-
Auto-ignition temperature (ºC)	650	310	180-220
Adiabatic flame temperature (ºC)	1890	2150	2054
Stoichiometric air-fuel ratio (kg/kg)	17.2	14.56	14.3
Flame propagation speed (m/s)	0.41	0.5	-
Flammability limit in air (vol% in air)	5.3-15	1.4-7.6	1-6
Carbon content (%)	75	85.5	87
Hydrogen content (%)	25	12-15	16-33

In addition, under normal cylinder charge temperatures and pressures, methane's flame propagation speed is lower than gasoline's, resulting in a longer ignition delay time for the fuel-air mixture [7,9]. Natural gas (NG) fuelled engines, as a result, use spark timing that is as much as 10 degrees CAD (crank angle degree) earlier before top dead centre (BTDC) compared to gasoline operation. [9]. This pre-ignited charge opposes the piston during the compression stroke; hence, the total power output of the engine is reduced. Furthermore, natural gas SI engines have lower thermal efficiencies than gasoline engines because natural gas burns at a slower velocity, resulting in lower combustion temperatures. As a result, engine calibration modifications must be made to gasoline engines before they can run on natural gas to make up for the power loss inherent in NG. Engines fuelled with natural gas can run on

higher compression ratios, which in combination with forced induction (turbocharging or supercharging) allows for increase in thermal efficiency and power output by up to 50% compared to engines that are fuelled with gasoline [11]. This is due to the fact that natural gas has a higher-octane number than gasoline, which is a measure of the fuel's resistance to auto ignition (120 for methane and 95 for gasoline). SI engines require high octane fuel to prevent knocking, which can cause severe damage. Port-fuel injection into the intake manifold has been the most common method of introducing NG to the engine [7], however, as discussed earlier, the low density of natural gas causes the engine to lose volumetric efficiency. By bypassing the intake manifold altogether, direct injection of natural gas into the combustion chamber eliminates the volumetric efficiency loss normally associated with port-fuel injection [12]. In addition, compared to port-fuel injection, direct injection produces less cycle-to-cycle variation, allowing natural gas engines' fuel-lean operating limit to be increased (coefficient of variation in indicated mean effective pressure is about 5% lower) [7]. This is because the higher in-cylinder pressures brought on by the direct injection of natural gas increase the charged motion, and the locally fuel-rich mixtures near the spark plug speed up the spread of the flame. However, this leads to higher temperatures during combustion, which is conducive to the production of NOx emissions.

2.1.2. Combustion and Emissions of Natural Gas SI Engines.

The emissions of carbon monoxide (CO) and other non-methane hydrocarbons from natural gas engines are generally lower than those from naturally aspirated gasoline engines [5,7]. The majority of a gasoline engine's carbon monoxide emissions occur during the cold start process due to insufficient air-fuel mixing and inadequate atomization and vaporisation of the liquid fuel [15]. Gaseous NG, on the other hand, allows for a more homogenous air-fuel mixture within the cylinder, which is especially helpful during cold start conditions, leading to more efficient combustion and significantly reduced CO emissions (between 50-90% depending on engine calibration) [12]. Moreover, Natural gas engines run with lower equivalence ratio, which further reduces CO and non-methane emissions (by up to 55% less HC) [14]. Natural gas's gaseous state allows it to avoid the wall wetting effect on the intake manifold and cylinder liner, further reducing non-methane hydrocarbon levels and decreasing fuel consumption [11]. In addition, as stated earlier, CO_2 emissions are comparatively lower in engines fuelled with

natural gas as the primary fuel compared to gasoline or diesel fuelled engines. On the other hand, NOx emissions from natural gas-fueled engines are roughly 33% higher than those from gasoline-fueled engines due to the higher compression ratios and more advanced ignition timing used in natural gas-fueled engines [16]. In addition, the relatively higher in-cylinder pressure and temperature resulted by NG combustion further favours the formation of NOx. Retarding the spark timing can help reduce NOx emissions, but it comes at the expense of increased brake specific fuel consumption. Consequently, the optimal engine operating parameters must be determined by striking a balance between engine performance, exhaust emissions, and fuel consumption.

A major concern regarding NG engines is their methane emission as they produce large concentrations of methane gas. North American regulations controls hydrocarbon emissions based on how reactive they are in the photochemical smog cycle; methane gas, which plays no role in photochemistry or smog formation, is nonetheless regulated as a potent greenhouse gas. (global warming potential of methane is more than 20 times higher than CO_2 over 100 years) [17]. The primary reason for this is that natural gas burns slowly, leading to incomplete combustion and a high volume of unburned gas escaping the combustion chamber [18]. This phenomenon occurs in engines that have been converted to run on natural gas but have not been properly modified in terms of engine calibration (e.g. spark timing, injection timing etc) [6, 19]. Furthermore, methane's reactivity is slower than most longer-chain hydrocarbons, making its removal in a standard three-way catalyst (TWC) challenging [20]. Regarding particulate matter emissions (PM), NG engines produce significantly less PM than gasoline or diesel engines (up to 95% less), as NG does not contain aromatic compounds like benzene and has fewer dissolved impurities that contribute to PM formation. [14]. However, a recent study found that the number of exhaust particles with diameters smaller than 10 nm (2-5 nm range) emitted by natural gas engines was greater than the number of particles with larger than 23 nm diameters [20]. Accordingly, vehicles powered by natural gas should be within the PM emission limits established by the Euro 6d regulations.

2.1.3. Dual-Fuel NG-Gasoline Engines

It's essential to differentiate between the various nomenclatures now in use while operating an engine using more than one type of fuel [24], Dual-fuel and Bi-fuel system. In a dual-fuel system, two different fuels can be injected at the same time into the combustion chamber while a Bi-fuel system uses two fuels that are not injected simultaneously during operation. Dual-fuel combustion in internal combustion engines have been extensively studied in the literature as it has shown promising results and an alternative method for reducing fuel consumption and emissions. The primary gaseous fuel examined in the literature for dual-mode combustion in spark-ignition engines with gasoline is natural gas. By utilising this technology, it is possible to take advantage of the benefits of both port and direct injection in a single injection system, as well as create an optimum fuel stratification by managing the injection strategy.

2.1.3.1. Pressure and HRR

Korakianitis et al. [78] conducted numerical models and experimental testing to analyse the combustion of dual-fuel gasoline and natural gas engine. Their results showed that the in-cylinder peak pressure decreased with increasing natural gas content and was ascribed to a decrease in the flame propagation velocity. This in turn increases the combustion duration and directly implies a delayed combustion phasing. Similarly, Singh et al. [69] found that the indicated mean effective pressure (IMEP) decreased with increasing PFI (methane) injection duration. The torque was lowered by 16 percent as a result of the gaseous methane displacing some of the intake air and therefore decreasing the airflow to the engine. Additionally, a lower IMEP was shown to be due to the reduction in calorific value, lower combustion temperature, and lower mechanical load caused by adding methane to the mixture [3]. On the other hand, Pan et al. [23] investigated an SI engine fuelled by gasoline and methane with gasoline injected directly and methane via port injection. They reported that increased methane content results in a higher in-cylinder peak pressure. The effect of increasing CNG ratio on the heat release rate (HRR) of a dual-fuel engine was highlighted by [6]. According to their findings, the maximum HRR gradually lowers as the CNG ratio rises, and its phase is gradually retarded. In addition, they reported that the maximum in-cylinder temperature (MCT) rises with the increase in CNG

substitution. They attributed this to the gaseous fuel having no cooling effect upon injection in the combustion chamber, hence the MCT rises as the liquid gasoline substitution ratio rises.

2.1.3.2. Thermal Efficiency and Fuel Economy

In a single-cylinder GDI engine, Singh et al. [69] investigated the impact of various port-injected natural gas blends on engine performance. The study found that the addition of methane to an engine that was initially tuned for gasoline did not result in appreciable reductions in fuel usage. In fact, incorrect injection lowered combustion quality and reduced volumetric efficiency. However, the indicated specific fuel consumption (ISFC) was reduced by up to 5% when methane was carefully introduced to the air-fuel mixture with the proper spark timing adjustment, and the MBF50 occurred at the maximum braking torque as a result of the fuel mixture's enhanced octane quality. The higher mass-based heating value of methane compared to gasoline and the more ideal combustion phasing (CA50 8 CAD aTDC) allowed the expansion ratio to be maximised, enhancing efficiency at high loads. These two elements contributed together to reduce the integrated ISFC of the dual-fuel compared to pure gasoline. Similarly, the impact of increasing methane substitution on the performance of a turbocharged gasoline fuelled SI engine was studied by Delpech et al. [20]. Dual-injection mode was reported to enhance the engine's compression ratio due to methane's high octane number while maintaining adequate engine performance and reducing fuel consumption by 25%, compared to gasoline operation.

According to Pipitone and Beccari [19], the thermal efficiency of an engine running on a 50/50 fuel mix of NG and gasoline improves by 5.5% while reducing engine output by less than 4% compared to a pure gasoline mode. Pan et al. [23] and Movahed et al. [21] also reported that the addition of methane increased efficiency and reduced emissions. Yontar et al. [16] used computational fluid dynamics (CFD) methods to study the characteristics of gasoline-compressed natural gas (90 percent gasoline/10 percent CNG) engines with a fully open throttle and compared them to experiment conditions. With the use of compressed natural gas (CNG), performance values such as volumetric efficiency (Ve), braking-specific fuel consumption (BSFC), and thermal efficiency (Te) are reduced. The introduction of gaseous methane fuel lowers the intake charge in each cycle thus reducing the volumetric efficiency. On the contrary, Zeng [15] et al concluded that supplying varied ratios of gasoline/CNG under various engine

loads can improve engine power performance while also lowering exhaust pollutants. It can be concluded from the literature that using a SI engine with a dual-fuel combination can have a wide range of impacts, as different fuel fractions and engine calibration can lead to different results.

2.1.3.3. Exhaust Emissions

In terms of emissions, there is a general agreement in the literature that the addition of natural gas/methane into a SI engine fuelled with gasoline leads to lower CO and HC emissions. The impact of gasoline and CNG dual injection on the exhaust emissions of a turbocharged SI engine was studied by Movahed et al. [21] and Hall et al. [26]. They found that raw HC and CO emissions were significantly reduced using the dual-fuel mode. They attributed this to the improved air-fuel mixture formation [30] with the addition of the gaseous fuel, and the reduced potential for liquid fuel impingement resulting in lower CO emissions. Similarly, [8] reported that CO and HC emissions were lower in the dual-fuel mode than in the pure gasoline mode, and they attributed this to the decreased carbon content of the mixed fuel. Additionally, because natural gas is a gaseous fuel, it may be combined with air without atomizing or evaporating, decreasing the oil film effect compared to the pure gasoline mode and facilitating the combined fuel to burn completely, lowering CO and HC emissions. Moreover, the increase in in-cylinder temperature and the reduction of fuel entrapment in crevices as the CNG ratio increases, significantly reduced the HC emissions [6]. In terms of CO_2 emissions, Xu et al. [6] found that as the NG replacement increases, CO_2 emissions drop dramatically. This is attributed to the lower average C/H ratio of natural gas fuel (which mainly constitutes of methane) compared to the gasoline fuel. Hydrocarbons produce CO_2 at a rate proportionate to their carbon to hydrogen content, as a result, burning CNG creates less CO_2 emissions.

There is, however, an increase in CH_4 emissions as a result of increased natural gas usage as reported by [27]. Even though the total amount of tailpipe CH_4 emissions was relatively low, the Global Warming Potential (GWP) of this greenhouse gas is 25 times more than CO_2 when looking at a 100 year time frame [33]. The natural gas CO_2-equivalent emissions could be up to 20% higher than those of CO_2 emissions [33]. Thus, the advantages of increased natural gas usage in dual-fuel engines may be partially nullified by the resultant rise in tailpipe CH_4 emissions. In addition, numerous studies have

documented an increase in NOx concentration with the increase in CNG replacement in dual-fuel engines which is a further challenge associated with the technology. Xu et al. [22] studied the effect of the dual-fuel engine on exhaust emissions and reported that as natural gas replacement increases up to 50%, NO emissions increase by 8.7% compared with the pure gasoline mode. The greater NOx emissions were attributable to the higher combustion temperatures that resulted from the dual-fuel mode. The effect of injector timing on a dual-fuel engine was studied by Liu et al [8]. The results reveal that NOx levels rise and subsequently falls with the advance in injection timing. Generally, the in-cylinder temperature has the greatest impact on NOx emission formation. With late injection, a significant amount of natural gas accumulates around the spark plug, limiting the combustion heat release rate and subsequently NOx emissions. On the other hand, early injection leads to a more homogenous fuel mixture which again reduces the combustion heat release inhibiting NOx formation.

2.2. Current NG Emission Control Technologies in SI Engines

2.2.1. Lean-burn vs Stoichiometric Natural Gas Engines

When using a natural gas internal combustion engine, the relative air-fuel ratio, lambda (λ), must be carefully managed to reduce the amount of harmful exhaust gases released. Engine performance and, by extension, fuel economy are profoundly affected by the accuracy with which the air-fuel ratio is managed. While running on fuel-rich mixtures result in lower NOx concentrations, significantly higher CO and unburnt HC emissions are produced due to the insufficient amount of oxygen available to oxidise the fuel. In addition, a rich engine operating condition is undesirable because of the heavy fuel penalty it imposes. Stoichiometric NG engines, on the other hand, run on λ=1 or slightly less than1. Non-methane hydrocarbon and CO emissions from these engines are extremely low, but they come at the expense of fuel economy and high NOx emissions. Stoichiometric natural gas engines use exhaust gas recirculation (EGR) and a TWC to reduce and regulate exhaust emissions [21, 22, 23, 24].

The two main types of natural gas engines are lean-burn (λ >1) and the more common stoichiometric (λ=1) combustion engines. In contrast to stoichiometric engines, lean-burn NG engines can improve fuel economy and decrease NOx pollution levels, but at the expense of increased HC and CO emissions [21]. Lean burn engines have their nitrogen oxide (NOx) emissions lowered by increasing the air-fuel ratio above λ=1.2 [24]. The variation from cycle to cycle increases dramatically with leaner mixtures, however, so there is a lean operating limit beyond which engine performance can be maintained without sacrificing performance. According to the literature, the best air-fuel ratio for reducing HC emissions is between = 1.05 and 1.2, when enough oxygen concentration is present to oxidise the unburned HCs; however, NOx emissions are highest between these settings [23-25]. In any case, an oxidation catalyst can be used with great success to treat HC emissions in the exhaust of a lean-burn natural gas compared to the treatment of NOx emissions. The excess of oxygen available with increasing lambda can enhance the combustion of the air-fuel mixture leading to a complete combustion of unburned HC and CO emissions. At the same time, increasing the air-fuel ratio increases the time required for the initial flame development and hinders flame propagation through the cylinder charge, causing longer ignition delay [11]. This results in slower heat release rate, slow combustion velocity and deterioration in combustion

quality compared to that under stoichiometric conditions, thereby increasing heat transfer losses to the cylinder walls. This has an adverse effect on HC and CO emissions, as the combustion temperature in the cylinder drops hence the improvement in oxidation of HC and CO with excess of oxygen is unrealised. Even though the lean-burn engines are successful at reducing NOx emissions, the technology is not practicable in real life conditions as it is difficult to maintain a high air-fuel ratio at transient situations (like acceleration and low engine speed). In addition, as exhaust emissions are very sensitive to small changes in lambda value, the accuracy of the air-fuel control system is critical. The control of air-fuel ratio in a natural gas engine can be achieved using a wideband oxygen sensor. Due to its precise determination of residual oxygen content, the engine control unit can efficiently optimise fuel delivery and ignition timing for better fuel economy and emission concentrations [26, 27].

2.2.2. Exhaust Gas Recirculation

To lower nitrogen oxide (NOx) emissions, many petrol and diesel engines use an exhaust gas recirculation (EGR) system. With EGR, the engine's exhaust gas is redirected back into the cylinder to reduce the amount of unburned fuel and oxygen concentration, thereby improving fuel economy. Since the recirculated gas has a higher heat capacity than the fresh air, it dilutes the inlet charge and reduces the combustion temperature [28]. The use of EGR in lean-burn natural gas engines can therefore achieve very low levels of NOx emissions, as along with the slow flame propagation of natural gas, reduction in oxygen concentration and in-cylinder temperatures slows down the combustion of the charge mixture even further. However, because of the lower temperatures at which combustion occurs and the resulting lack of oxygen, emissions of HC, CO, and PM are increased. The addition of hydrogen can help counteract the decline in combustion quality brought on by the EGR strategy. The high flame speed of H_2 speeds up combustion of the mixture charge, leading to higher temperatures and more complete oxidation of HC and CO emissions. It has been reported in the literature that engine out emissions can be drastically reduced in NG engines by combining moderate EGR substitution with hydrogen [29-31]. For a 15% H2 – 85% NG fuel mixture, increasing EGR substitution reduced NOx emissions significantly as compared to the baseline NG combustion. On the other hand, HC emissions reduced

with increasing EGR up to an EGR substitution of 14% but remained higher than baseline NG engine emissions [29].

2.2.3. Spark Timing

Spark timing adjustments in spark-ignition engines have a substantial effect on combustion and exhaust emissions. Due to the slow flame speed of natural gas, a spark advance strategy is required in a NG-fuelled engine to ensure that the fuel mixture is completely burned. Spark timing in NG engines is typically advanced by 2-10 degrees BTDC relative to stoichiometric gasoline-fuelled engines [8, 10]. In engines using leaner air-fuel ratios, the time needed for the initial flame to develop is longer because less spark energy is transmitted to the cylinder charge at spark discharge [30]. Additionally, because of the low in-cylinder temperature and slow burning velocity of natural gas, especially at lean air/fuel ratios, the combustion duration increases and the timing of ignition is delayed. Therefore, lean-burn NG engines require highly advanced spark timing to compensate for the ignition delay, but this can lead to engine knock [11]. Advancing the spark timing leads to earlier ignition and shorter combustion duration. This decreases the temperature of the burned gas during the expansion stroke, making it more difficult for the remaining fuel to be oxidised, hence THC emissions increase. Similarly, as the spark timing is advanced, the homogeneity of the air-fuel mixture is decreased, which leads to incomplete combustion of the fuel thereby increasing CO emissions. Meanwhile, the lower combustion temperatures and lower burned gas temperatures that result from earlier spark timings lead to a declining trend in NOx emissions.

2.2.4. Hydrogen Enriched Natural Gas Engines

The addition of a fuel with a higher flame speed velocity can further reduce the exhaust emissions of CO, unburned HC, and CH_4 caused by the slow burning rate of natural gas. A small amount of hydrogen added to the intake charge of a natural gas engine can improve its combustion characteristics leading to significant improvements in term of combustion stability, engine performance and levels of exhaust emissions [31]. Table 2.2 details the combustion properties of hydrogen.

Table 2.2: Combustion properties of hydrogen [33].

Fuel	**H_2**
Flammability limit in air (%vol.)	4-75
Flammability limits (λ)	0.14-10
Auto ignition temperature (ºC)	585
Octane number	140
Stoichiometric air-fuel ratio	34.2
Laminar burning velocity (m/s)	2.9
Diffusivity in air cm^3/s	0.63

When compared to natural gas, hydrogen has a higher calorific value, which means that a given air-fuel mixture can be burned at a higher temperature within the cylinder, thus increasing the rate of combustion [32]. Increasing concentrations of H and OH radicals boost combustion reactivity, which in turn causes the flame to spread through the cylinder charge more quickly [6, 7]. Enhanced cylinder conditions lead to cleaner combustion and lower emissions of HC and CO. Depending on the engine's operating conditions, hydrogen-fueled engines can produce lower CO emissions than standard natural gas engines. When operating at a stoichiometric air-fuel ratio, adding hydrogen increases carbon monoxide emissions, while lean-running engines emit no carbon monoxide at all [31,32]. Unburned THC is reduced as a result of the increased in-cylinder temperatures caused by the faster burn rate of the fuel mixture with the addition of hydrogen, but methane emissions remain high [31]. The low overall carbon content of hydrogen-enriched natural gas along with the shorter quenching distance (distance between the position of flame extinguishment and the cylinder wall) induced by hydrogen addition is another reason for the reduction in HC emissions [31,32]. However, because of the higher combustion

temperature, NOx emissions are greater in hydrogen-enriched natural gas engines [6]. In addition, it is possible to use hydrogen to improve the combustion in ultra-lean natural gas engines due to its favourable combustion properties and rapid flame propagation [34]. The more volatile fuel mixture and improved combustion stability brought on by hydrogen addition help mitigate the drop in COV of indicated mean effective pressure (IMEP) that resulted from lean-burn operation.

2.2.5. Aftertreatment System

2.2.5.1. Lean Burn vs Stoichiometric NG Aftertreatment

Lean-burn and stoichiometric combustion are the most popular technologies used for the best engine performance and emission control in NG engines, as previously mentioned. Nevertheless, these systems are insufficient to bring emissions down to the levels allowed by the Euro 6d standard, so natural gas vehicles are also equipped with exhaust aftertreatment systems. The reduction of methane (CH_4) and other engine exhaust emissions (CO, NMHC, NOx) in a stoichiometric NG engine is accomplished with a three-way-catalyst (TWC) technology adapted from a gasoline TWC [21].

Even though natural gas engines have much lower HC emissions than gasoline engines, methane emissions are still a major problem. Methane accounts for a large fraction of the HC emissions from NG engines and has a higher light-off temperature than longer chain hydrocarbons because its C-H bond is more stable than those of other hydrocarbons. As a result, platinum group metals (PGM), and more specifically palladium (Pd) and rhodium (Rh), are incorporated into the TWC's composition to improve the efficiency of CH_4 oxidation and conform to end-of-life THC regulations [35]. Pd-Rh catalysts with high total PGM loadings can be used to efficiently eliminate methane emissions under stoichiometric conditions. A stoichiometric air-fuel ratio is required for the TWC to simultaneously remove CO, NO and THC emissions. The CO-NO crossover point denotes the transition from a rich to a lean operating condition, where CO emissions are completely oxidised, and the NO conversion efficiency reduces at the same time [6, 7]. This is considered to be the most optimal point for catalyst simultaneous conversion of THC, CO and NO emissions. This point is known to be slightly rich of stoichiometry ($\lambda \sim 0.997$ to 0.999) in the case of TWC for natural gas engines [7, 8, 9, 10], rather than

stoichiometry (λ= 1], mostly due to the low reactivity of CH_4. This further reflects the dissimilarities in the chemistry of emission control between gasoline and natural gas.

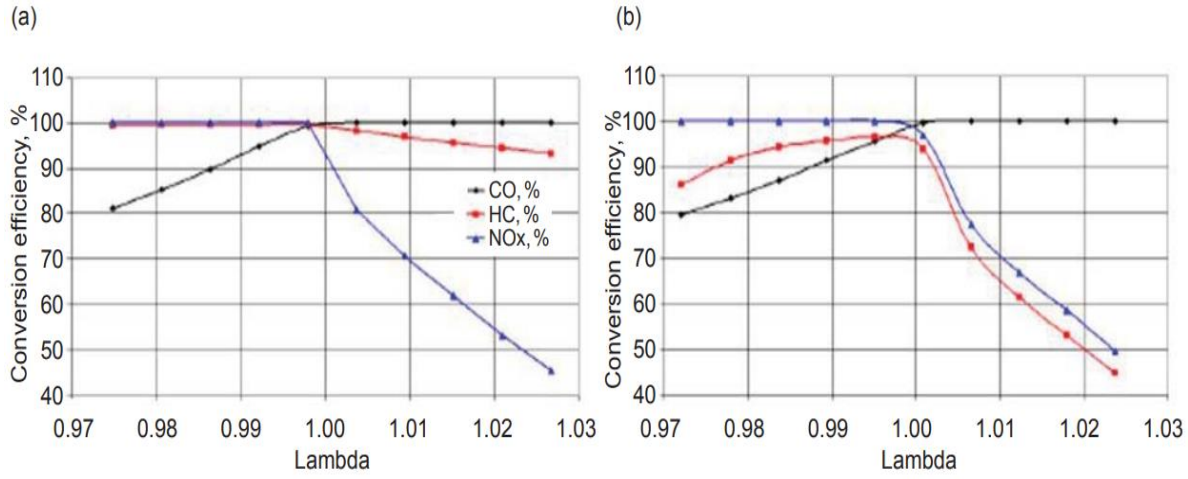


Figure 2.2: Performance of an aged Pd:Rh TWC at 450 ºC as a function of lambda on: a) Stoichiometric Gasoline engine, b) Stoichiometric NG engine [35].

Exhaust performance of a Pd-Rh bimetallic catalyst for a standard gasoline engine and a stoichiometric NG engine versus lambda ratio is shown in Figure 2.2. Catalyst NOx and CO conversions follow a consistent pattern across both engine configurations. Conversion efficiency of CO at stoichiometric conditions is close to 100%, while conversion efficiency of NOx can be increased with the NG engine due to much lower engine-output NOx than that of the gasoline counterpart. In addition, at stoichiometric conditions, HC conversion is considerably enhanced (95% efficiency). As a result of NG's poor combustion in excess air, the catalyst in a lean NG engine case is subjected to high amounts of unburned CH_4. This results in a low HC conversion efficiency [21].

The current TWC technologies are very effective at lowering exhaust emissions, but they induce drawbacks such as increased heat losses and pumping work at low to medium engine loads because of their reliance on a stoichiometric mixture. As a result, most stoichiometric NG engines feature a water cooled EGR to dilute the stoichiometric mixture, leading to better fuel economy (i.e. lower pumping losses) and reduced emissions when combined with a TWC [21,23]. With this combined technology, NOx and CO_2 emissions can be reduced by 10–30 and 360–700 times, respectively, compared to lean-burn combustion [33]. However, the TWC's efficiency relies heavily on precise regulation of the air-

fuel ratio because the lambda window for an acceptable trade-off between CO oxidation and NOx reduction is extremely small (± 0.01) [23]. While non-methane HC and CO emissions from a lean-burn NG engine can be controlled with the use of an oxidation catalyst, methane and NOx emissions are more challenging to eliminate under lean conditions. Therefore, in order for lean-burn NG engines to meet the stringent emissions regulations, catalytic after treatment systems like selective catalytic reduction (SCR) are required. However, because of the complexity and expense of such system, vehicle manufacturers might favour the simpler inexpensive stoichiometric engine with TWC [11]. Lean-burn natural gas heavy duty vehicles' exhaust emissions have been shown to be significantly reduced when an NH_3-SCR (selective catalytic reduction with ammonia as reducing agent) is combined with an oxidation catalyst based on palladium and platinum oxides [36]. The combined catalytic performance resulted in a 40% CH_4 conversion at 415 ^oC, a 99% conversion of CO, and a 70% conversion of NOx [36]. In addition, the nearly homogeneous combustion of the air-gas mixture and the lack of large hydrocarbon chains and aromatics in the NG fuel mean that neither lean-burn nor stoichiometric NG engines require aftertreatment systems for PM emissions. [21].

2.2.5.2. PGM NG Oxidation Catalyst

To reduce the release of harmful gases including HCs, CO and NOx from the exhaust of gasoline engines, platinum group metals (pgms) have been utilized in three-way catalysts (TWCs) since 1974. Pt, Pd, and Rh have historically been employed together because of their complementary properties; Rh is highly efficient at converting NOx, while Pd and Pt both are utilised for the oxidation of CO and HCs. The majority of the modern stoichiometric natural gas aftertreatment system is made up of highly loaded Pd/Rh catalyst [8,9,11]. Pd is the most active noble metal for oxidizing methane, hence it has been the subject of numerous investigations on methane conversion [2, 3, 4, 5].

Pd was the most effective PGM for CH_4 oxidation as reported by Sakai et al. [25], followed by Pt and Rh. However, the high performance of Pd operates on a very narrow lambda window, so they observed a dramatic decrease in CH_4 conversion efficiency as air/fuel ratio increased from stoichiometry. Subramanian et al. [10], studied the performance of Pd/Al_2O_3 catalyst in reducing CH_4 emissions under different air/fuel ratios. They reported that under excess oxygen, CO strongly inhibits

CH_4 oxidation compared to net reducing conditions. They also noted that under net reducing circumstances CH_4 oxidation by NO was stressed as the main route for CH_4 removal, whereas steam reforming was regarded negligible. This was in contrast to other studies in the literature [18,19] who highlighted the importance of steam reforming on CH_4 conversion. There was also evidence for NO reduction by hydrogen and by CH_4 at various temperature ranges in the literature [18], [20]. Because of this, it is essential to stress that the normal reaction responsible for NO reduction on a typical gasoline TWC, i.e. CO + NO pathway, does not contribute considerably when natural gas is the fuel.

In addition, it has also been reported that Pd is the most active PGM in improving methane's conversion efficiency under lean air/fuel ratios [4]. Under such excess oxygen conditions, PdO or a Pd-PdO pair [10-13] is reported to be the active species for CH_4 conversion. The catalyst support materials [17,18] and the particle size of the Pd [17, 18] plays a role in the catalyst's activity. Additionally, small levels of Pt can enhance Pd-catalyst sintering resistance [19, 20] and boost the activity of methane oxidation [21–27]. While Pd is effective for CH_4 oxidation, its activity decreases at decreasing oxygen partial pressures [9]. In addition, the presence of water species in the exhaust has been reported to inhibit the performance of Pd catalysts. The strong inhibition of Pd-based catalysts in the presence of water [9,30,31] has been attributed to the development of $Pd(OH)_2$ surface hydroxyls on PdO, or on the support material [32]. Under stoichiometric circumstances, however, Pd becomes less sensitive to water inhibition. In contrast, methane oxidation activity is low for Pt-based catalysts in excess oxygen [28], most likely as a result of accumulated oxygen deactivating the metallic Pt-sites and preventing methane from being absorbed. [8,29]. On the other hand, compared to Pd catalyst, water has a minor detrimental effect on Pt catalysts [36,37] or no effect at all [38].

Several studies in the literature have reported that Rh is the most active PGM metal for steam reforming (SR) [17,18] while ceria-based mixed oxides (utilized to support TWCs' oxygen storage capacity) also act as SR promoters [22,24]. According to the literature, doping the catalyst with ceria greatly increases methane SR [19, 20] and decreases the light-off temperature [21], especially near stoichiometric air/fuel ratios [27]. SR reaction facilitates CH_4 adsorption on noble metal sites while preventing the deactivation of the catalyst by adsorbing H_2O on the reduced ceria sites [22, 25, 26]. It

was reported that during brief transitions from lean to rich conditions, SR makes a considerable contribution to CH_4 conversion in a ceria assisted Pd/Rh catalyst. However, carbonaceous species accumulating on the ceria surface reduce SR over time. To maintain a high rate of CH_4 conversion, it has been proposed that lambda oscillations across stoichiometry be used in conjunction with the high SR reaction rate across this window [29]. Moreover, the addition of ceria further promotes water-gas-shift (WGS) reaction [22].

Several authors have reported an improvement in CH_4 conversion during lambda oscillations [17,27,30]. The performance of a Pd/Rh TWC in a stoichiometric CNG engine was investigated by [11]. In steady state, they observed low methane conversion in both rich and lean conditions and determined that direct oxidation by oxygen was the sole reaction pathway involved for methane reduction. On the other hand, higher methane conversion was achieved during periodic lambda oscillations which was attributed to the promotion of SR reactions. This was further studied by Bounechada et al. [19] using a Pd-Rh-Al-Ce catalyst under cyclic rich/lean engine lambda conditions that closely resemble TWC operation. Their study demonstrated that substantial CH_4 conversion is possible with brief rich pulses compared to steady state conditions, and that oxygen oscillations with small amplitudes near stoichiometry are preferable for methane oxidation compared to large amplitude oscillations. Therefore, they concluded that cyclic oscillations enhance CH_4 conversion compared to stoichiometric or lean conditions. [12] investigated the effects of both steady state and cyclic lambda operation on a honeycomb three-way catalyst composed entirely of Pd. It was only under periodic rich/lean operation that the TWC's CH_4 oxidation activity was notable, and they also noted that NO conversion mirrored that of CH_4. It was also found that under net reducing conditions, the optimum point for CH_4 conversion occurred, rather than at the nominal stoichiometric point ($\lambda = 1$). The maximum CH_4 conversion corresponded with complete removal of CO; which suggests inhibition of CH_4 oxidation by CO.

2.2.5.3. Effect of PGM Ratio

Over the past few decades, precious group metals (PGM) use in automobiles has fluctuated in both amount and type due to a number of variables namely, fuel quality, emissions regulations, exhaust architecture, relative pricing of the PGMs, and catalyst washcoat technology. The bulk of TWC employed in gasoline combustion engines today are made up of Palladium (Pd) or Rhodium (Rh), while the use of Platinum (Pt) has reduced substantially. Pd replaced Pt in gasoline autocatalysts in the 1990s due to its lower cost. However, to obtain the same level of emissions control, twice as much Pd as Pt was necessary. This was due to the presence of high sulphur content in gasoline fuel which substantially reduced the efficiency of the Pd catalyst. At the turn of the century, sulphur levels in gasoline fuel began to drop (from 400 ppm to less than 100 ppm), which reduced the substitution ratio between the two PGM metals to almost 1:1. Nonetheless, it appears plausible to anticipate that, in the future, there will be various considerations that may influence PGM choice. Rh prices have increased by over 55% since the middle of 2008, and Pd prices have increased by 10 times since 2009. As such, it is worthwhile to conduct periodic reviews of the effectiveness of modern catalysts that employ the three PGMs across a spectrum of conventional loadings.

Emissions conversion efficiency is highly sensitive to the composition of TWC catalyst due to the complex coherent or synergistic interaction of various noble metals and additives. In addition to enhancing performance and decreasing waste of noble metals, optimizing PGM ratio and loading helps cut after-treatment system costs. Additionally, a more cost-effective method of balancing the engine's emission and fuel consumption might be selected during the calibration process if the TWC has a higher emission reduction performance. Huo et al. (2019) assessed the effect of PGM ratio on the performance of the TWC and discovered that increasing the amount of Pt enhanced the catalyst's effectiveness in lowering CH_4 and NOx emissions but had only a minor impact on CO emissions. It is generally agreed that Rh catalysts are better at reducing nitrogen oxides (NOx), whereas Pt and Pd catalysts are better at oxidizing hydrocarbons (HC) and carbon monoxide (CO) [46]. However, Rh is five to six times as expensive as Pt and Pd because of its scarcity. Therefore, it is essential to optimise the PGM content in

a TWC to maximise its efficiency in reducing exhaust emissions across a broad working temperature range and air/fuel ratio.

The effect of varying PGM content and ratio on the transient emissions behaviour of a NG engine was examined by [10]. According to their findings, the PGM ratio has a large influence on overall emissions and can shift the distribution of peak emissions, while the PGM loading has a negligible effect on total emissions and no effect on peak emissions distribution. Catalysts with high PGM ratio and loading enhanced the light-off temperature and reduced peak exhaust emissions. NOx, HC, and CO emissions increased when Pt/Pd ratio and Rh content decreased, while NH_3 levels decreased. They also suggested that by lowering the Rh content and raising the Pt/Pd ratio, the price of the TWC might be reduced without compromising its efficiency.

2.3. Particulate Matter Characterisation

Gasoline Direct Injection (GDI) engines present significant advantages in terms of fuel economy, CO_2 and other gaseous emissions with respect to their port fuel injection (PFI) counterparts, but still produce pollutants that contribute to greenhouse effects and higher particulate matter (PM) levels than PFI [1,2,3]. This is mainly due to fuel impingement on the wall and piston, and local fuel-rich regions resulted from the direct injection. These local heterogeneous fuel-rich areas lead to increased particulate matter precursor formation, and later the nucleation of particles [4, 5, 6]. The European Union target of 119 g CO_2/km for WLTP to be complied by 2024 and the further 37.5% emissions reduction target expected by 2030 [7] urge the need to find low carbon footprint solutions. The use of natural gas as an alternative fuel can greatly reduce the environmental impact of GDI engines as it produces significantly lower PM emissions compared to petroleum fuels [8,9, 10]. This is due to its low carbon content, good mixing capabilities and cleaner combustion. Natural gas entering the cylinder pre-mixed with air provides a more homogenous air-fuel mixture, and reduces particle producing pyrolysis reactions [5].

Particulate matter is formed when volatile, unburned fuel fractions, soot (carbonaceous material), and organic and inorganic compounds interact in the engine and exhaust. The ultrafine PM (smaller than 100 nm) emitted into the atmosphere, can have adverse effects on human health, penetrating deep into the lungs when inhaled and contributing to several environmental and health implications, such as cardiovascular disease and respiratory problems [8, 5]. Typically, these fine particles have little effect on particle mass but can be substantial in terms of number concentration. As a result, the emission regulations are becoming more stringent with Euro 6c limiting both PM number ($6x10^{11}$ #/km) and mass concentration (0.005 g/km) [13, 20]. Gasoline particulate filters (GPF) can be deployed in the after-treatment system to trap these soot particles. However special care has to be taken in the design of these filters in order to optimise their effectiveness and to avoid an increase of fuel consumption caused by the increased backpressure of loaded GPFs. This emphasises the need to understand the nature and characteristics of these particle emissions, both quantitatively and qualitatively to find a sustainable solution and control strategies to reduce them.

It is possible to gain insight into the mechanisms that lead to particle production through characterising the soot generated by engines [21–25]. The characterisation of particulate matter emissions is essential as it provides important information about particles reactivity, morphology, nanostructure and composition which are all necessary for the efficient design of Gasoline Particle Filters (GPFs). An overview of the most commonly utilised strategies and the work that has been done in this area regarding the particles from dual-fuel of CNG-gasoline will be presented in this section.

2.3.1. Particle Size Distribution

Typically, particle size distributions are used to quantify PM emissions in terms of mass and number. Nucleation, accumulation, and coarse are three modes that can be found in a typical exhaust particle size distribution as shown in Figure **2.3**. The plotted data has a trimodal, lognormal shape as these distributions offer a good fit to the measured data. Nucleation mode particles, made up of mostly hydrocarbon droplets, are often defined as those with a diameter of less than 20-50 nm. On the other hand, accumulation mode normally consist of adsorbed materials and carbonaceous agglomerates with size ranging from 20 to 500 nm, while coarse mode includes the bigger particles >1000 nm usually found in Diesel engines. Different sizes of atmospheric particles are also depicted in the figure below, with the largest PM10 particles having a diameter < 10 μm, while the smallest nanoparticles diameter < 50 *n*m.

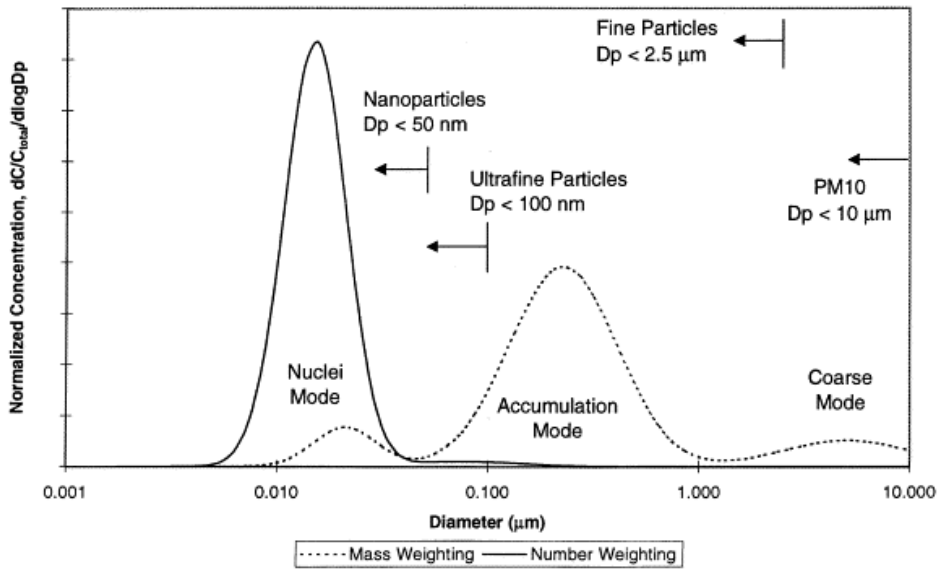


Figure 2.3: Typical engine exhaust size distribution.

Catapano et al investigated the effect of compressed natural gas (CNG) on particle formation and emissions in a dual-fuel engine with multiple injection configurations as shown in Figure 2.4. In the dual-fuel mode, CNG was injected straight into the combustion chamber, while gasoline was port-injected into the engine. The particle size distribution (PSD) for the gasoline only mode demonstrated a notable accumulation phase concentrated at 80 nm. On the contrary, the dual-fuel case demonstrated a bimodal size distribution with a strong nucleation mode observed, and a mild accumulation mode. They reported that the particle number concentration is lower for the dual fuel than for the gasoline only mode, and the curve is shifted towards smaller particle sizes. Based on their findings, they determined that GDI emits a greater number of particles with sizes greater than 20 nm, while DF mode emits a greater number of particles with sizes less than 20 nm. In addition, particle emissions from a natural gas spark ignition engine were researched by Alanen et al. [23], who found relatively low particles number concentrations. Particles from natural gas engines had a distribution peak between 2 and 5 nm in size, with a very small peak diameter of less than 10 nm. They also observed that particle diameter shifted towards smaller particle size, with most particles having a diameter of 23 nm or less. CNG's simple molecular structure coupled with the reduction in fuel-rich zone with the introduction of the gaseous fuel explains why the dual-fuel particle emissions were less than those of GDI mode.

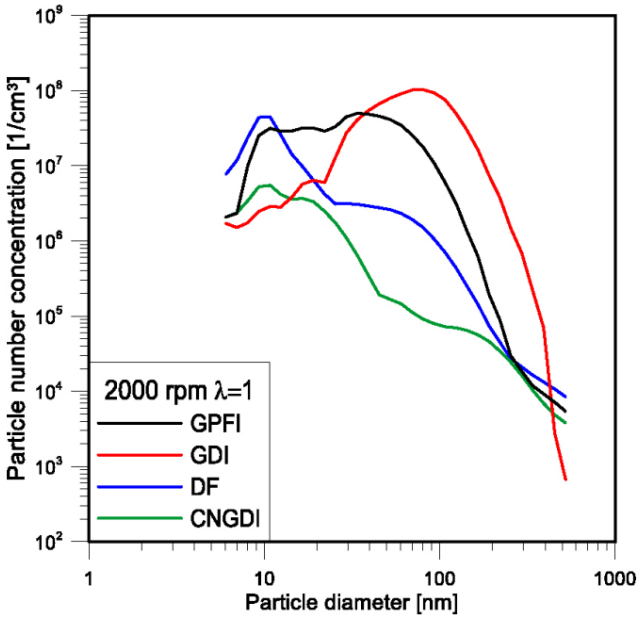


Figure 2.4: Particle size distribution for different injection configurations, adapted from [16].

2.3.2. PM Oxidation

A better understanding and modelling of the soot oxidation processes might help automotive engineers and researchers to optimize techniques for filter regeneration. There are various techniques that can be used to determine soot reactivity and oxidation behaviour such as Thermogravimetric analysis (TGA) and X-ray diffraction (XRD) that are widely used. Using a furnace, TGA can be carried out under precisely regulated conditions of ramp temperature and environment (inert or oxidant). It can be then utilized to measure PM composition, such as the ratio of volatile organic compounds (VOC) or soot and the ash% as well as to determine the oxidation temperature of soot.

Over the years, diesel engines have been the primary focus of research into soot oxidation [23-26], while some studies were conducted for GDI soot [27-30]. However, studies on the use of natural gas and hybrid engines in general have been scarce. Nithyanandan et al. [24] analysed the oxidative reactivity of soot samples collected from a CNG/Diesel dual-fuel engine and reported that the oxidation reactivity of CNG soot was found to be higher than that of diesel soot. Due to the devolatilization procedure, which removes volatile organic fractions (VOF), mass reduction began at a lower temperature for the CNG soot samples. Samples of CNG soot had shown a lower T50 percent (the temperature at which 50 percent of carbon was converted) and an earlier onset temperature, suggesting that the soot reactivity increases with CNG content.

2.3.3. PM Nanostructure and Morphology

Soot produced by diesel engines has been widely studied using Transmission electron microscopy (TEM) technique which can demonstrate the shape, morphology, and kind of particles produced inside the combustion chamber [5]. Understanding and characterizing these parameters can aid in the design of particle filters necessary to meet future stringent emission regulations. For that purpose, the morphology and nanostructure parameters of soot particles are explained in this section.

2.3.3.1. Morphology:

There are several parameters associated with PM morphology namely:

1. Number of primary particles, np_0
2. Primary particle diameter, dp_0
3. Radius of gyration, Rg
4. Fractal dimension, Df

All of the above-discussed parameters should be taken into consideration when evaluating soot aggregates. Figure **2.5** demonstrates the morphological parameters found in soot particles as displayed from a TEM micrograph. As can be seen from the figure, several spherules agglomerated to form aggregates of fractal-like geometry (several primary particles are joined together forming an agglomerate). The average diameter of these spherules is shown by dp_0. Soot oxidation is dependent on the surface area to volume ratio of the agglomerates, which is why primary particle diameters are critical to understanding the PM formation process and the combustion chamber conditions, as well as providing information on Df, np_0 and Rg. Lee et al. (2013) described Rg as a representative length that links each spherule to the aggregate's centroid, showing the average size of the aggregate. Additionally, Df explains how the aggregate particulates are formed. Spherical particles are more likely to have larger magnitude values, while stretched chainlike structures are more likely to have smaller magnitude values (Meakin P, 1989). Finally, np0 is a measure of how many spherules are present in an aggregate.

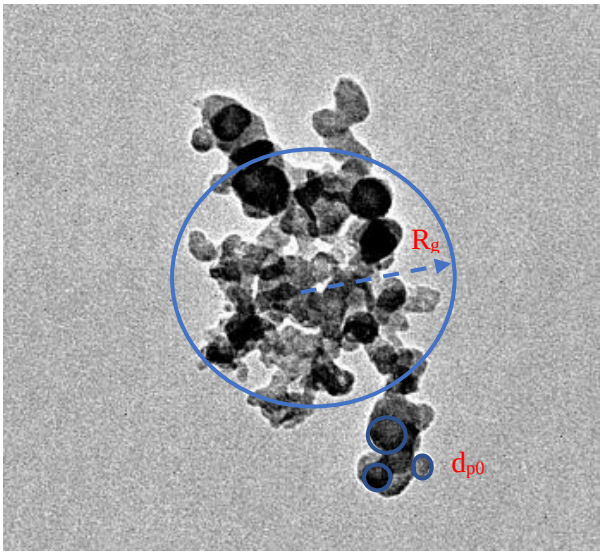


Figure 2.5: Typical morphological parameters associated with soot particles

Nithyanandan et al reported several morphological differences between CNG and Diesel soot. CNG soot was less clumped compared to diesel soot due to decreased loading, and has longer, more complicated, highly curved chains. In addition, there is a single chain of particles in CNG soot, which are looser and more open-looped than the relatively denser Diesel soot. The spherules of the dual-fuel soot are also less round and exhibit uneven, twisted shapes, which are characteristics of immature soot [23]. These differences can be seen in Figure **2.6** from their study. Moreover, they observed that in comparison to the dual-fuel soot aggregates of the same size, Diesel soot aggregates have a greater amount of spherules. They also added that CNG soot has significantly higher variation in spherule size distributions shifting toward larger spherule sizes with increasing CNG content. This was attributed to the higher surface growth rate aided by the higher active sites present in CNG soot.

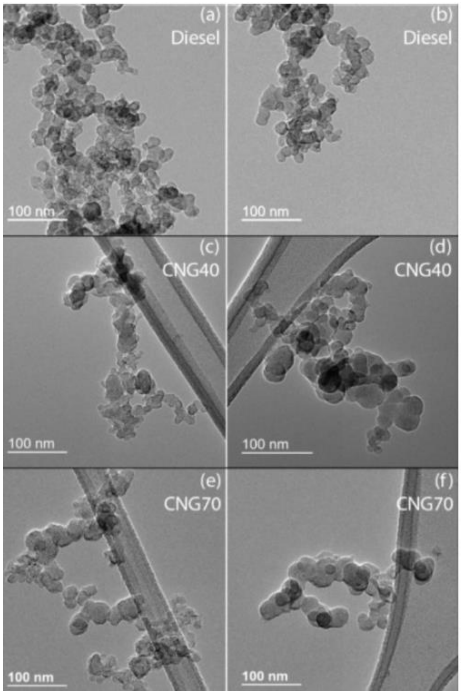


Figure 2.6: TEM images showing particles collected from Diesel and CNG dual fuelling.

2.3.3.2. Nanostructure

In this section, the fundamentals of carbon nanostructure are described to better comprehend the techniques employed for the characterization of PM. Soot oxidative reactivity is closely linked to PM nanostructure, which reveals a great deal about PM formation process, hence understanding the ordering of the primary particles on a nanoscale is equally significant. HRTEM and Raman spectroscopy are two

methods used to examine PM sample nanostructure qualities. HRTEM technique can be used to analyse each primary particle based on TEM micrographs, providing information about their carbon layer ordering and oxidation reactivity. In terms of determining the oxidative reactivity of particle samples, Raman spectrometry analysis can be used to examine carbonaceous material for its graphitic character. The physical parameters associated with PM nanostructure are:

1. Interlayer spacing (d002),
2. Crystallite height (Lc),
3. Crystallite width (La), and
4. Tortuosity (τ)

The graphitization of soot particles is quantified by their interlayer spacing (d002), whereby a low d002 value indicates a low oxidation potential of the soot. The crystallite width (La) (also known as fringe length), is a measure of the atomic carbon layer thickness whereby a high La value indicates a low soot reactivity. Carbon atoms located at the basal plane are more difficult to oxidise compared to carbon atoms located at the edge sites. Fringe tortuosity is a measure of the curvature of the carbon layer and is linked to odd numbered carbon rings and lattice defects [104, 106]. [102, 104, 106]. According to the literature, the degree of disorder can be determined from the principle that tortuosity separates adjacent layers by preventing the formation of the crystalline stack. [110, 111]. A low τ value indicates low level of disorder and hence a poor oxidative reactivity potential. Figure 2.7 depicts the physical parameters associated with PM nanostructure.

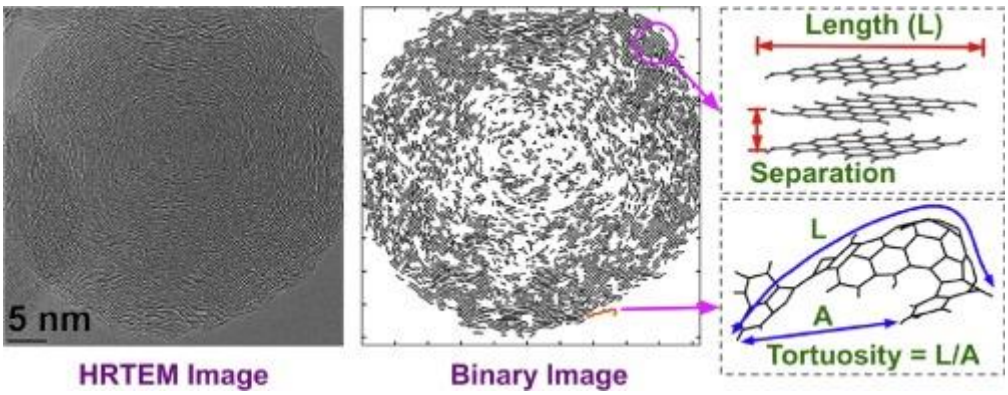


Figure 2.7: Physical nanostructure parameters (adapted from Gaddam et al. [19])

Numerous studies on PM characterisation in Diesel and GDI engines have been conducted [3, 28 - 32]. In contrast, there are limited studies reporting the effect of dual-fuel on PM reactivity and nanostructure. Nithyanandan et al reported differences in PM nanostructure with the addition of CNG fuel to a diesel engine. They concluded that the soot collected from the dual-fuel combustion was immature exhibiting irregular shaped spherules. They also noted that the lamellae of the soot particles were arranged in a random, incoherent fashion, as illustrated in Figure 2.8 with no identifiable core. In light of this, it would be expected that immature soot would be more reactive than mature soot as also reported by [13, 16]. During the combustion process of the dual-fuel, two factors were shown to be responsible for this: first, as a result of CNG addition, soot precursors are inhibited hence the production of aggregated particles was favoured rather than mature particles. Secondly, there was insufficient time for the soot to form an inner core and an outer shell because of the reduced combustion period with dual-fuel.

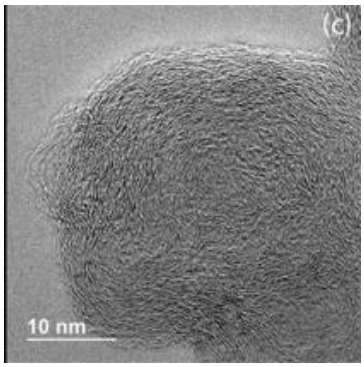


Figure 2.8: HRTEM image of soot collected from dual-fuel combustion with 70% CNG. Adapted from [18].

Particle oxidative reactivity and carbonaceous structure have both been studied using Raman spectroscopy as an alternate approach [26, 27]. Typical soot from an internal combustion engine is shown in Figure 2.9 in a simple Raman spectrum. One Gaussian band (D3) and three Lorentzian bands (D4, D1, G) are obtained by mathematical fitting of the data.

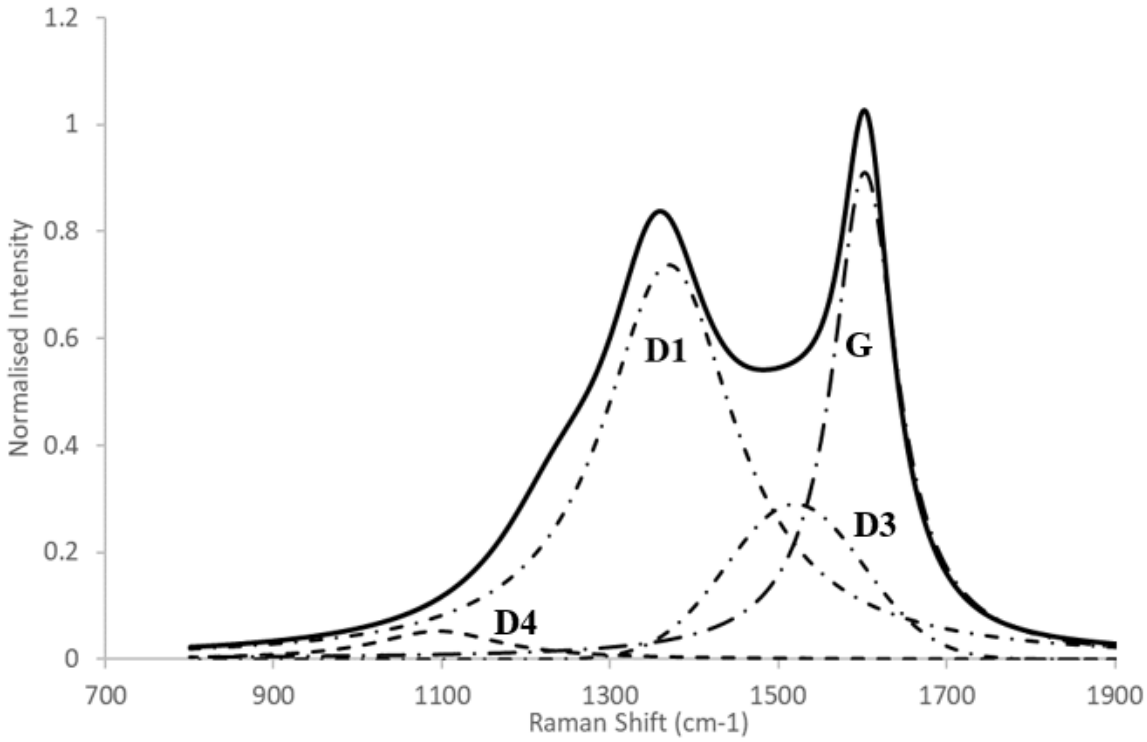


Figure 2.9: Typical Raman spectrum representative of gasoline soot.

A carbonaceous material's structural order can be discerned by the distinct bands and their intensity, area and width variances. Graphite's idealistic structure can be seen in the most prominent band G, while the greatest component of the D-band, D1, reflects the carbon lattice's flaw structures. In addition, by comparing the ratio of D1 intensity and area to G (I_{D1}/I_G, A_{D1}/A_G), it is possible to gauge the amount of fringe and edge sites that are more prone to oxidation hence giving an indication of the oxidative reactivity of the carbon lattice [19]. Sample crystallinity can be determined by the D-band peak size and the D1 band's full width at half maximum (FWHM). Smaller peaks demonstrate a more ordered carbon structure shifting towards larger crystalline sizes [19,20]. Lastly, interstitial defects and amorphous material are responsible for the region between D-and G-band peaks in the spectrum, the smaller the region the more ordered the carbon structure of the particle sample will be [20]. CNG-Diesel dual-fuel soot spectra were analyzed by Nithyanandan [64]. They found that the G band of CNG soot had a lower intensity and a narrower D1 band (1350 cm^{-1}) than diesel soot. More nanostructural abnormalities were found in diesel soot and CNG soot was shown to be more reactive.

3. Experimental Setup and Methodology

The experimentation facilities used in this Thesis are described in this chapter. Two different engine test cells are described, a four-cylinder GDI engine used mainly for the study presented in Chapter 5 and a three-cylinder GDI engine that was used for the remaining chapters. In addition, data acquisition instrumentation, fuel properties, gaseous and PM emission analysers and catalyst specifications are all detailed.

3.1. Four-Cylinder Engine Test Bench

A 2 L, 4-cylinder, turbocharged GDI engine fitted with an air-guided direct injection combustion system design was utilised to carry out part of experiments presented in this thesis. The engine is operated on a stoichiometric combustion strategy by controlling the air/fuel ratio using feedback signals from a Heated Exhaust Gas Oxygen (HEGO) sensors. The engine is configured with side-mounted solenoid fuel injectors and the injection pressure was varied using an integrated solenoid valve controlled by the ECU depending on the engine operating condition.

A 75-kW alternating current (AC) dynamometer was connected to the motor to monitor and control engine load and rotational speed. The engine test cell is shown in Figure **3.1**, below. In-cylinder pressure was monitored and recorded in all 4 cylinders using AVL GM12D miniature piezo-electric pressure transducers. A Baumer 720 pulse per revolution magnetic encoder was utilised to calibrate the AVL piezo-electric pressure transducers to the engine cycle. Pressure signals were recorded every 0.5 crank angle degree (CAD) over 200 cycles and acquired using a LabView software with a National Instruments (PCI-MIO-16E- 4) board for data collection. To import and process the data collected from the various data acquisition sources, a bespoke post-processing script was written in Matlab. Engine combustion parameters such as in-cylinder pressure and heat release rate (HRR) were measured and analysed with the help of this Matlab code to provide a comprehensive picture of the combustion process. A Rhenonik RM015 Coriolis fuel metre was utilised to quantify the amount of gasoline fuel used. To track oxygen levels, a Heated Exhaust Gas Oxygen (HEGO) sensor was employed. The experimental apparatus and engine specifications are listed in Table **3.1**.

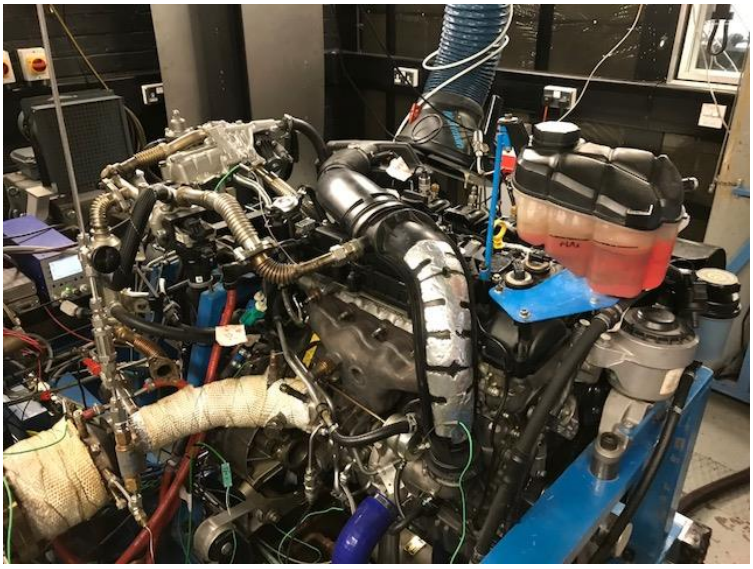


Figure 3.1: 4-cylinder GDI engine test bench.

Table 3.1: 4-cylinder GDI engine specification.

Compression ratio	10:1
Bore x Stroke	87.5 x 83.1 mm
Turbocharger	Borg Warner k03 with variable wastegate
Swept volume	2,000 cc
No. of cylinders	4
Rated Power	149 kW at 6000 rpm engine speed
Rated Torque	300 Nm at 1750-4500 rpm engine speed
Engine Management	Bosch ME17
Fuel measurement	Recorded by a Rheonik RM 015 sensor and maintained at 28^{o}C
Control unit	Cadet control system supplied by *CP Engineering*

3.2. Three-Cylinder Engine Test Bench

A 1.5 L, 3-cylinder, turbocharged research gasoline engine manufactured by Ford was also used during this research study, a schematic view of the engine and test apparatus is shown in Figure 3.2. The engine can be run with dual injection mode, DI and PFI of gasoline fuel, although only DI mode was used in this study. Table **3.2** summarizes the basic engine specification. The engine is equipped with Kistler PiezoStar water-cooled pressure sensors (Type 6045B-2-3), which are installed in each cylinder head. The AVL Rotary Encoder 366C was used for the shaft encoder. In order to collect in-cylinder pressure measurements in real-time, a pressure sensor and a shaft encoder were utilised.

Table 3.2: GDI Engine specifications and associated apparatus.

Engine type	**Spark-ignition, 3-cylinder**
Charged method	Turbocharged
Compression ratio	11:1
Swept volume	1497 cc
No. of cylinders	3
Rated Power	134 kW at 6000 rpm engine speed
Rated Torque	240 Nm at 1600-4500 rpm engine speed



Figure 3.2: Three-cylinder gasoline DI/PFI engine test bench.

3.3. Fuels Used

The engines were operated using two fuels, a commercial EN228 fuel from Shell that has 5% (v/v) ethanol and a 99.95% neat methane from BOC that serves as a substitute for compressed natural gas. Table **3.3** details the fuel properties of the fuels used in this research study.

Table 3.3: Fuel properties for gasoline and methane gas.

	Gasoline	**Methane gas**
Elemental C-H-O	$CH_{1.93}O_{0.03}$	CH_4
Calorific value (MJ/kg)	41.65	50
Research octane number (RON)	95.8	>120
Density (kg/m^3)	746.6	0.657
H/C ratio	1.93	3.9
Oxygenates -Ethanol (%vol)	9.4	0

3.4. Gaseous and Particulate Emission Analysers

3.4.1. FTIR

Gaseous emission levels were measured using a MultiGas Fourier Transform Infrared Spectrometer (FTIR) 2100 MKS., in particular: oxides of Nitrogen (NOx), Carbon oxide (CO), Carbon dioxide (CO_2) and Total Hydrocarbon (THC) including hydrocarbons from C1 to C12. FTIR utilises the unique fingerprints of each gas constituent to verify the sample specie by using molecular infrared (IR) spectroscopy analysis. IR spectrum passes through the exhaust gas and depending on the sample's absorption it is reflected as the specific wavelength of a particular gas species. For CO, HC species, and NOx, the lowest detection limits are 1.2 ppm, 1 ppm, and 3.6 ppm, respectively. The exhaust gas was pumped via a heated line maintained at 190 ^oC to avoid the condensation of H_2O vapour and hydrocarbons. The optical lens of the FTIR is protected from harm by filtering the exhaust gas PM before it enters the instrument. Figure **3.3** depicts the FTIR analyser used in this research.



Figure 3.3: MultiGas FTIR 2100 MKS analyser.

3.4.2. SMPS

The particle distribution in this study was obtained using a TSI Scanning Mobility Particle Sizer (SMPS), a Differential Mobility Analyzer (DMA) and a Condensation Particle Counter (CPC) as shown in Figure **3.4**. Particle sizes ranging from 7.5 to 294 nm were obtained using flow rates of 10 l/min for the sheath and 1 l/min for the sample. Using a tiny radioactive source (Kr-85), the particles are neutralized before they enter the electrostatic classifier. In the DMA, a magnetic field controls the flow path of charged particles, and they are then separated based on their electrical mobility. The mono-disperse distribution is then sent into a CPC unit where the number of particles are counted based on their size.

In addition, an ejector diluter system was used in conjunction with the SMPS analyzer in order to dilute the sample and prevent the formation of moisture/HCs condensation. Air at 1 bar was used to dilute the samples and the dilution ratio was set at 10 for all experiments. Exhaust gas concentrations of NO and CO_2 were used to determine the DR, removing any experimental bias caused by the FTIR analyzer's detection limits, as shown in Equation 3.1.

$$\boldsymbol{Dilution\ ratio} = \frac{\boldsymbol{NO\ ppm_{exhaust}}}{\boldsymbol{NO\ ppm_{sample}}} \cong \frac{\boldsymbol{CO_2\%_{exhaust}}}{\boldsymbol{CO_2\%_{sample}}} \qquad \text{Equation 3.1}$$



Figure 3.4: Scanning Mobility Particle Sizer (SMPS) 3969.

3.4.3. TGA

To study the oxidation behaviour of the soot produced from the different fuelling conditions, a Perkin Elmer TGA model Pyris was used, shown in Figure **3.5**. First, the microfiber glass filters were cut into small discs and then placed in an alumina crucible. A user-defined program was then generated that consists of two phases: a) de-volatilisation phase where the sample is heated under inert atmosphere (nitrogen gas) to evaporate the volatile organic fraction (VOFs) and b) oxidation phase where air is used to oxidise the remaining soot at a heating ramp of 3 ^{o}C/min. The full TGA procedure is detailed in Table **3.4**.



Figure 3.5: Perkin Elmer Pyris 1 TGA analyser.

Table 3.4: TGA defined program.

No.	Time interval/Temperature	Gas
1	Sample held for 10 mins @ 40 ˚C	
2	Temperature increased by 3 ˚C/min to 400˚C	
3	Sample held at 400 ˚C for 30 mins	
		N_2 100ml/min
4	Temperature reduced by 3 ˚C/min to 200˚C	
6	Temperature increased by 3 ˚C/min to 650˚C	
7	Sample held at 650 ˚C for 30 mins	
8	Temperature reduced by 50 ˚C/min to 40˚C	
		N_2 60ml/min
9	Sample released for analysis	Air 40 ml/min

3.4.4. RAMAN

The crystalline nature and oxidative reactivity of the collected carbonaceous materials were analysed using Raman spectroscopy, as shown in Figure **3.6**. The Raman spectra from the sample were measured from 800 to 2000 cm^{-1} and were stimulated by an argon ion laser beam with an excitation wavelength of 532 nm. The spectra were analysed by employing a mathematical fitting technique based on a four-curve model, specifically the 3L1G technique (three Lorentzian bands and one Gaussian band). The average spectrum was calculated using data from five separate sample locations for each soot filter to ensure accuracy of results.



Figure 3.6: Renishaw inVia confocal Raman microscope.

3.4.5. TEM/HRTEM

The morphological images were acquired using a TalosTM F200X S/TEM equipped with an FEI Ceta 16MTM camera shown in Figure **3.7**. For statistical purposes, at least 25 photos of agglomerates were taken from each soot sample across a range of different locations. The evaluation of the different morphological characteristics such as primary particle diameter (dp0), radius of gyration (Rg), primary particle number (npo), and the fractal dimension (Df) was performed with the use of an in-house MATLAB script previously used and developed at The University of Birmingham. For each sample, a minimum of 180 primary particles were considered, from a variety of agglomerates, to ensure the accuracy of results as operator and grid position can affect the measurements taken. [34]. The nanostructural variables such as interlayer spacing (d002), fringe length (La) and tortuosity (τ) were analysed and quantified for the different fuelling conditions.



Figure 3.7: JEOL JEM-2100 Electron Microscope.

3.5. Catalyst Cores

Several catalysts of different sizes and compositions, supplied by Johnson Matthey, were investigated in this Thesis. Small-scale furnace tests were undertaken to evaluate the performance of three palladium/rhodium catalysts in removing gaseous emissions. The catalysts had different loadings of Low (L), Medium (M) and High (H) PGM of 50, 150 and 200 g ft^{-3} respectively. Additionally, a full-scale Pd/Rh catalyst with PGM loadings of 150 g ft^{-3} and a Pt/Rh catalyst with equivalent price loading to Pd were also examined under engine cyclic lambda variation. The detailed characteristics of the catalysts used in this research study are presented in Table **3.5**. The full-scale catalysts are depicted in Figure **3.8**.

Table 3.5: Catalyst specifications.

Catalyst code	**Dimension (in)**	**PGM total loading (g ft^{-3})**	**PGM content**	**PGM ratio**
L	ϕ1x5	50	Pd:Rh	47.5: 2.5
M	ϕ1x5	150	Pd:Rh	142.5 : 7.5
H	ϕ1x5	200	Pd:Rh	190 : 10
A	ϕ4.66x4.5	150	Pd:Rh	142.5 : 7.5
B	ϕ4.66x4.5	278.5	Pt:Rh	271 : 7.5



Figure 3.8: Full scale catalysts used in this research

4. Performance of Different Loaded PGM Catalysts for Dual-Fuel Engines

4.1. Introduction

No study to date has investigated the performance of the aftertreatment system designed for dual-fuel gasoline-CNG engines, with all studies either limited to combustion analysis of the dual-fuel or for dedicated CNG fuelled engines. As such, the main aim of this chapter is to fill the literature gap in the aftertreatment system of dual-fuel engines by investigating the effect of real engine exhaust gas on the performance of CNG catalysts especially in reducing CH_4 emissions, under different fuelling compositions. The dual-fuel injection of methane-gasoline provides an alternative solution for vehicle manufacturers to meet future emission targets, possibly using only a CNG catalyst. If the dual-fuelling strategy yields beneficial results, then the possibility of additional engine research and development should be examined.

4.2. Experimental Procedure

The engine was operated at idle conditions for 20 minutes to reach operational coolant and oil temperatures of 90 ± 1ºC and 95 ± 2ºC respectively, to avoid cold start effects and minimise emission fluctuation. During the tests, the engine speed was maintained at 2100 ± 2 rpm and load of 30 ± 2 Nm corresponding to a low load condition for vehicles. The level of gasoline substitution by methane was evaluated under three different conditions: 0% (M0), 20% (M20), and 40% (M40) replacement. Gasoline fuel was directly injected into the combustion chamber while methane gas was introduced via port-injection. The temperature and flow rate of methane gas were monitored throughout the experiment to ensure there was no significant variations in density. The engine apparatus used in this study is shown in Figure **4.1**.

Pd/Rh coated catalyst with different PGM content was used in this study, supplied by Johnson Matthey as detailed in section 3.5. The catalysts were installed in a reactor within a tubular furnace (Figure 4.2) and fed with exhaust gas from the engine. The temperatures pre and post the catalyst were monitored using K-type thermocouples installed at the reactor's intake and outlet. Prior to testing, the engine was warmed up to minimise emission fluctuations and assure consistent results. A pump and a

flowmeter located downstream of the reactor's outlet were used to maintain a consistent flow rate of 1.16 m^3/h over the catalyst and achieve a gas hourly space velocity of 30,000 h^{-1+}. A one-way valve was installed to prevent the build-up of back pressure. Moreover, in order to reduce the impact of daily variability, all experiments were performed on the same day.

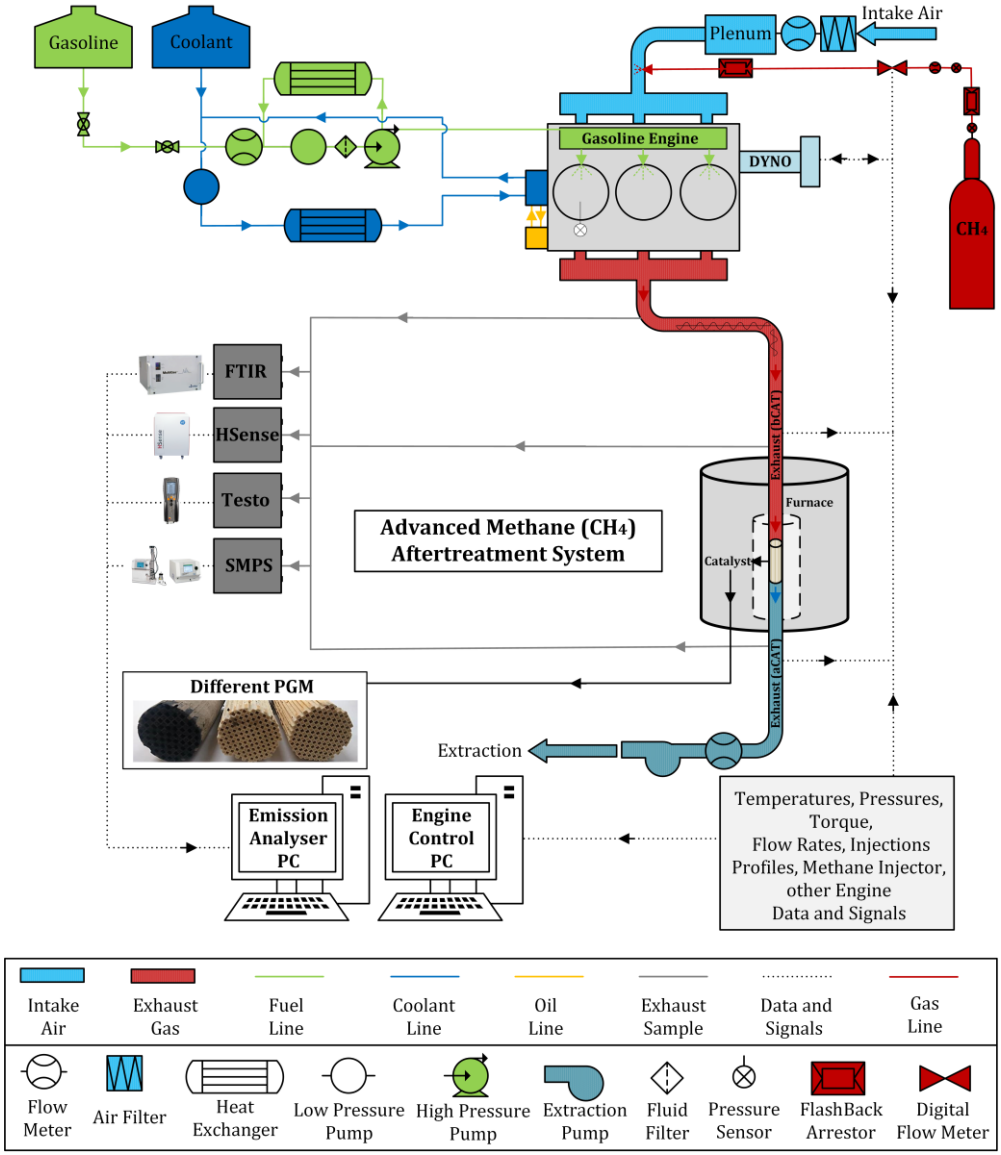


Figure 4.1: Engine apparatus, testing and analysis schematic.



Figure 4.2: Tubular furnace and reactor used in the experiments.

4.3. Results and Discussion

4.3.1. Combustion Studies

Engine-out emissions from vehicles with different fuelling compositions can be fairly compared by adjusting the spark timing to phase the combustion and maintain a constant MFB50%. The slower laminar flame speed velocity of methane gas promotes a slower flame propagation rate leading to a longer combustion duration compared to the gasoline mode [50, 51]. Thus, the spark timing was slightly advanced when the methane proportion was increased with respect to only gasoline operation to achieve equal MFB50%. As a result, the maximum in-cylinder pressure (P_{max}) of M0, M20 and M40 fuelling conditions were identical, while the heat release rate (HRR) reduced with the addition of methane to the combustion chamber as seen in Figure **4.3**. The start of combustion started earlier with M20 and M40 and the prolonged compression stroke resulted in higher in-cylinder temperature as demonstrated in the HRR profile. Additionally, the improvement in engine combustion was also reflected in the reduction of COV of the indicated mean effective pressure (IMEP) as shown in Table **4.1**. The gaseous methane fuel increases the stability of the combustion process by increasing the homogeneity of the air-

fuel mixture and by mitigating the effects of insufficient liquid fuel evaporation under low load conditions [52-54].

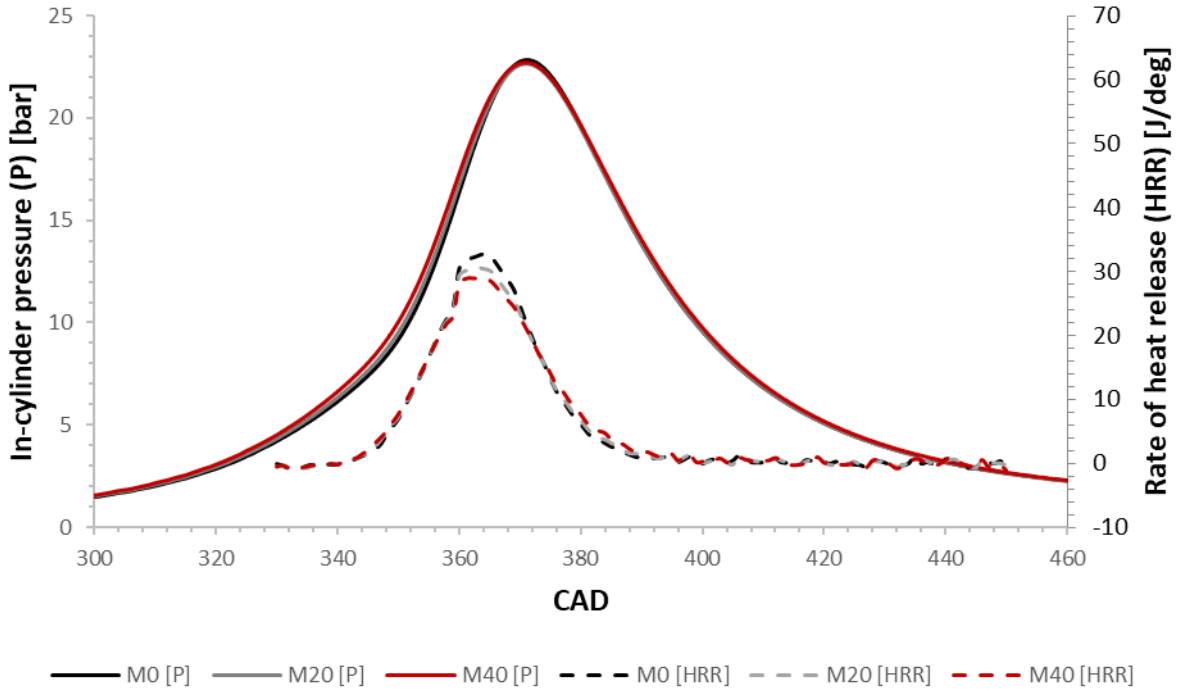


Figure 4.3: Corresponding in-cylinder pressure and HRR for M0, M20 and M40 test conditions.

Table **4.1** details the brake specific fuel consumption (BSFC), thermal efficiency (T.E.), COV of IMEP and engine exhaust temperatures of the studied fuel compositions. The addition of 20% methane reduced the BSFC by 4.5% compared to the baseline gasoline-mode due to the higher mass-based heating value of methane while the addition of 40% methane led to 5.3% reduction in fuel consumption (55). This is also highlighted with the increase in T.E. of the engine with the addition of methane. Further optimization of spark timing for natural gas operation can lead to even higher improvements in terms of fuel consumption. The higher-octane quality of natural gas reduces the knock intensity of the engine, thus enabling the spark timing to be more advanced and the combustion phasing maintained close to peak efficiency. This would be particularly beneficial at higher loads eliminating the need for

fuel enrichment (running rich of stoichiometry) needed to protect engine hardware from excessive temperatures [55-57].

Table 4.1: Engine parameters for the different CNG replacements

Methane Replacement (%)	**BSFC (g/kWh)**	**T.E. (%)**	**COV of IMEP**	**Exhaust Temperatures (°C)**
0%	343.5	24.83	1.565	495
20%	328.3	26.00	1.28	492
40%	325.2	26.23	0.88	487

4.3.2. Emissions Upstream the Catalysts

The exhaust emissions resulted from the combustion of the dual-fuel engine are demonstrated in Figure **4.4**. Depending on the amount of methane in the fuel blend, different emission levels were observed during the combustion of the dual-fuel. A significant reduction in CO emissions were resulted with methane fuelling dropping by 30% and 54% with M20 and M40 respectively compared to the baseline gasoline mode. Additionally, because of the simpler chemical structure of methane and its lower carbon content compared to gasoline, less CO_2 emissions were emitted [57-59].

With the increase of methane utilisation, lower unburned non-methane hydrocarbons (NMHC) emissions were produced compared to the gasoline mode. The more homogenous air-fuel mixture of the dual-fuel mode resulted in a more complete combustion and a subsequent reduction in unburnt fuel [60]. Moreover, the decrease in the direct-injection of the gasoline fuel reduces the liquid fuel impingement into the cylinder walls reducing wall quenching and resulting in lower CO, CO_2 and NMHC emissions [60].

Conversely, engine-out methane emissions exhibited a contrasting trend to non-methane hydrocarbons and CO_2 emissions. With the increase in methane fuel utilisation, CH_4 emissions increased by up to 500 ppm with M40, mainly due to non-combusted methane escaping the combustion chamber. The high global warming potential of methane (25 times greater than CO_2 over a 100 year time frame) may offset the benefits attained by methane utilisation when taking the CO_2-equivalent emissions into consideration. This makes it essential for the development of an efficient aftertreatment system that can efficiently oxidise CH_4 in the dual-fuel system in order to maximise the potential of this strategy (to be discussed further in section 4.3.3.2). On the other hand, there was a slight increase in NO emissions with the dual-fuel mode. Improved fuel combustion and the higher methane adiabatic flame temperature increases the engine's in-cylinder temperature, which promotes NO generation [60].

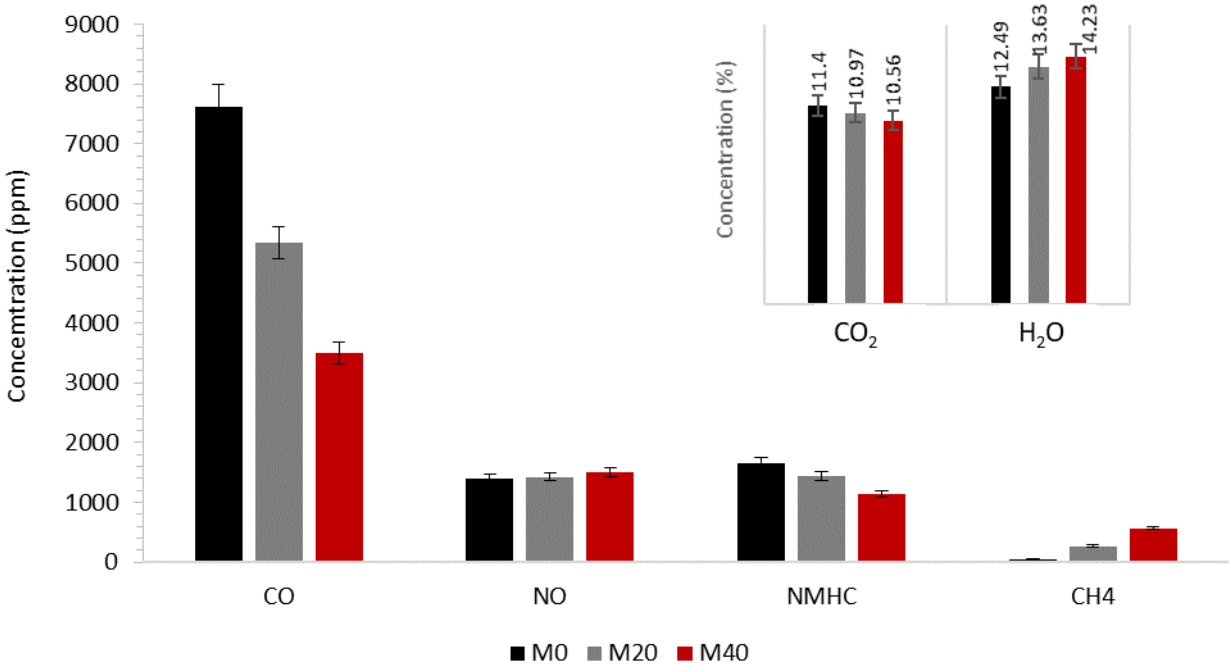


Figure 4.4: Engine-out emissions with different methane % replacement.

4.3.3. Impact of PGM ratio and Methane Replacement on Catalytic Activity

4.3.3.1. Regulated Gaseous Emissions

The catalyst light-off profiles for the gaseous emissions for both M0 and M40 engine fuelling conditions are shown in Figure **4.5**, M20 was not studied in these set of experiments. Light-off tests were carried out using Low (L), Medium (M) and High (H) PGM catalysts with loadings of 50, 150 and 200 g ft^{-3} respectively.

In a TWC, hydrogen and CO act as the reducing agents of NO with the selectivity being temperature dependent [65-66]. There are two conversion windows of NO observed across the catalysts for M0 fuelling condition. Firstly at low temperatures (<200ºC) favouring the reduction of NO by H_2, which reacts with the adsorbed oxygen atoms to produce N_2O [66]. Then at temperatures (>200ºC) another reduction pathway takes place through reactions with CO, with the selectivity of hydrogen towards NO decreasing as it is oxidised by O_2 instead. The same reactions also occur with M40 fuelling, however an additional NO conversion window is observed in this case. At higher temperatures (>240 ºC) the catalysts demonstrated a slower NO conversion rate with M40 compared to M0. This is attributed to the lower concentration of CO available from engine combustion to participate in NO reduction with the M40 fuelling, which is the governing reaction pathway at these temperatures. The ratios of the exhaust reductants and oxidants species are key for catalytic reactions in a three-way catalyst (TWC), and a balance is therefore needed for its efficient operation [67]. As shown in Figure **4.5** for the M40 case, CO emissions are completely oxidised, however there is still approximately 350 ppm of NO present in the exhaust. This excess NO then reacts with another reducing agent, methane which has a similar role to CO in removing the oxygen from NO dissociation on the Pd sites [66-68].

On the other hand, light-off catalyst temperatures for THC was significantly delayed with M40, compared to M0 which is attributed to the higher concentrations of CH_4 present in the exhaust gas. Methane constitutes approximately half of the THC concentration in the M40 exhaust and is the most difficult hydrocarbon to oxidise , thereby shifting the light-off to higher temperatures [see section 4.3.2].

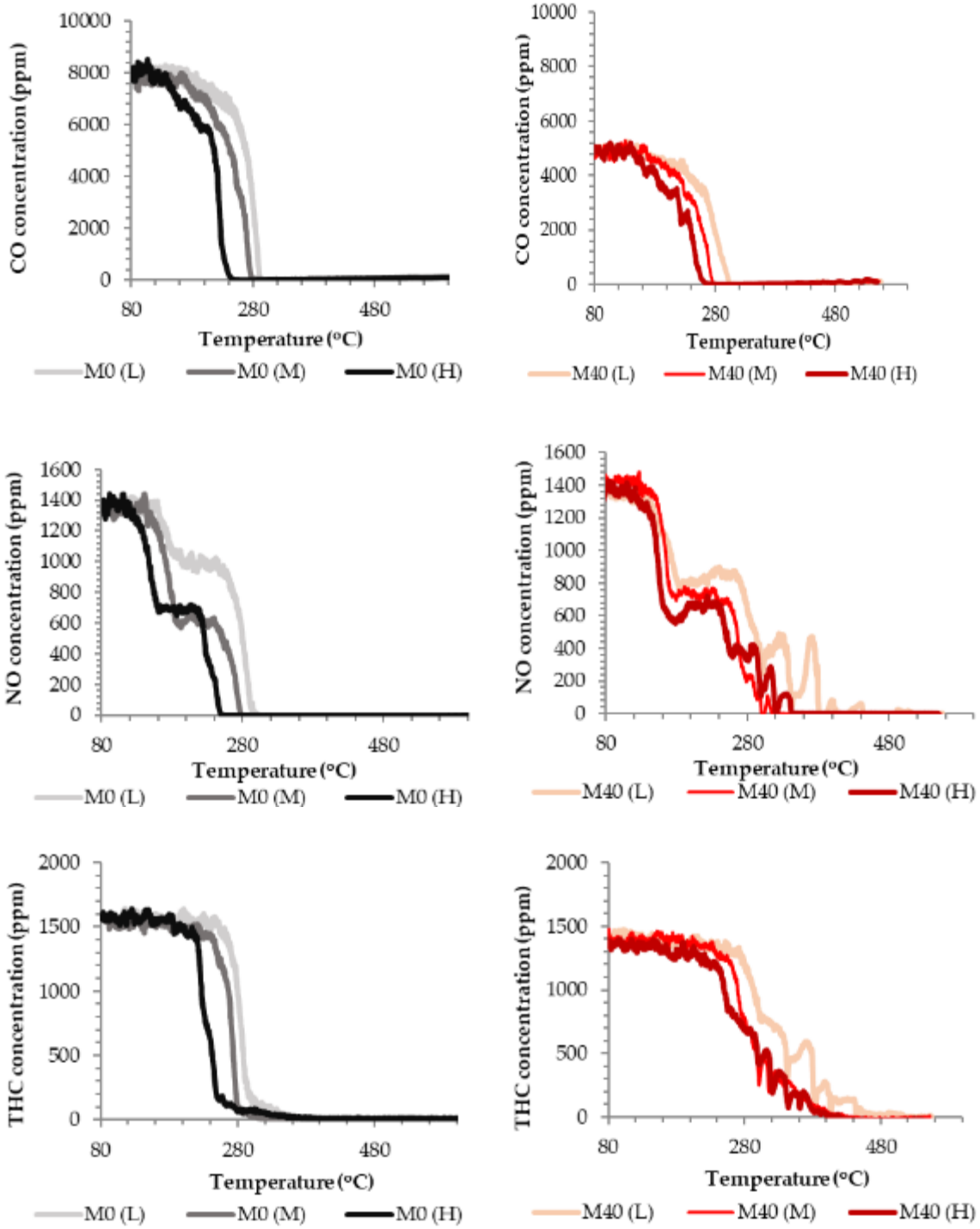


Figure 4.5: Catalyst light-off activity for regulated emissions for M0 and M40.

The effect of increasing the catalyst PGM loading on the regulated emissions light-off temperature is shown in Figure **4.6**. Catalysts with higher PGM demonstrated a faster conversion rate than lower PGM catalysts. CO, NO and THC light-offs were enhanced by approximately 50, 110 and 50ºC respectively when using the highest PGM catalyst. This indicates that NO is significantly more sensitive

to PGM loading, specifically Rhodium (Rh), than other exhaust emissions. The difference in $T_{50\%}$ of NO between the catalysts with 200 and 150 g ft^{-3} is significantly lower than the catalyst with loading of 50 f ft^{-3} indicating that although increasing the Rh loading has a positive effect on the low-temperature activity of the catalyst, the benefit seems to diminish at PGM > 150 g ft^{-3}. Noble group metals are known to be expensive, with Rhodium being 5-6 times more costly than Pd and Pt [69], therefore careful economic consideration has to be taken into the optimisation of these noble metal catalyst to reduce the cost while still attaining a relatively faster light-off temperature.

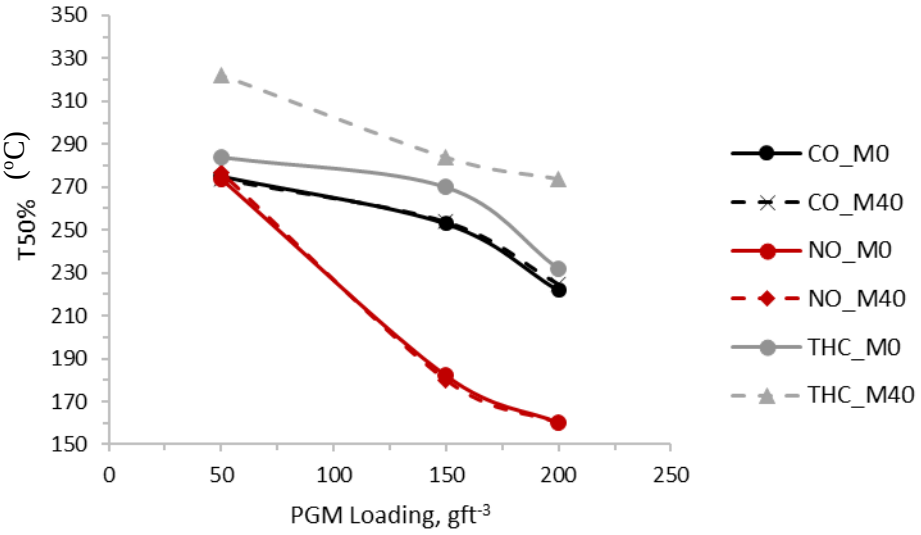


Figure 4.6: Regulated emissions light-off temperature vs PGM loading.

4.3.3.2. Methane Light-off Study

Figure **4.7** demonstrates the light-off profile of methane for M0 and M40 respectively. Comparing the two fuelling conditions, there are insignificant differences between CH_4 light-off temperatures for M0 and M40 as both curves superimpose perfectly, despite the significantly higher CH_4 concentration present in the engine exhaust with M40 fuelling. This indicates that the catalyst's ability to oxidise methane is more dependent on temperature rather than fuel composition i.e. regardless of the concentration of CH_4 flowing through. Moreover, CH_4 conversion starts right after CO depletion through reaction with NO as explained in the previous section. Some studies have shown that CO acts as an inhibitor for CH_4 conversion which is also observed in this study (66).

It is well accepted that among precious group metals, palladium (Pd) have the greatest effect on the conversion of CH_4 followed by platinum and rhodium [69-71]. Generally, the active phase for methane oxidation is known to be PdO [66, 72], however under stoichiometric natural gas vehicles (NGV) exhaust gas conditions, metallic Pd are the predominant active species [72]. The reactivity of metallic Pd is controlled by competitive adsorption of methane and oxygen at the surface in a Langmuir–Hinshelwood mechanism [67]. Hence, in order to oxidise the highly stable methane bond at lower temperatures the use of Pd loading is essential in the aftertreatment system.

The results from Figure **4.8** indicate that increasing the Pd loading led to significantly earlier light-off temperatures for CH_4 for both fuelling conditions. Methane light-off temperature for both fuelling conditions was in the order of approximately 340, 350 and 395°C for High, Med and Low PGMs respectively. However, the benefit diminishes above Pd loading >142.5 g ft, which suggests that the effect of Pd on CH_4 conversion had reached a plateau as shown in Figure **4.8**. These results are promising compared to various other catalyst formulation reported in the literature [71]. A point to note is that the high efficiency of Pd is only activated within a quite narrow operating window due to its sensitivity towards oxygen [72]. This makes the control of air-fuel ratio for stoichiometric dual-fuel gasoline engines vital for the efficient operation of its aftertreatment system.

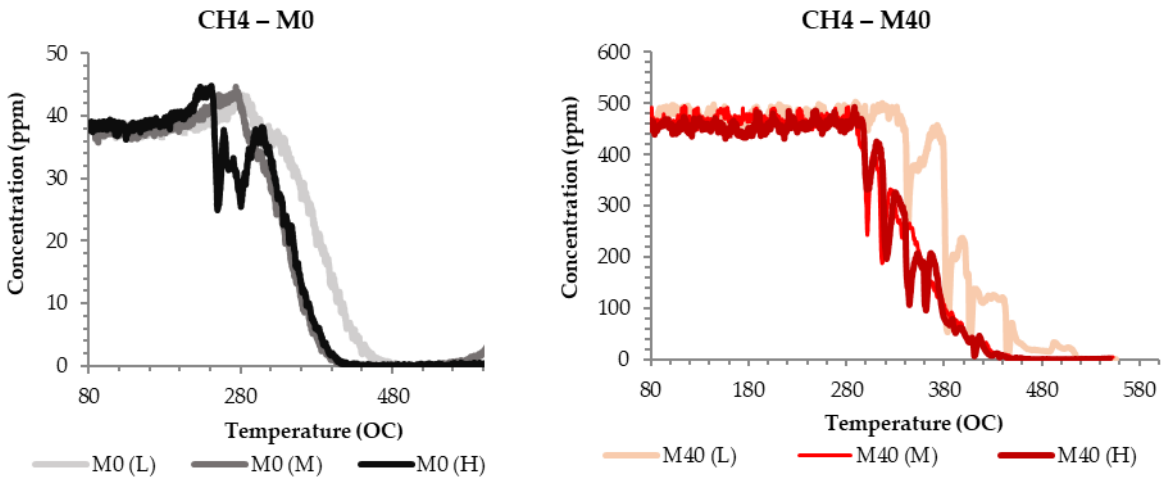


Figure 4.7: Light-off activity of CH_4 for M0 and M40 at different PGM loadings.

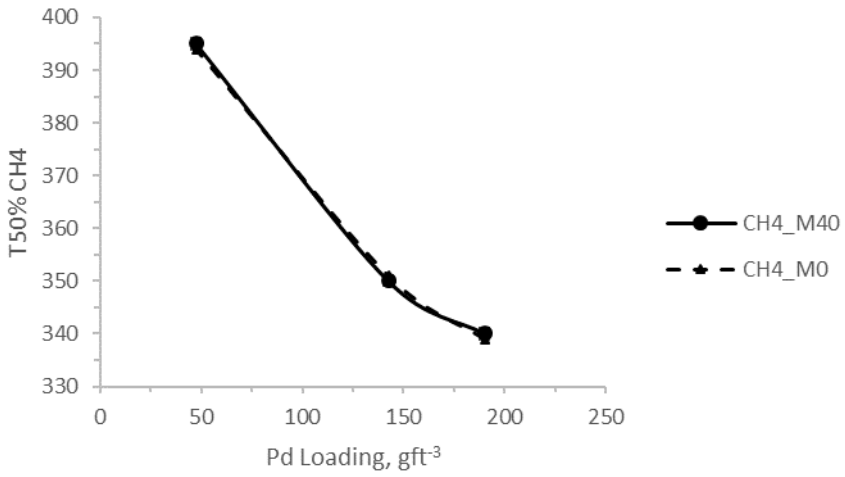


Figure 4.8: CH_4 light-off temperature vs Pd loading.

4.3.3.3. Catalyst Impact on Non-Methane Hydrocarbon

Hydrocarbon reactivity is governed by their respective molecular structure and carbon numbers. It is well documented that short-chain hydrocarbons have lower oxidation activity as they require higher energy to detach their stable C-H bond as opposed to longer chain hydrocarbons. The oxidative reactivity decreases in the following order: alcohols > aromatics > alkynes > alkenes > alkanes [73, 74].

Figure **4.9** demonstrates the pre-catalyst concentrations of NMHC for both M0 and M40 case. In general, less non-methane hydrocarbons (NMHCs) were resulted from M40 combustion compared to M0. Propane is the highest NMHC produced with over 225 ppm present in M0 and 125 ppm in M40, followed by ethylene (70 ppm, 45 ppm) and toluene (70 ppm, 30 ppm). Small concentrations of oxygenated hydrocarbons acetaldehyde and formaldehyde were found pre-catalyst but were completely oxidised at temperatures <300ºC. These species are harmful to humans as they are classified as carcinogenic so their aftertreatment control is vital. Some HCs are known to inhibit the oxidation of CO and reduction of NO over a TWC by occupying the catalyst active sites [69, 73]. Traces of propylene (also known as propene) were found in the engine exhaust, approximately 40 ppm for M0 and 20 ppm for M40. It has been reported that propylene has a promoting effect on NO reduction over a Pd/Rh catalyst [69] which could explain the inferior oxidation activity of NO for M40.

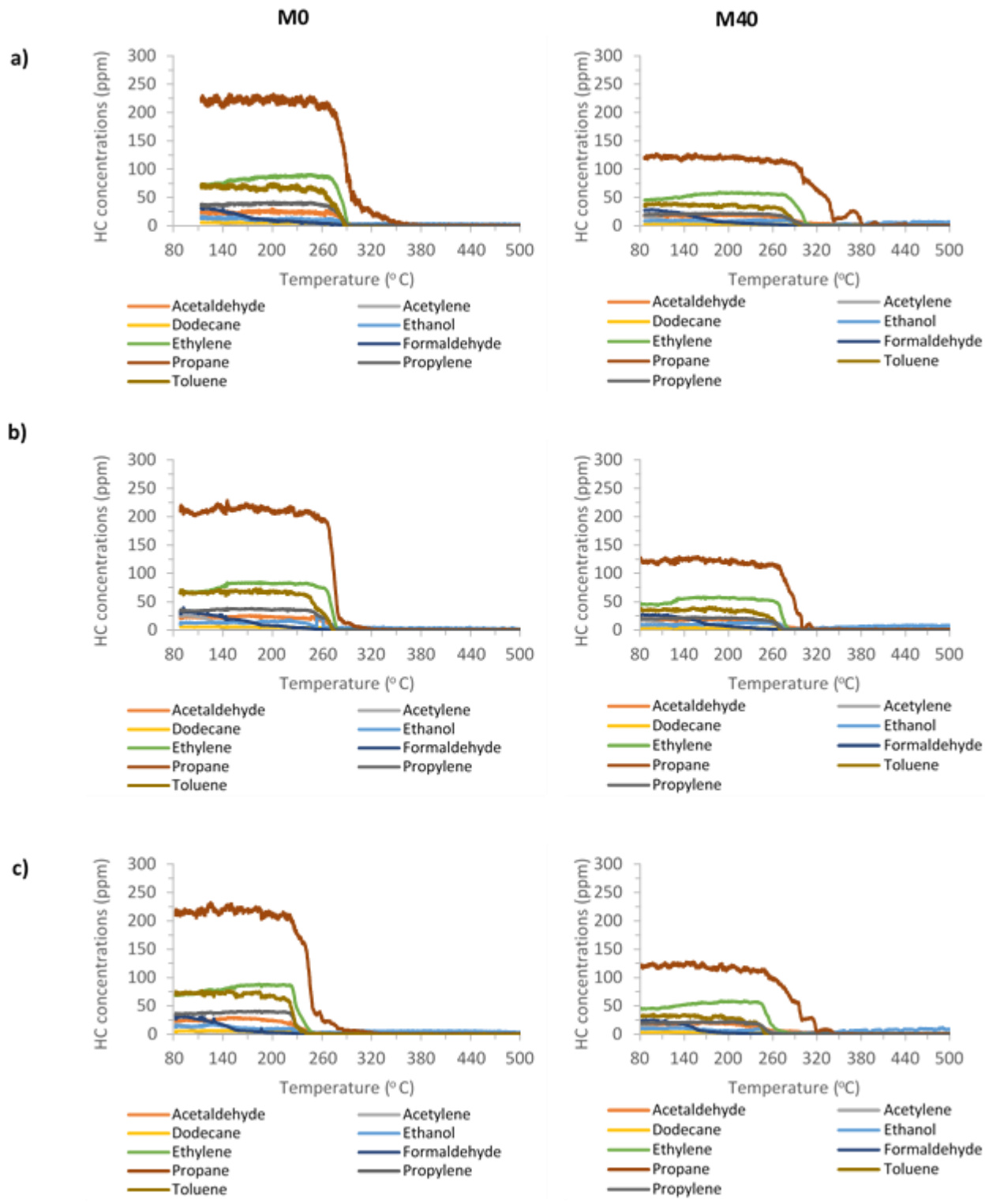


Figure 4.9: NMHC light-off activity for M0 and M40: a) High PGM, b) Med PGM and c) Low PGM.

The light-off temperatures of most HCs were slightly delayed in the M40 fuelling compared to M0 with Propane being the HC most affected. The oxygen concentration from the dual-fuel mode was lower compared to the gasoline mode as more oxygen is consumed in the combustion phase to oxidise the injected methane. This resulted in lower concentrations of O_2 that can undergo HC oxidation reactions over the catalyst. On the other hand, increasing the PGM loading led to faster light-off temperatures for all the NMHC species in both fuelling conditions.

4.3.3.4. Ammonia and N_2O formation over CNG Catalyst

Several studies conducted on gasoline-NG engines have shown that three-way catalysts are the main cause of high levels of tailpipe ammonia emissions [75, 76]. Moreover, the level of NH_3 is highly impacted by the operating condition and air/fuel ratio with the highest level occurring during rich driving conditions. The formation of ammonia (NH_3) depends on the kinetic behaviour and chain effect of the different reductants and oxidants species in the exhaust and their interaction over the TWC as shown through equations (1-4) [66, 69, 75-79].

$$2NO + 5H_2 \rightarrow 2NH_3 + 2H_2O \quad \text{Equation 4.1}$$

$$2NO + 2CO + 3H_2 \rightarrow 2NH_3 + 2CO_2 \quad \text{Equation 4.2}$$

$$2NO + H_2 \rightarrow N_2O + H_2O \quad \text{Equation 4.3}$$

$$2NH_3 + 4NO \rightarrow N_2O + 3H_2O + 2N_2 \quad \text{Equation 4.4}$$

$$CO + H_2O \rightarrow CO_2 + H_2 \quad \text{Equation 4.5}$$

$$CH_4 + H_2O \rightarrow CO + 3H_2 \quad \text{Equation 4.6}$$

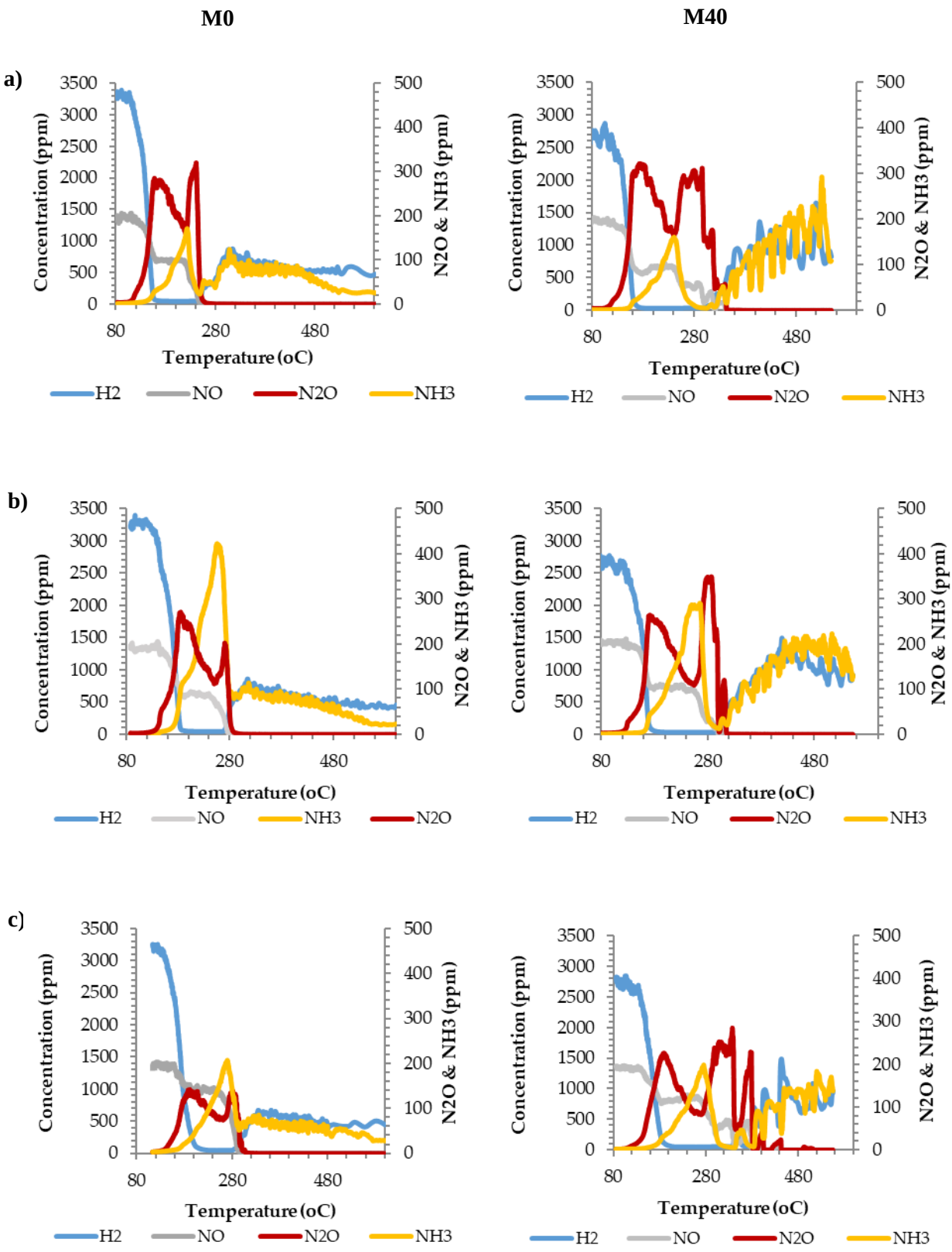


Figure 4.10: Ammonia slippage and by-products for M0 and M40: a) High PGM, b) Med PGM, c) Low PGM.

Figure **4.10** displays the ammonia formation over the CNG catalysts for the different PGM loadings and fuelling conditions along with levels of H_2, NO and N_2O, the by-products of NH_3 formation/oxidation. NH_3 is formed over the catalyst via the reaction of NO with H_2 (Eq 4.1), whereby the H atoms removes the O atoms from the dissociation of NO before further reacting with the N atoms [75, 76, 78]. An alternate reaction pathway can occur via further reaction with CO (Eq 4.2), which helps in NH_3 formation through its participation in the removal of O atoms, thereby facilitating the direct reaction of H atoms with N atoms and also through the intermediate hydrolysis of isocyanic acid (HNCO) [78]. However NO reduction can also lead to another pathway forming N_2O instead, with the selectivity depending on temperature and the kinetic reactions of the different species. As demonstrated in Figure **4.10**, initially NO reacts with H_2 at approximately 100^{o}C to form N_2O (Eq 4.3). The selectivity of the catalyst then changes momentarily to form NH_3 within a narrow temperature window 180 – 280^{o}C before changing back again to N_2O. This indicates that the selectivity of the catalyst towards NH_3 formation at low temperatures occurs only within a narrow temperature window provided that enough H_2 is available to undergo NO reduction. Ammonia levels then reduce either through oxidation by O_2 or through NH_3 decomposition via (Eq 4.4) [78, 79].

Considering the M0 fuelling condition at high temperatures (>300^{o}C), NH_3 concentration stabilizes following a sharp decrease. This is attributed to water gas shift (WGS) reactions (Eq 4.5) which increases the availability of H_2 to take part in NH_3 formation via (Eq 4.1) [77]. With further increase in temperature, the amount of H_2 reduces due to the more favourable reactions with O_2 and the WGS equilibrium constraint at higher temperatures (77, 78]. This subsequently reduces the NH_3 concentration gradually to 25 ppm as observed in Figure 4.10Figure 4.10. Conversely, for the M40 fuelling condition higher NH_3 levels are seen at high temperatures with concentrations stabilising at 150-200 ppm. Apart from the WGS reactions, the higher levels of CH_4 in the exhaust stream resulted from M40 combustion means more methane was available to undergo steam-reforming reactions (Eq 4.6), thereby producing higher H_2 concentrations [79]. This additional H_2 produced increases the formation of NH_3 in the high temperature region (>300^{o}C). The high level of ammonia slippage in the dual-fuel mode presents a

challenge due to the health risks these emissions impose and hence aftertreatment SCR technology should be adopted to remove them.

For both fuels, an NH_3 peak was observed at different low temperatures (<300ºC) depending on the PGM content with the reactivity following the order: High PGM > Medium PGM > Low PGM. The peak concentration of NH_3 produced differs across the three catalysts with the highest concentration produced across the Medium PGM catalyst (400 ppm) followed by Low PGM (200 ppm), while High PGM resulted in the lowest peak level of NH_3 (150 ppm). Comparing the effect of PGM content at high temperatures (>300ºC), there is no difference between the activities of the three catalysts with all three curves super imposing each other. Hence, the effect of PGM loading on NH_3 is only apparent at low temperatures.

4.4. Summary

The potential of a dual-fuel methane-gasoline strategy mode on the performance of a spark-ignition gasoline engine and the efficiency of novel CNG catalysts was investigated. The study has effectively addressed one of the major challenges of the dual-fuel system reported in the literature, that of the tailpipe methane emissions. The different PGM loaded CNG catalysts effectively reduced the engine-out exhaust emissions, especially the higher concentration of methane from the dual-fuel combustion at relatively lower temperatures. The light-off temperature for methane was achieved at 340, 350 and 395ºC for High, Med and Low PGMs respectively. However, another challenge was identified in the study resulted from the dual-fuel mode. High concentrations of ammonia emissions were produced over the catalyst which were primarily formed from steam-reforming reactions due to the increased level of methane in the exhaust stream. Therefore, further research into dual-fuel strategy development coupled with SCR technology should be conducted in the future to deal with these harmful ammonia emissions. The results from the study further demonstrated that the dual injection mode can achieve improvements in terms of better fuel economy, lower NMHC, CO and CO_2 emissions compared to the GDI mode. This is attributed to the more homogenous mixture and complete combustion with the introduction of the gaseous fuel. In addition, the lower C/H ratio resulted in significantly lower PM emissions.

5. Full-Scale Aftertreatment Technologies for Dual-Fuel Engines

5.1. Introduction

Precious group metal three-way catalysts (TWCs) were introduced to regulate hydrocarbon (HC), carbon monoxide (CO), and nitrogen oxide (NOx) emissions from gasoline-powered automobiles. The vast majority of TWCs are made of Pd/Rh, with Pt making up just a small percentage. The aftertreatment system analysed in the previous chapter showed promising results in abating the harmful emissions from the engine exhaust, on a laboratory scale. It is therefore important to assess the performance of the system using full-scale NG catalysts with PGM loading of 150g, as concluded in the previous chapter. Pd/Rh catalysts have been more popular in recent years, thanks to reduced sulphur content in the fuel and better wash coat technology, as well as a >10-year trend of Pd being less expensive than Pt [88]. However, Pd has outpriced Pt in the last decade as its demand increased significantly. As such, the main aim of this chapter is to analyse and compare the performance of Pd and Pt catalysts especially in reducing CH_4 emissions under different engine lambda conditions. The outcome of this chapter will determine the feasibility of interchanging Pt and Pd in the aftertreatment system of CNG and gasoline vehicles. In addition, catalyst analysis study is extended to include their performance under different driving conditions, alternating from stoichiometric (stoic) to lean and stoic to rich. Finally, studies were undertaken to improve the engine's fuel economy while keeping tailpipe emissions to a minimum through the use of different air/fuel cycles. The performance of the catalyst under these cycles was studied and evaluated providing an indication of the benefits of such strategy for future research.

5.2. Experimental Procedure

Figure **5.1** shows a schematic diagram of the experimental apparatus utilised in this chapter. Engine warm up was conducted at idle conditions for 20 minutes to reach operational coolant and oil temperatures of 90 ± 1ºC and 95 ± 2ºC respectively. This was done to avoid cold start effects and ensure consistency of results. Engine speed and load were fixed at 2100 ± 2 rpm and 30 ± 2 Nm, respectively, for the tests, corresponding to a low load condition for vehicles. In this chapter only one methane fuel replacement mode was studied (M40) and compared to the baseline gasoline mode (M0) while ensuring the MFB50% remains the same between the two conditions. Periodic monitoring during the test were carried out to guarantee that the replacement ratio for methane gas did not change significantly due to temperature or flow rate fluctuations.

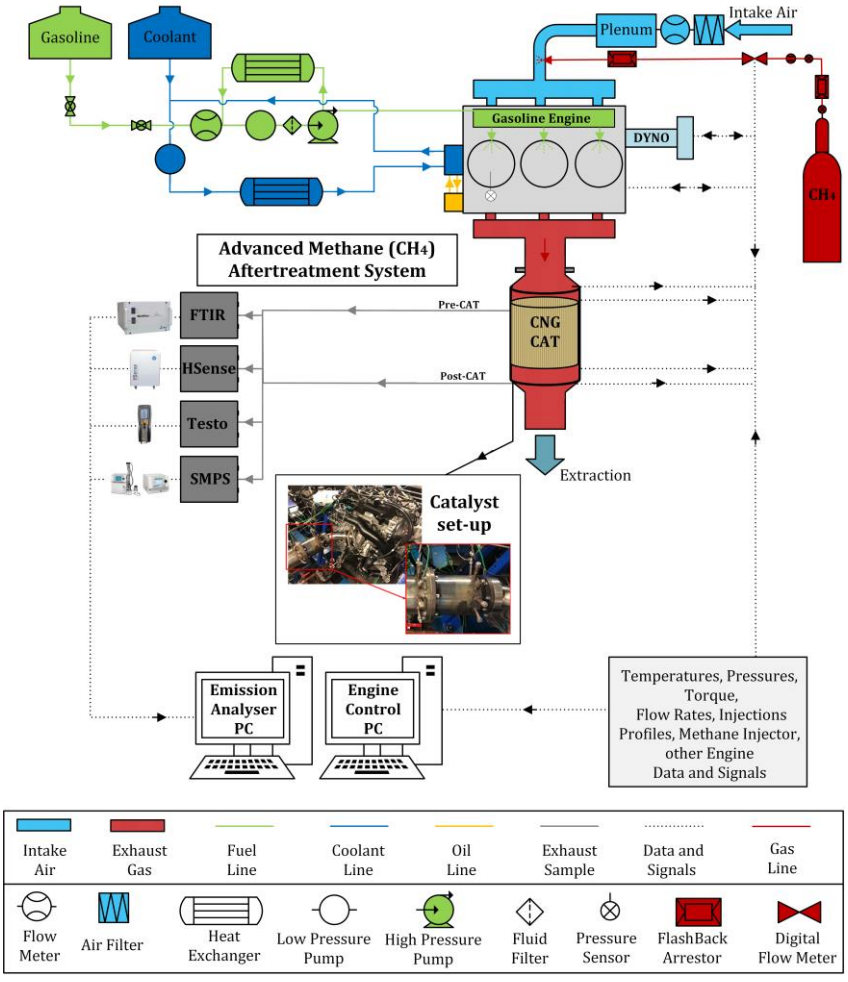


Figure 5.1: Experimental setup.

In this chapter, full scale CNG catalysts supplied by Johnson Matthey were installed on a canning and mounted on the GDI engine. The specifications of the catalysts used, including PGM content and PGM ratio are specified in Table **5.1**. The catalysts were placed in a furnace for 5 hours and regenerated at 600ºC prior to the test. Engine lambda was controlled by two lambda sensors positioned pre and post the catalyst and switched from stoichiometry (stoic) to rich and lean by changing the lambda parameters in the ATI vision software. For the cyclic air/fuel tests, a code was developed within the ATI software specifying the amplitude and duration of the lambda condition and linked to the engine control. An example of the cycle conditions undertaken in this chapter are presented in Figure **5.2**. Different Stoichiometric to Lean/Rich ratios were studied (5:1, 1:1 and 1:5) to understand the impact of each condition on catalyst performance and exhaust emissions. A combined cycle focusing on exhaust emissions and fuel economy simultaneously is then developed and assessed, examples of such cycle and durations are illustrated in Figure **5.3**. The fuel economy was calculated based on the BSFC Equation 6.1 for dual-fuel engines [87] and taking BSFC stoic as the baseline.

$$BSFC_{\ average} = \frac{T_R \times BSFC_{rich} + T_L \times BSFC_{lean}}{T_R + T_L} \qquad \text{Equation 5.1}$$

Where T_L and T_R are the durations of the cycle spent in lean and rich condition respectively.

Table 5.1: CNG catalyst specifications and their PGM loading

Catalyst	PGM content	PGM ratio	Dimensions
A	Pd:Rh	142.5 : 7.5	4.66 in. x 4.5 in.
B	Pt:Rh	271 : 7.5 (Pt price equivalent to Pd at the time of study)	4.66 in. x 4.5 in.

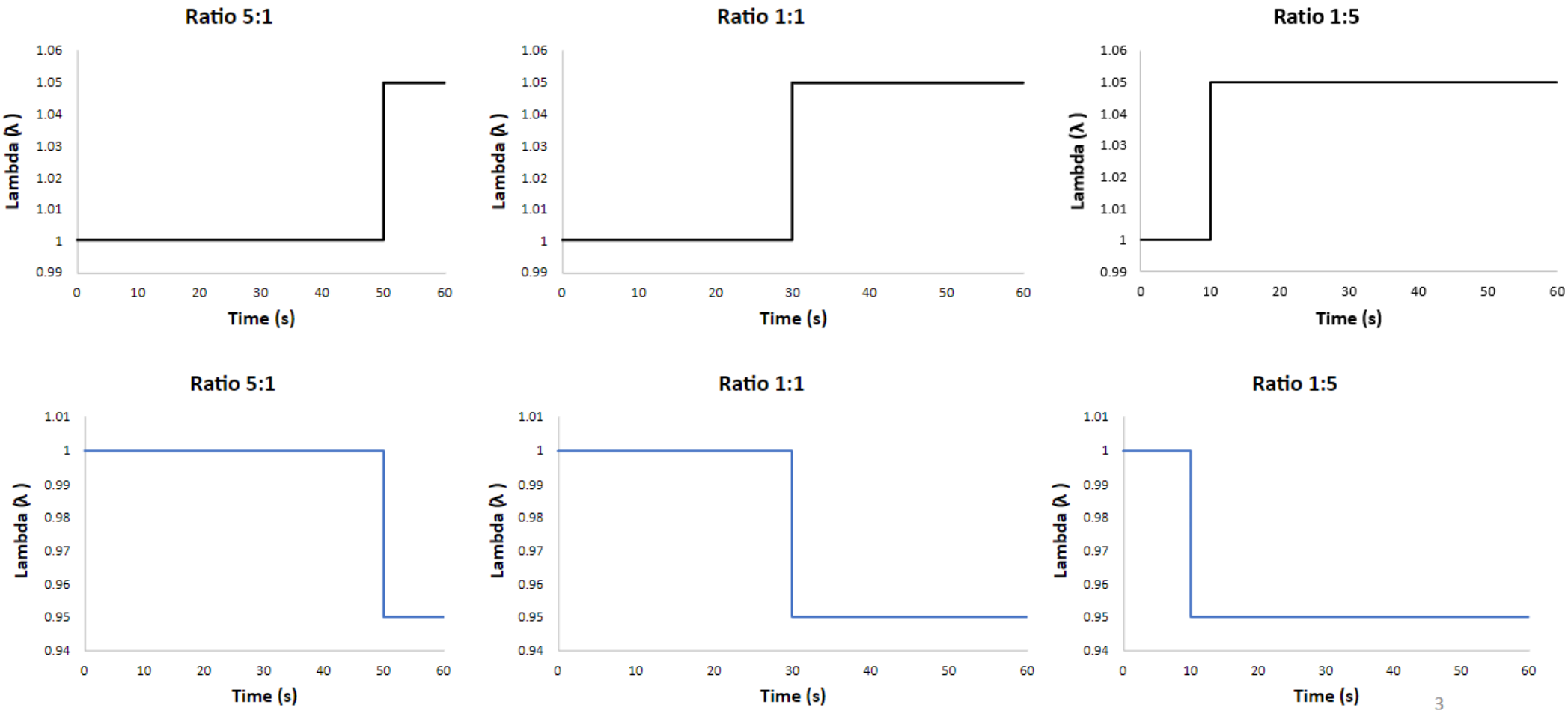


Figure 5.2: Stoichiometric to Lean/Rich cycle duration and ratio.

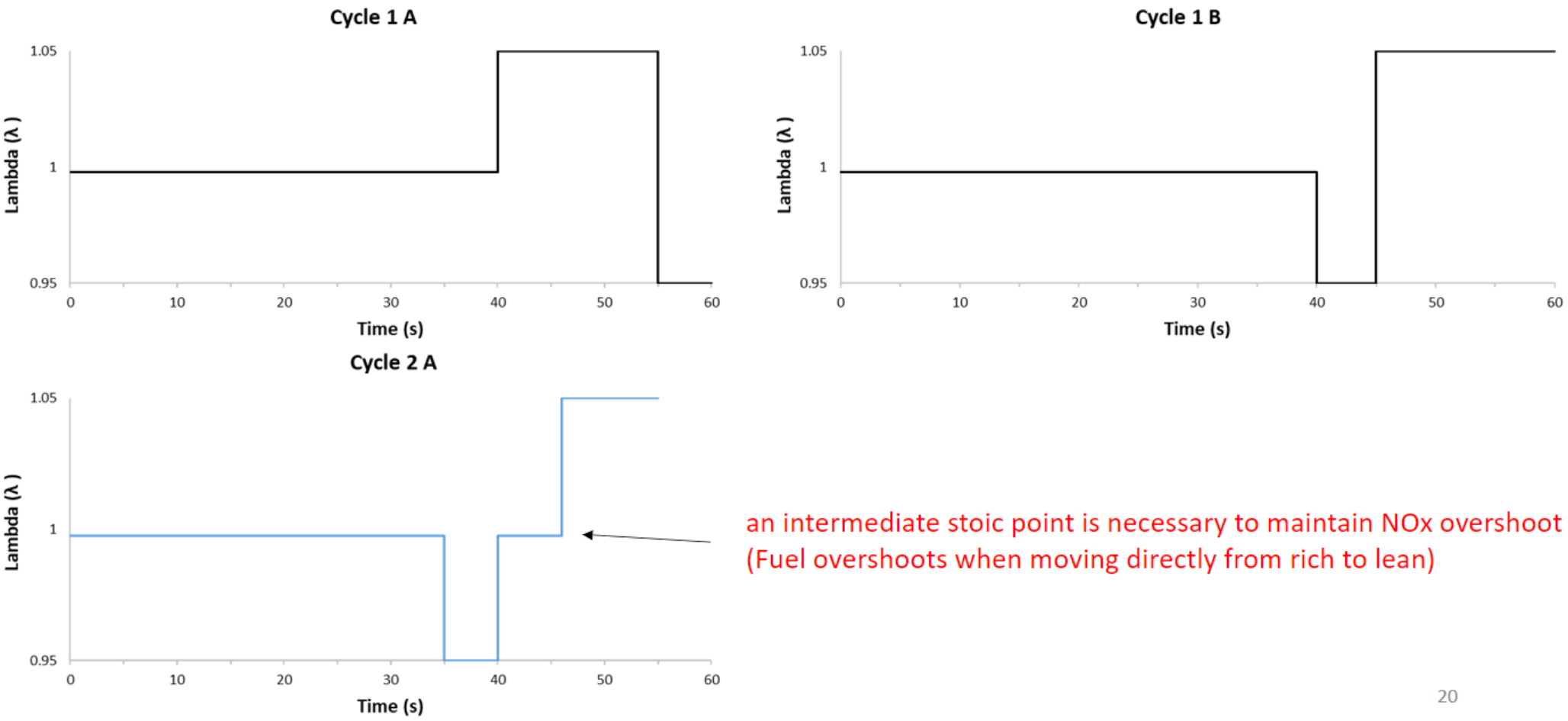


Figure 5.3: Combined Stoichiometric-Rich-Lean cycle for fuel efficiency.

5.3. Results and Discussion

5.3.1. Emissions Upstream the Catalyst

The exhaust concentration upstream the catalyst as a function of engine lambda (λ = 0.95-1.05) is shown in Figure 5.4. The formation of CO and THC is associated with the incomplete combustion of fuel inside the combustion chamber [83-84]. The limited amount of oxygen available in the cylinder at maximum rich mode (λ = 0.95), leads to incomplete combustion and subsequently the highest amounts of CO, THC and H_2 in the exhaust gas. As the engine condition changes from rich to lean, CO, HCs and H_2 concentrations gradually decrease due to the more complete combustion facilitated by the increase in oxygen concentration. On the other hand, the formation of NO emissions are associated with the increase of in-cylinder temperature and availability of oxygen inside the combustion chamber [84]. At λ<1 NO values are at their lowest as less oxygen is available to react with nitrogen. Since stoichiometric combustion results in the highest in-cylinder temperatures, NOx concentrations peak at lambda values relatively near to one, while at lean conditions (λ>1) incomplete combustion leads to cooler in-cylinder temperatures, hence NO emissions drop again [85].

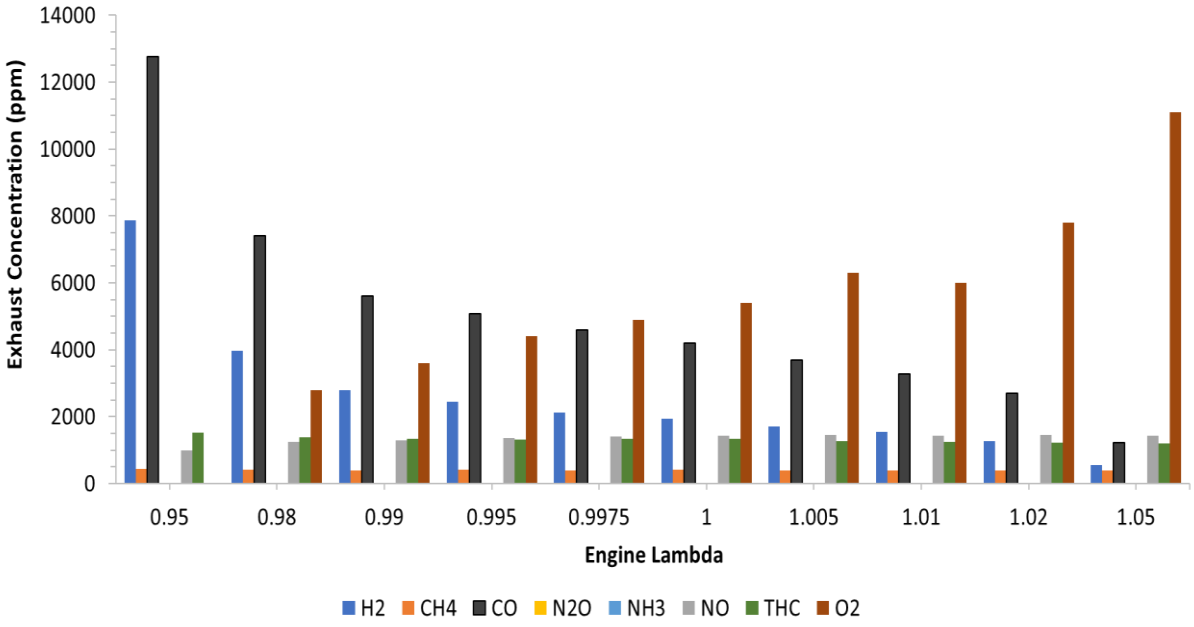


Figure 5.4: Exhaust concentration upstream the catalyst as a function of engine lambda for M40.

5.3.2. Catalyst Efficiency – Comparison of Different PGM Loaded Catalysts

The performance of two full-scale catalysts containing different PGM contents and ratios were investigated and analysed in this section. Catalyst A containing Pd:Rh and catalyst B containing Pt:Rh (with Pt loading price-equivalent to Pd).

Palladium and platinum behave very similarly and can be equally effective for the oxidation of HC's and CO [88]. The majority of natural gas aftertreatment system consists of Palladium/Rhodium catalysts as Pd is the most active noble metal known for methane abatement. On the other hand, Platinum behaves better under lean conditions so is generally used in diesel aftertreament system [89]. However, the price of Pd has surpassed that of Pt over the last decade and has more than doubled since, due to the higher demand. This has consequently driven research into the substitution of Pd by Pt in three way catalyst formulations to ease off the demand in Pd and bring about a balance between the two precious metals.

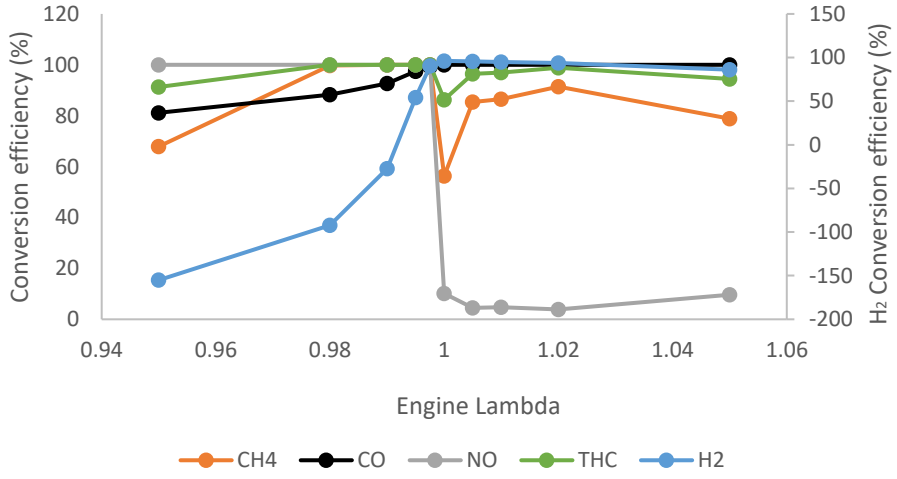


Figure 5.5: Pd-Rh Catalyst: Oxidation performance as a function of engine lambda.

The performance of the Pd-Rh CNG catalyst in oxidising the exhaust species as a function of lambda is illustrated in Figure 5.5. When the engine is running at rich mode ($\lambda<1$), the catalyst performance is very poor as it's unable to oxidise CO and HCs species. At this engine condition the catalyst lacks the required amount of O_2 to effectively oxidise all exhaust species. The poor CO conversion in turn favours NO reduction due to the less competition with O_2 over the catalyst, hence NO conversion remains high during this lambda range [90]. In addition, high amount of H_2 concentrations is produced in the catalyst

mainly due to CO undergoing water gas shift (WGS) reaction [91]. As engine lambda increases, the efficiency of the catalyst increases reaching 100% for all exhaust species just rich of stoichiometry (λ= 0.9975). At stoichiometric operation (λ = 1) NO conversion drops dramatically to 10% and continues to drop further as lambda increases which agrees with results from [88]. Similarly, HC conversion decreases at stoichiometry mainly due to its inability in oxidising CH_4 before increasing again lean of stoichiometry. Conversely, CO and H_2 conversion remains at 100% as lambda increases to max lean operation (λ = 1.05).

A gradual rise in CH_4 conversion can be seen between λ = 0.95 – 0.98, this is attributed to the availability of excess oxygen after other reducing agents such as CO and H_2 have been oxidised. Palladium is still in the metallic phase during this lambda window, and its surface is not completely coated by oxygen molecules. As soon as lambda reaches stoichiometry a sharp reduction in CH_4 oxidation is observed. Similar trends in Pd-Rh activity for methane abatement was observed by [9]. They attributed this to oxygen inhibition, i.e., adsorption of CH_4 is impeded because oxygen molecules cover the active sites [92, 93]. The different palladium oxidation states are responsible for the distinctive behaviour of CH_4 conversion on the lean side. As air/fuel ratio increases, the excess oxygen in the gas feed accelerates the oxidation of Pd to PdO, which when combined with Pd(0) is the most active palladium state for CH_4 oxidation under lean conditions as reported in the literature [88-92]. This can be seen in Figure 5.5, CH_4 conversion rate on the lean side (λ>1) rises to a maximum of roughly 90%, which corresponds to the existence of a mixed Pd/PdO phase, before reducing to around 78% when Pd is completely oxidised.

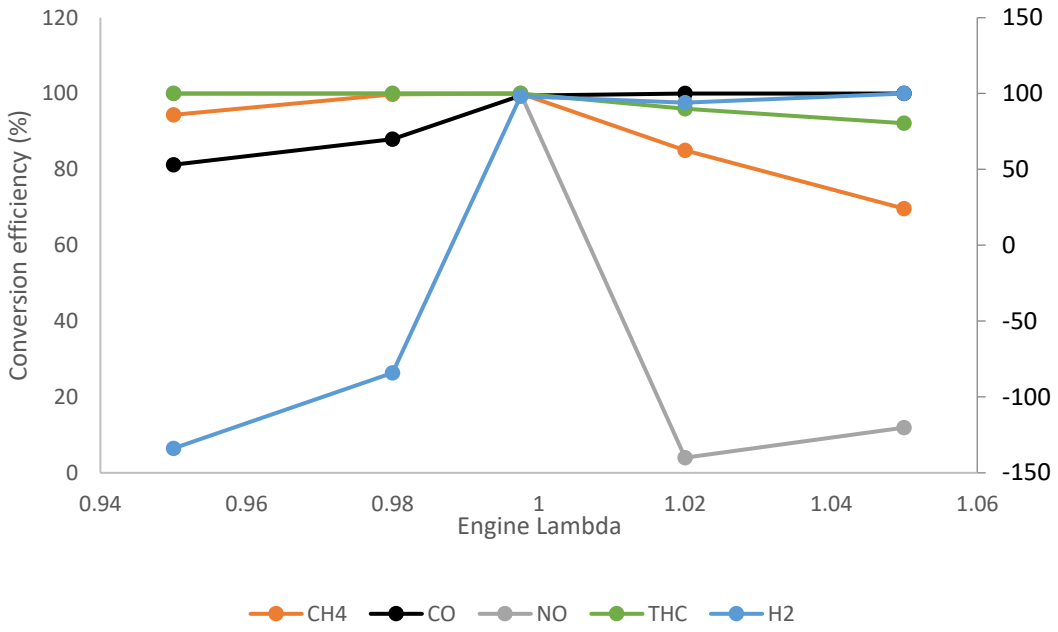


Figure 5.6 Pt-Rh Catalyst: Oxidation performance as a function of engine lambda.

Similarly, the performance of the Pt-Rh CNG catalyst in oxidising the exhaust species as a function of engine lambda is illustrated in Figure 5.6. The efficiency of the catalyst in removing CO and NO were very similar to the Pd/Rh catalyst and no clear differences can be observed. On the other hand, a slight dissimilarity in performance between the two catalysts is seen with regards to THC emissions, mainly in the extreme rich or lean region. On close inspection, this is largely due to CH_4 activity with the Pt catalyst outperforming the Pd catalyst significantly at max rich lambda (0.95), while the Pd catalyst had slightly better CH_4 conversion at max lean lambda (1.05). The lean CH_4 conversion profiles of the Pt/Rh catalyst are more linear compared to Pd/Rh as CH_4 conversion decreases steadily until λ = 1.05. Moreover, conversion of CH_4 is much higher just lean of stoichiometry and does not substantially drop as opposed to the Pd/Rh catalyst. Even though the Pt/Rh catalyst is also affected by oxygen inhibition, Pt remains in its active form near stoichiometric lean regions and hence is able to convert CH_4 more efficiently than the Pd/Rh catalyst [92]. These results suggest that Pt outperforms Pd in CH_4 conversion under rich conditions while Pd performed better under lean conditions. In addition, Rh plays a distinct and irreplaceable role among the three PGM metals by improving NOx conversion [88]. A combination of these three metals in the aftertreatment system may be able to combine strengths and mitigate their individual drawbacks in the aftertreatment of dual-fuel engines.

5.3.3. Effect of Air/Fuel Variation on Catalyst Performance

In this section the effect of systematically changing the air/fuel ratio on the performance of the two CNG catalyst is investigated and analysed. The study aims to understand the impact of various driving sequences that happen when accelerating (Stoic-Rich cycle), breaking (Stoic – Lean cycle) or a mix of driving conditions (Stoic – Lean – Rich) on the catalyst performance primarily using M40 fuel. Comparison with M0 will also be made to show the catalysts behaviour under different fuelling conditions. It should be noted that engine-out data has been acquired for only one case cycle to demonstrate the effect of changing engine condition on the emissions, and it can be used as a reference for the other cycles while taking into account the difference in lambda duration as appropriate.

5.3.3.1. Stoic to Lean

Figure **5.7** demonstrates how the engine-out emissions are affected by the change in lambda for the given cycle (Stoic 30s, Lean 30s) for the dual-fuel condition. As expected, changing the air/fuel ratio from stoic to lean reduces concentrations of CO, THC and H_2 due to the more complete combustion, while NO levels increase slightly due to the increase in in-cylinder temperature as explained in section 5.3.1.

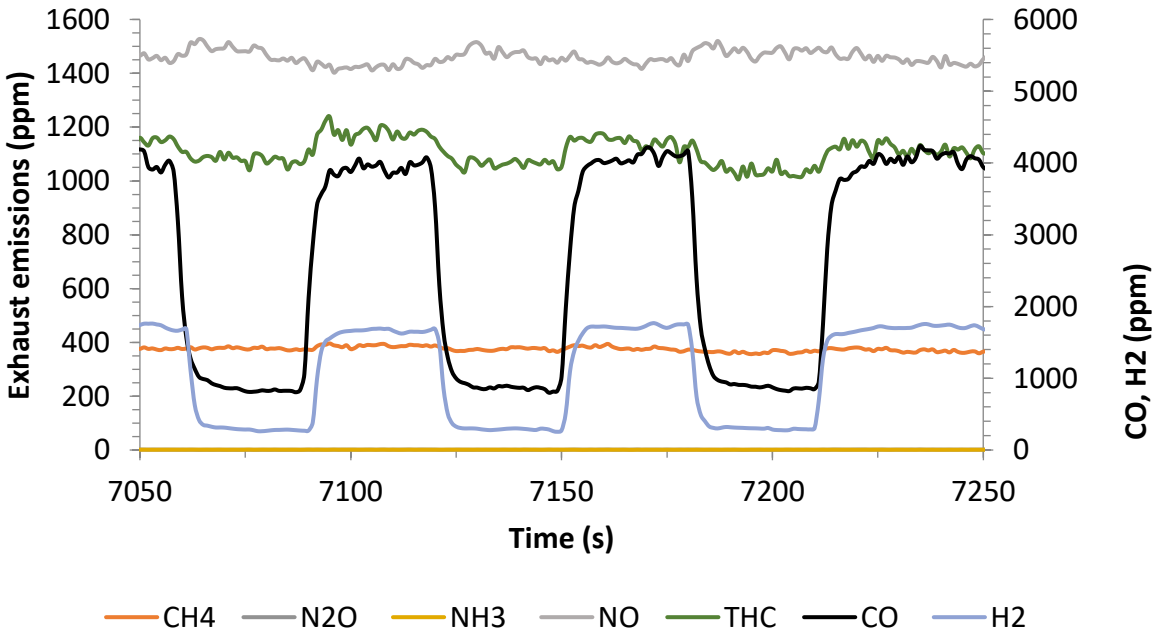


Figure 5.7: M40 engine-out emissions under Stoic to Lean lambda cycle.

The effect of the various Stoic to Lean cycles on the performance of catalyst A (Pd-Rh) for the M40 fuelling condition are shown in Figure **5.8**. As can be seen from the figures, CH_4 concentration measured after the catalyst gradually increases as the duration of lean in the cycle increases and the catalyst is unable to oxidise CH_4 even at excess oxygen concentrations. This is well in-line with results from the previous section (Figure 5.5) as the catalyst efficiency drops at this lean condition. In addition, the results show that the catalyst efficiency in reducing NO emissions is very sensitive to air/fuel ratio, NO peak levels gradually increase as the duration of lean increases. However, when the cycle changes back to stoichiometric condition, there is an obvious delay in NO conversion which slowly reduces to 0ppm. The slight distortion in NO profile is due to the presence of higher concentrations of methane with M40 fuelling. CH_4 acts as an inert gas, essentially meaning the exhaust stream is running slightly lean as less HC are able to undergo "reducing" reactions [92], hence why NO profile drags on before stabilising. This is also confirmed by examining the difference in NO profiles between M0 and M40 in Figure 5.9. There are insignificant levels of CH_4 present in the M0 fuelling and NO profile increases and decreases sharply with the cycle, hence no distortion is present in this case.

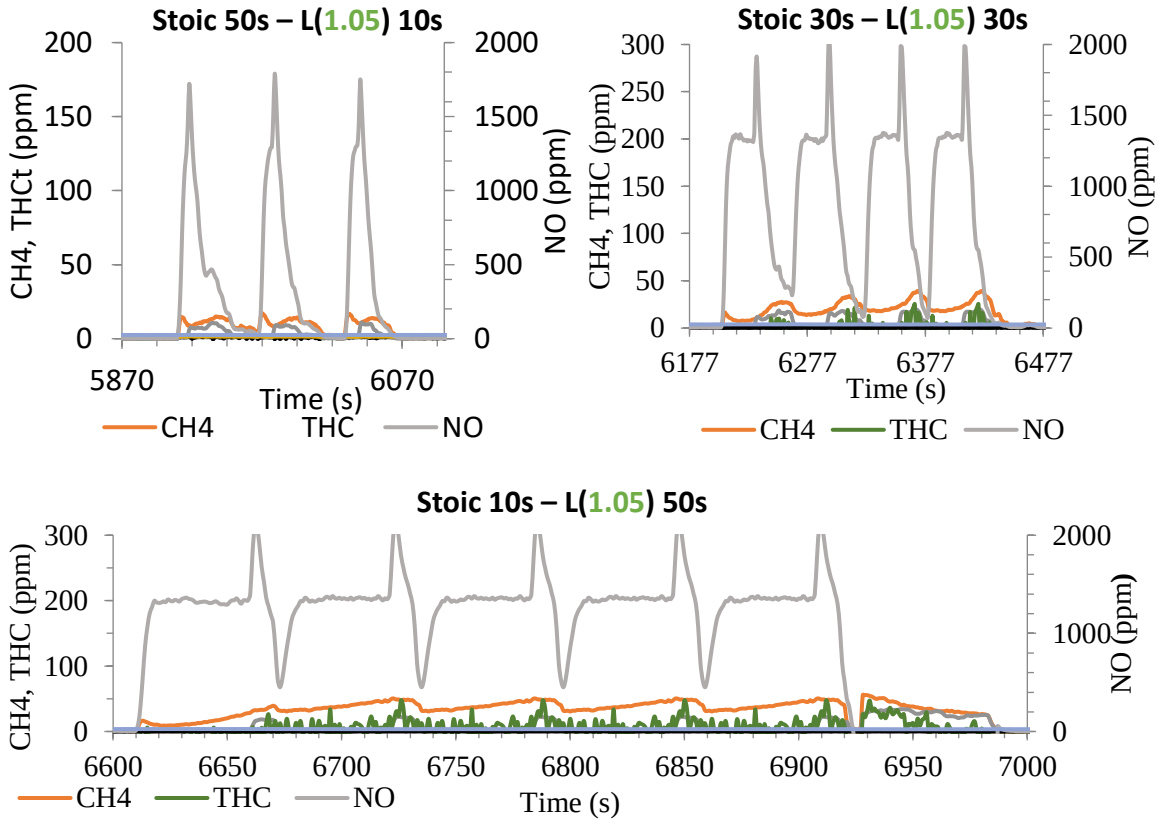


Figure 5.8: Effect of Stoic to Lean cycle on Cat A for M40

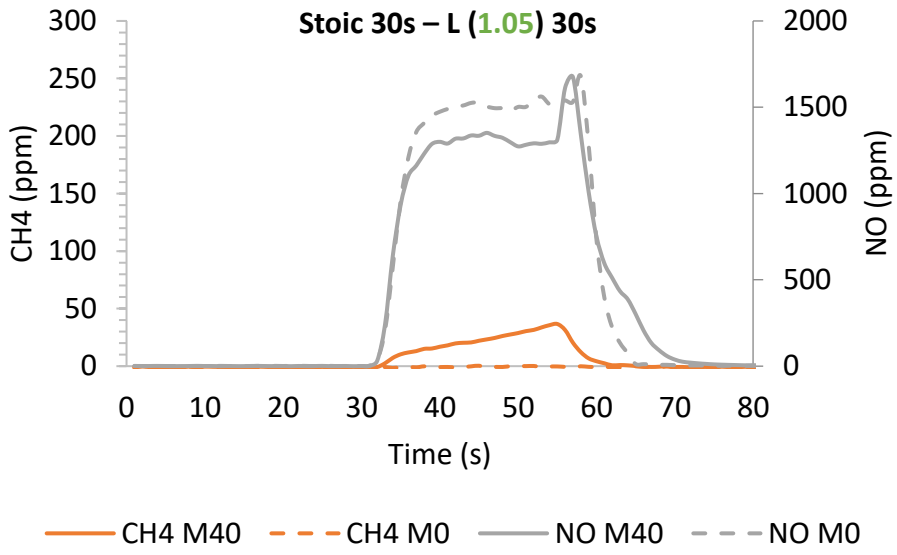


Figure 5.9: Comparison between M0 and M40 fuelling conditions for Cat B.

Figure **5.10** demonstrates the effect of the cycle on catalyst B (Pt-Rh). The catalyst struggled even more with oxidising rising methane emissions as compared to catalyst A, with CH_4 levels peaking at 100 ppm at the longest lean duration. This further supports findings in section 5.3.2 as the Pt-Rh catalyst performed worse in CH_4 abatement at lean conditions. No significant differences is seen for NO emissions as it performs similarly to catalyst A. This is due to the fact that both catalysts contain similar content of Rh which is the main PGM responsible for NO abatement in three-way catalysts [88].

In both cases, the catalysts were not affected by the cycles and they were both able to restore full performance as soon as the cycles concluded. However, further tests with longer and more vigurous cycles should be undertaken in order to properly assess the long-term impact of such cycles on the catalyst performance. The tests carried out were not intended for such study and is outside of the scope of the thesis and so the results obtained should only be taken as a guide.

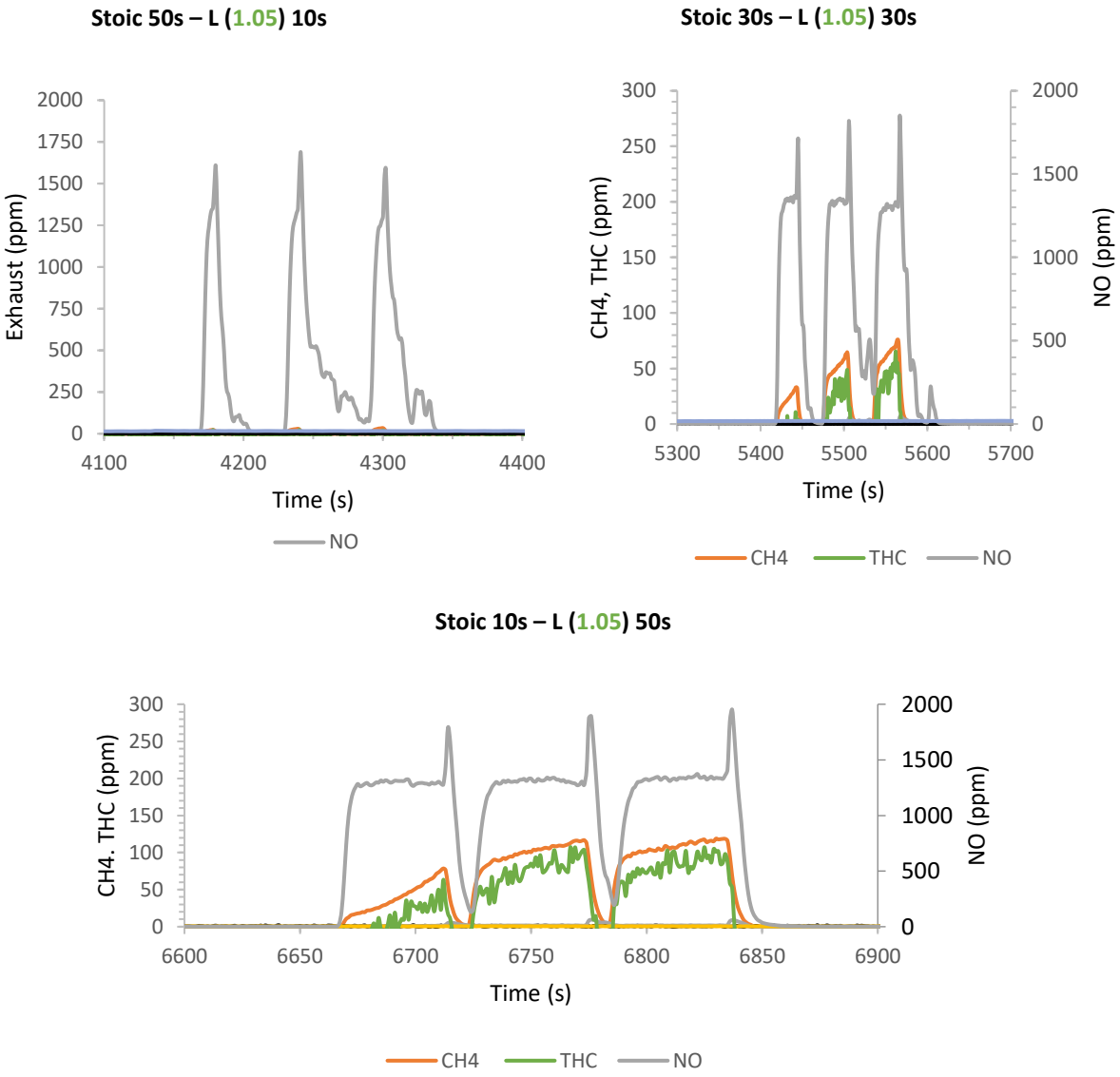


Figure 5.10: Effect of Stoic to Lean cycle on Cat B for M40.

5.3.3.2. Stoic to Rich

Figure **5.11** demonstrates how the engine-out emissions are affected by the change in lambda for the given cycle (Stoic 30s, Rich 30s) for the dual-fuel condition. As expected, changing the air/fuel ratio from stoic to rich increases concentrations of CO, THC and H_2 due to the lower levels of oxygen available for complete combustion, while NO levels reduce due to the lower in-cylinder temperatures as discussed previously in section 5.3.1.

The effect of the various Stoic to Rich cycles on the performance of catalyst A (Pd-Rh) for the M40 fuelling condition are shown in Figure 5.12. As can be seen from the figures, considerably high levels of ammonia (approx. 1000 ppm) are being produced over the catalyst at rich conditions. This is attributed to the high level of H_2 available over the catalyst at this rich condition (approx. 8000 ppm engine-out, from Figure **5.11**) which then reacts with NO producing NH_3 [76-79]. Moreover, a significant amount of CO also escaped the catalyst which is mainly due to poor combustion during the rich period and the lower amount of NO available to undergo reducing reactions due to its more favourable reaction with H_2 [89]. Some CH_4 slippage is also noticeable downstream the catalyst especially for cycles with longer rich durations. The reduced efficiency of the catalyst at this rich condition is in line with results from previous section 5.3.2. This further highlights the importance of developing a strategy aimed to reduce exhaust slippage at such engine condition.

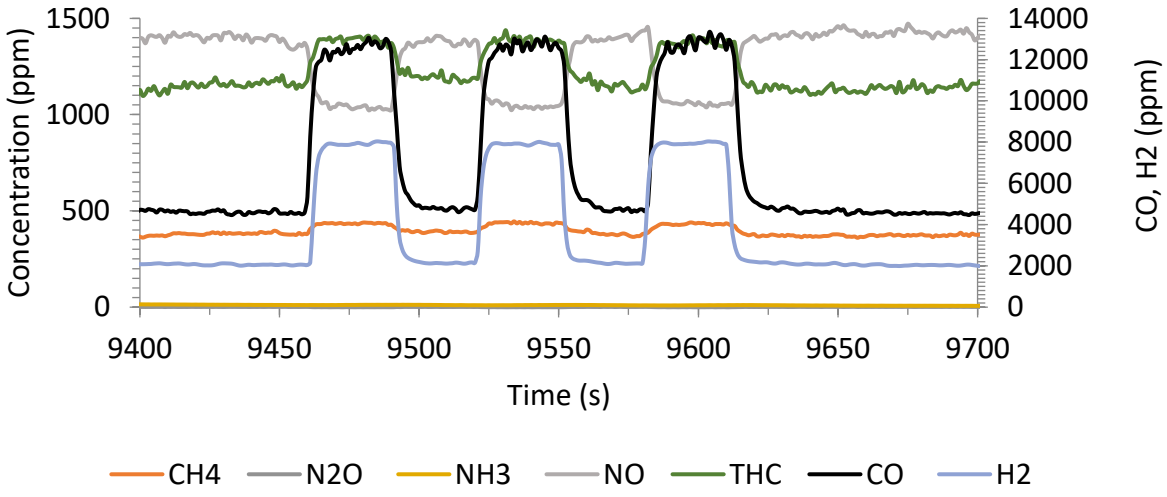


Figure 5.11: M40 engine-out emissions under Stoic to Rich lambda cycle.

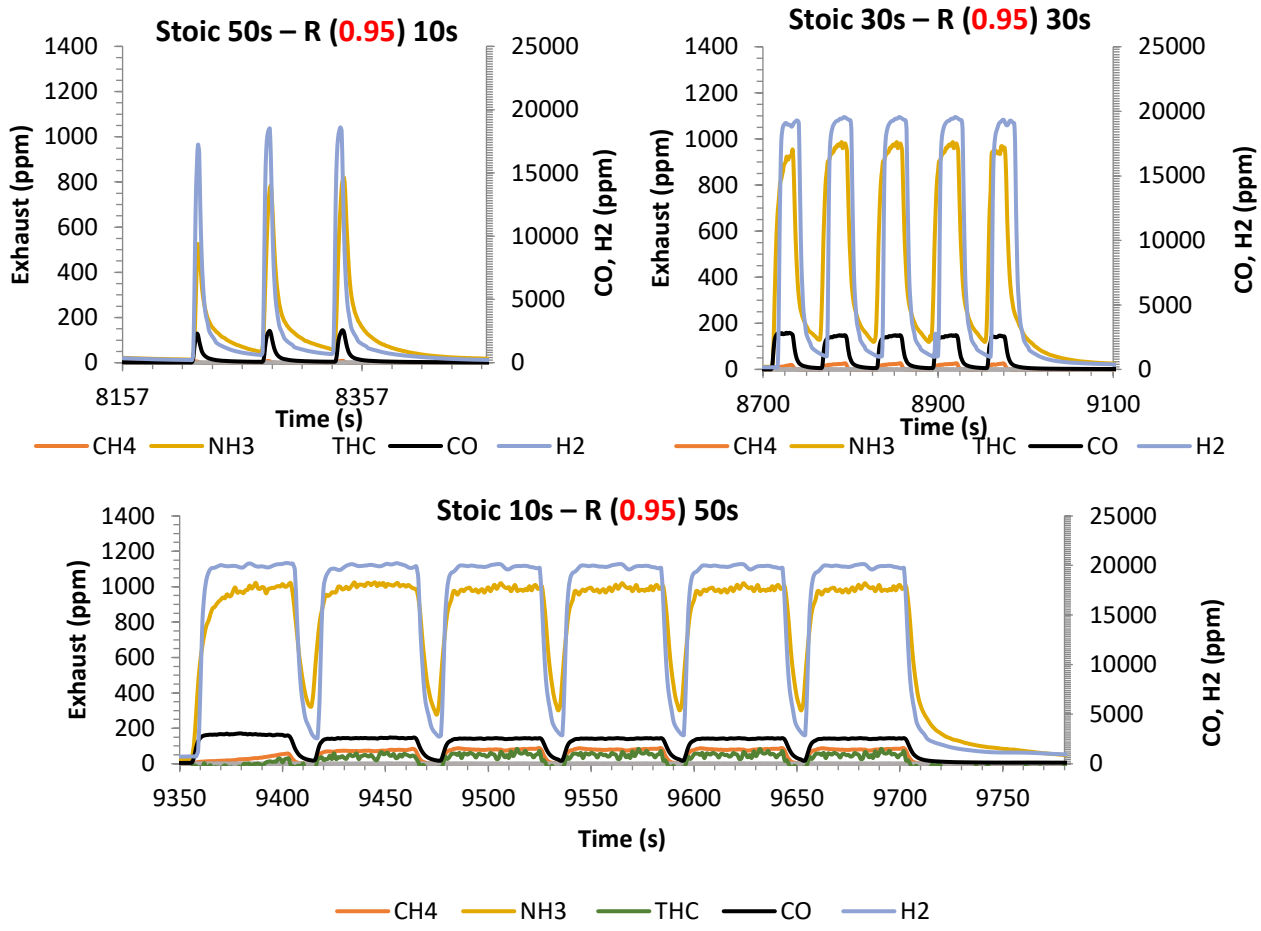


Figure 5.12: Effect of Stoic to Rich cycle on Cat A for M40.

Figure 5.13 demonstrates the effect of the different cycles on Cat B (Pd-Rh) for M40 fuel. The trend of results closely imitates that for Cat A. However, the Pt catalyst is slightly more efficient as lower NH_3, CO and CH_4 were detected downstream the catalyst. These results agree with the comparisons made in Figure 5.5 and Figure 5.6 in the previous section. In both cases, the catalysts were not affected by the cycles and they were both able to restore maximum performance as soon as the cycles were concluded. Examining the difference between the two fuelling conditions in Figure 5.14, methane substitution showed lower levels of NH_3 and CO downstream the catalyst. This difference however should be attributed to the lower exhaust levels resulted from the M40 combustion compared to M0 (Figure **4.4**), and thus not considered a fuel effect over the catalyst.

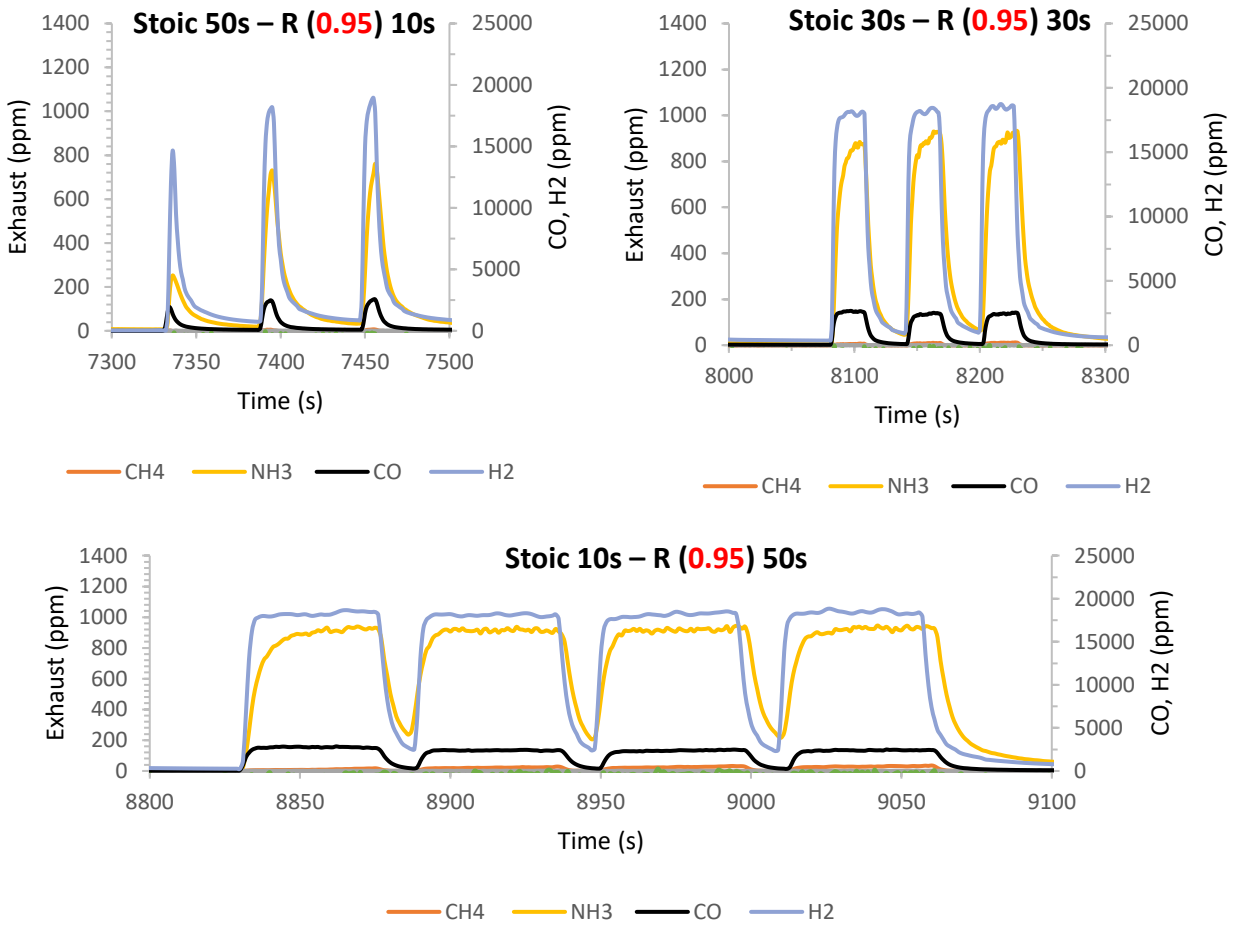


Figure 5.13: Effect of Stoic to Rich cycle on Cat B for M40.

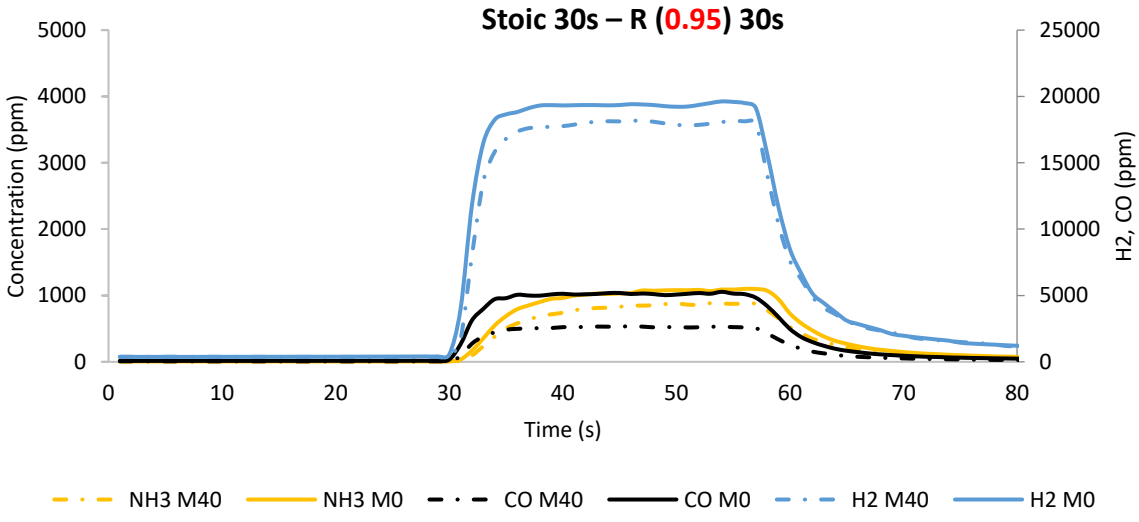


Figure 5.14: Comparison between M0 and M40 fuelling conditions for Cat B.

5.3.4. Effect of Cyclic Lambda Variation on Emissions and Fuel Economy

The results from the previous section focused on the effect of the cycle on the performance of the catalyst alone. It is evident that however these cycles will have an effect on engine efficiency and fuel economy. Running a lean cycle (from stoic to lean and vice versa) will improve the engine efficiency as less fuel is used in the combustion process. However, this subsequently might lead to high tailpipe NOx emissions that could be above the limit set by regulations especially the more stringent Euro 7. This encouraged to investigate combination of cycles aiming to reduce tailpipe emissions and improve fuel economy simultaneously. To achieve this, cycles with different stoichiometry, lean and rich ratios were evaluated and studied. Other parameters that were evaluated include the amplitude and duration of each cycle. An extensive number of cycles were tested for this purpose, however only a chosen set of tests will be presented in this chapter. Catalyst A and M40 fuel are used for the analysis in this section unless otherwise stated. Table 5.2 highlights the cycle tests carried out and the subsequent fuel efficiency results.

Table 5.2: Cycle tests showing ratio of stoic, lean and rich used and fuel efficiency for each case**.**

Engine-condition: 30Nm/2100 rpm **Fuel condition: M40**			
Cycle duration	**No.**	**Cycle**	**Improvement fuel efficiency (%)**
60s	1	40s stoic / 18s lean (1.01λ) / 2s rich (0.98λ)	0.97
	2	40s stoic / 15s lean (1.01λ) / 5s rich (0.98λ)	0.32
	3	40s stoic / 15s lean (1.02λ) / 5s rich (0.98λ)	1.39
	4	40s stoic / 5s rich (0.98λ) / 15s lean (1.02λ)	1.39
	5	35s stoic / 5s rich (0. 98λ) / 6s stoic / 9s lean (1.05)	1.02

The primary aim of the tests was to improve the fuel economy by running the engine lean either for a longer period or at a higher amplitude. At the same time, a rich cycle is introduced either before or after the lean cycle to help flush the catalyst from the excess oxygen and restore stoichiometry for the catalyst. Catalysts for automobiles are designed to operate in a narrow range of stoichiometric operating conditions. During normal vehicle operation, engine lambda changes from lean to rich, which reduces the efficiency of the catalyst. For this reason, catalysts are equipped with OSC materials that temporarily enable the catalyst to store oxygen under oxidizing conditions (Equation 5.1, Equation 5.2) and release the oxygen for CO and HC oxidation under reducing conditions (Equation 5.3, Equation 5.4). The OSC ability of the catalyst is due to cerium oxide (CeO_2) in the washcoat. [From 99-101].

$$2CeO_2 \leftrightarrow Ce_2O_3 + 0.5O_2 \qquad \text{Equation 5.2}$$

$$Ce_2O_3 + NO = 2CeO_2 + 0.5N_2 \qquad \text{Equation 5.3}$$

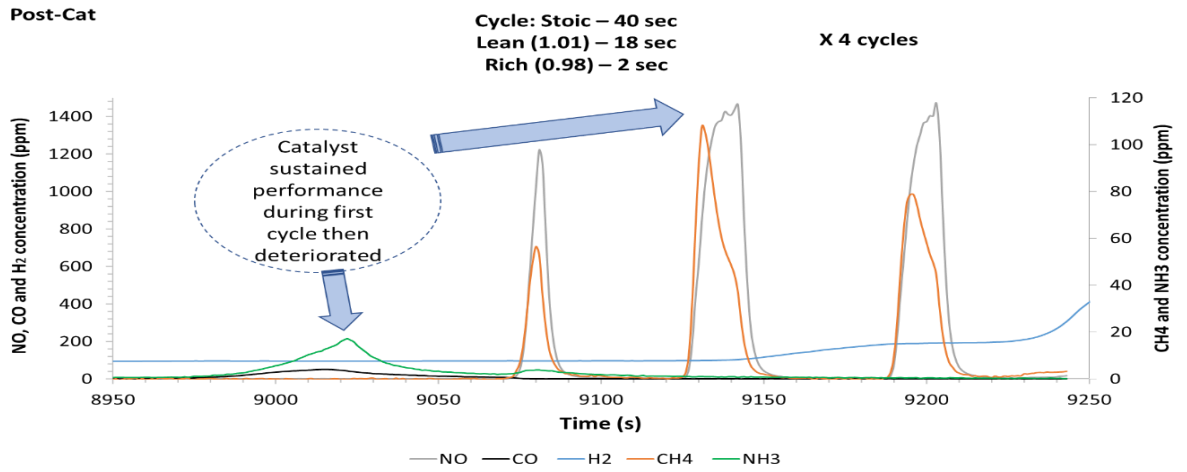
$$2CeO_2 + CO = Ce_2O_3 + CO_2 \qquad \text{Equation 5.4}$$

$$CeO_2 + HC = Ce_2O_3 + CO_2 + H_2O \qquad \text{Equation 5.5}$$

Figure **5.15** show an example of the test conditions for cycles 1 and 2 and their effect on exhaust emissions post-catalyst. Inspecting the effect of cycle 1 from Figure **5.15**a, the catalyst was able to cope well at the start of the cycle with only a minimal peak of NH_3 slippage (~20 ppm) showing that the combination of OSC of the catalyst and also the introduction of a short rich duration was able to deal with the excess oxygen produced and maintain the catalyst at close to stoichiometric condition. Trovarelli [100] reported that during the rich phase, CO adsorption on ceria creates oxygen vacancy sites. NO produced during the lean phase can be reduced by decomposition on these vacancy sites or by reduction with the adsorbed CO to form N_2. They also reported that NH_3 is formed due to reaction of NO with H intermediates which explains the NH_3 peak seen initially. However, as the cycle continued the catalyst performance deteriorated with relatively high tailpipe NO peaks. This is attributed to the increase in O_2 concentration due to the longer lean period in the cycle resulting in the oxidation of ceria and reduction in the number of surface oxygen vacancy sites available for NO decomposition. In

addition, CO is completely oxidised due to the excess oxygen and is hence unavailable for NO reduction over the catalyst.

a)



b)

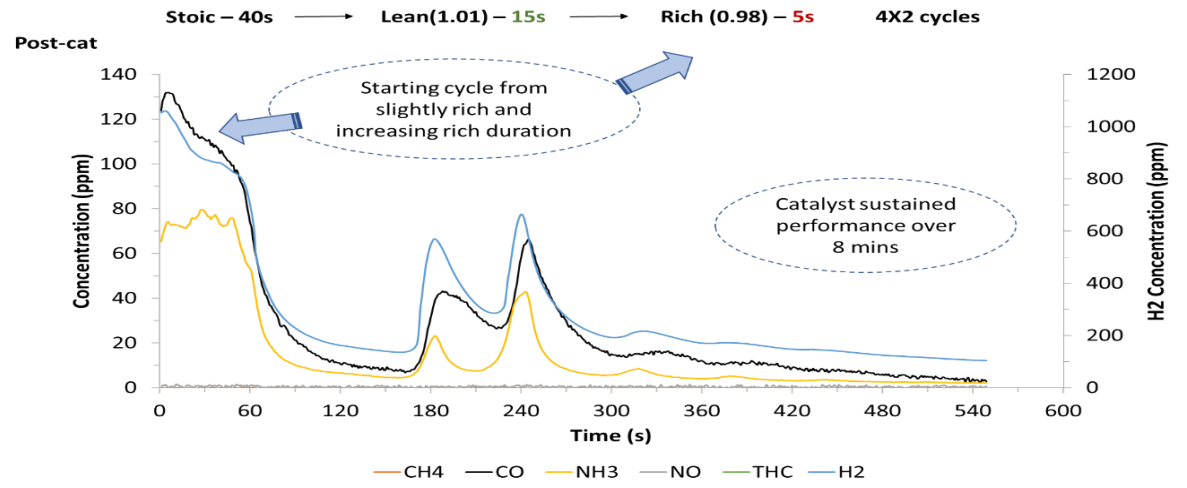


Figure 5.15: Effect of test cycles on catalyst-A performance; a) Cycle 1, b) Cycle 2.

To improve the NO efficiency of the catalyst, the ratio of rich : lean in the cycle was increased as shown in Figure **5.15** (cycle 2). In this case, the cycle started from slightly rich as evident from the increased level of CO, H_2 and NH_3 at the start of the cycle. This along with the increased duration of rich period had a positive effect on the catalyst performance as more CO was available to reduce the NO concentrations resulted from lean period. In addition, the longer rich feed enables sufficient time for the regeneration of oxygen vacancy sites for NO decomposition [100]. The catalyst was able to sustain a good performance over 8 minutes with only small peaks of CO and NH_3 visible during this period. The increase in rich period however reduced the benefits in terms of fuel economy compared to cycle 1 with only 0.32% achieved during this cycle (Table 5.2).

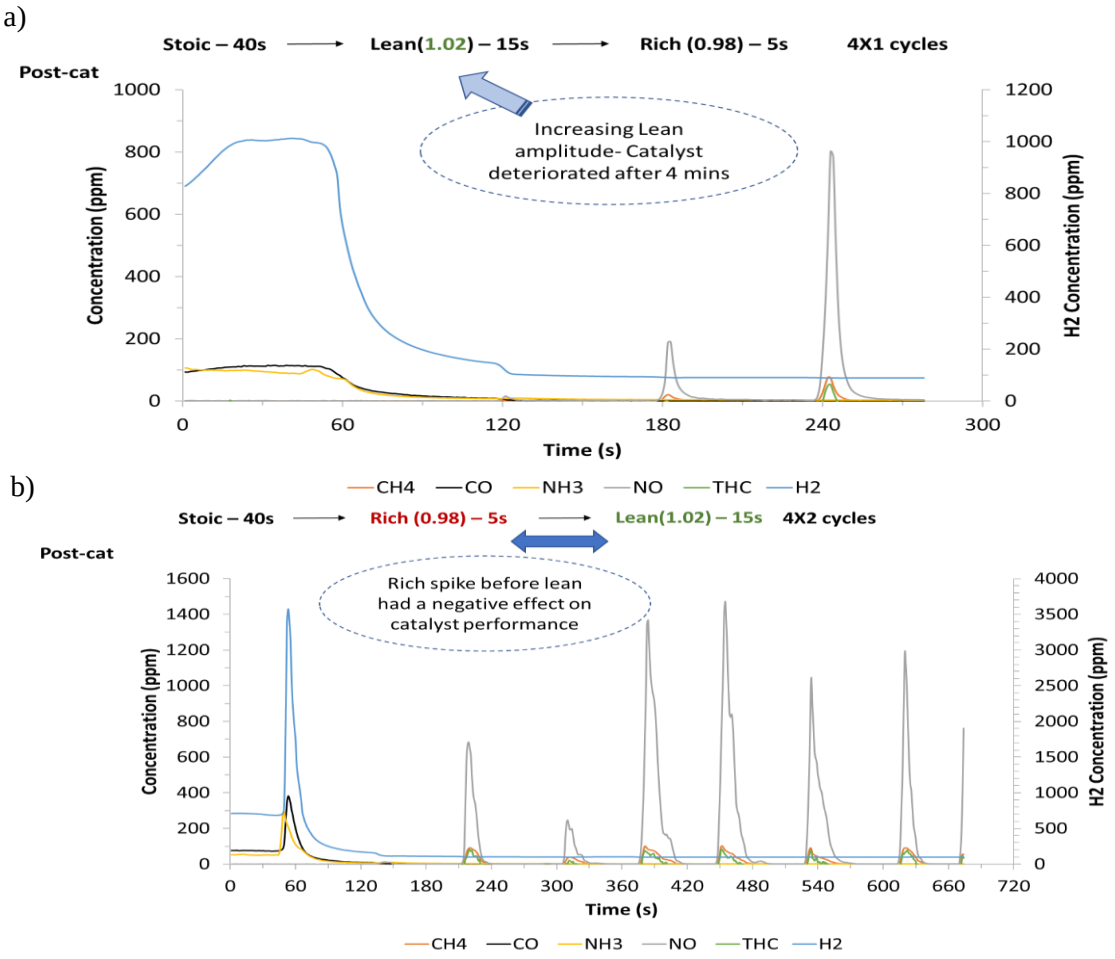


Figure 5.16: Effect of test cycles on catalyst-A performance; a) Cycle 3, b) Cycle 4.

Figure **5.16**a illustrates the effect of increasing the lean amplitude while keeping the same lean/rich durations as that of cycle 2. Increasing lambda to 1.02 showed a positive effect on fuel economy savings of 1.39% and the catalyst performed well for the first few cycles initially reducing all exhaust species. The catalyst performed significantly better in this cycle compared to cycle 1 (Figure **5.15**) and was able to keep NO emissions at a lower level, even though the lean amplitude was higher. This further highlights the importance of prolonging the rich period to enable the sufficient regeneration of oxygen vacancy sites thus reducing NO levels during the lean period. However, as the cycle continued further, the catalyst performance deteriorated after 4 mins. Figure **5.16**b shows the effect of starting the rich period before the lean period in the cycle. High amounts of CO and NH_3 can be seen at the start of the cycle as the rich period has a more dominant effect on the catalyst performance initially before the lean period starts to dominate at later cycles with NO and CH_4 slippage observed.

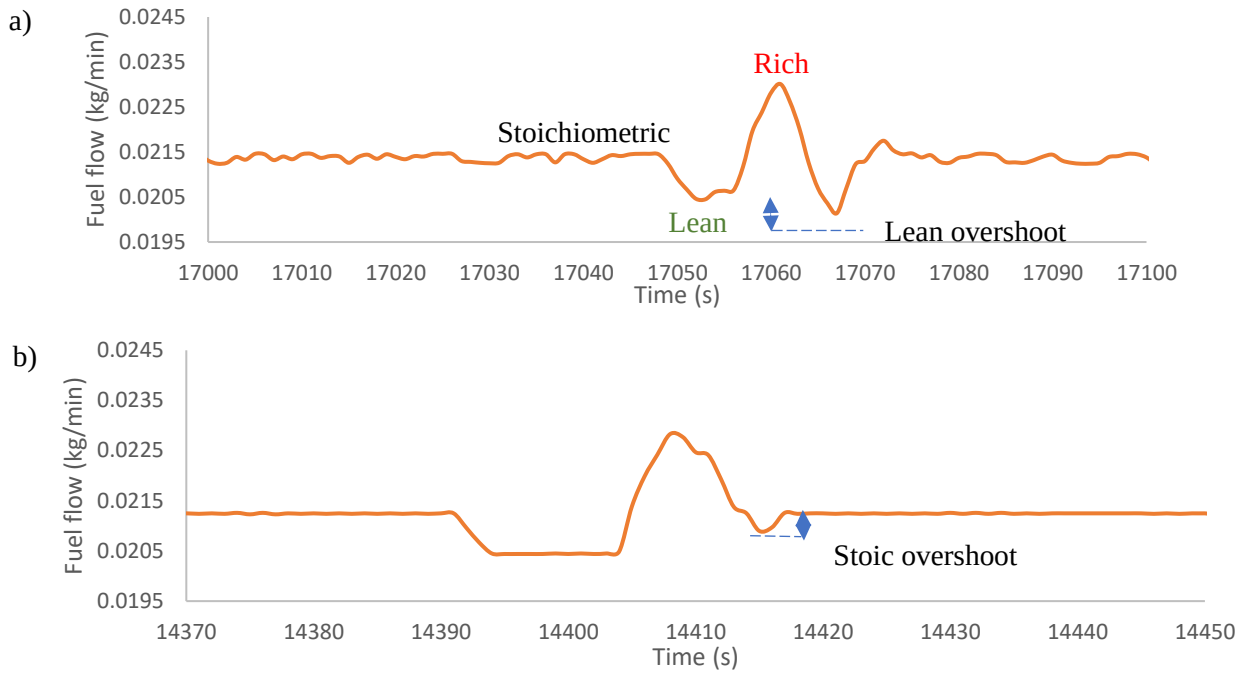


Figure 5.17: Fuel flow profile highlighting the effect of switching between different lambda states.

Further analysis was conducted to investigate the reasons for the increase in NOx emissions at later stages in the cycle. Figure **5.17**a shows the fuel profile of one of the preliminary cycles conducted during these tests. It can be clearly seen that when the cycle changes from rich to lean, there is a slight fuel overshoot compared to the change from stoic to lean. This overshoot increases the amount of oxygen going into the catalyst and over time results in NOx slippage. By contrast, Figure **5.17**b shows the effect on the fuel profile when the cycle changes from lean to rich to stoic. In this case, an overshoot into the lean section still occurs but the amplitude is low enough for the catalyst to cope with the excess oxygen. Therefore, it can be concluded that an intermediary stoic period is necessary to prevent NOx overshoot at later stages in the cycle. The cycles were then further developed taking into account the results from the preliminary studies and presented in Figure **5.3** (Cycle 2A). The cycle parameters were chosen as they gave an overall improvement in fuel economy while also keeping exhaust emissions to a minimum and can therefore act as a guidance to further improve these cycles. The effect of the cycle on the engine-out emissions and catalyst performance are presented in Figure 5.18. The cycle was allowed to run for 15 minutes to analyse the performance of the catalyst and whether it can sustain this performance over a long period of time. An intermediary stoichiometric period of 6 seconds was added in the cycle between rich and lean period and the effect can be seen from the slight change in gradient of engine-out NO emissions.

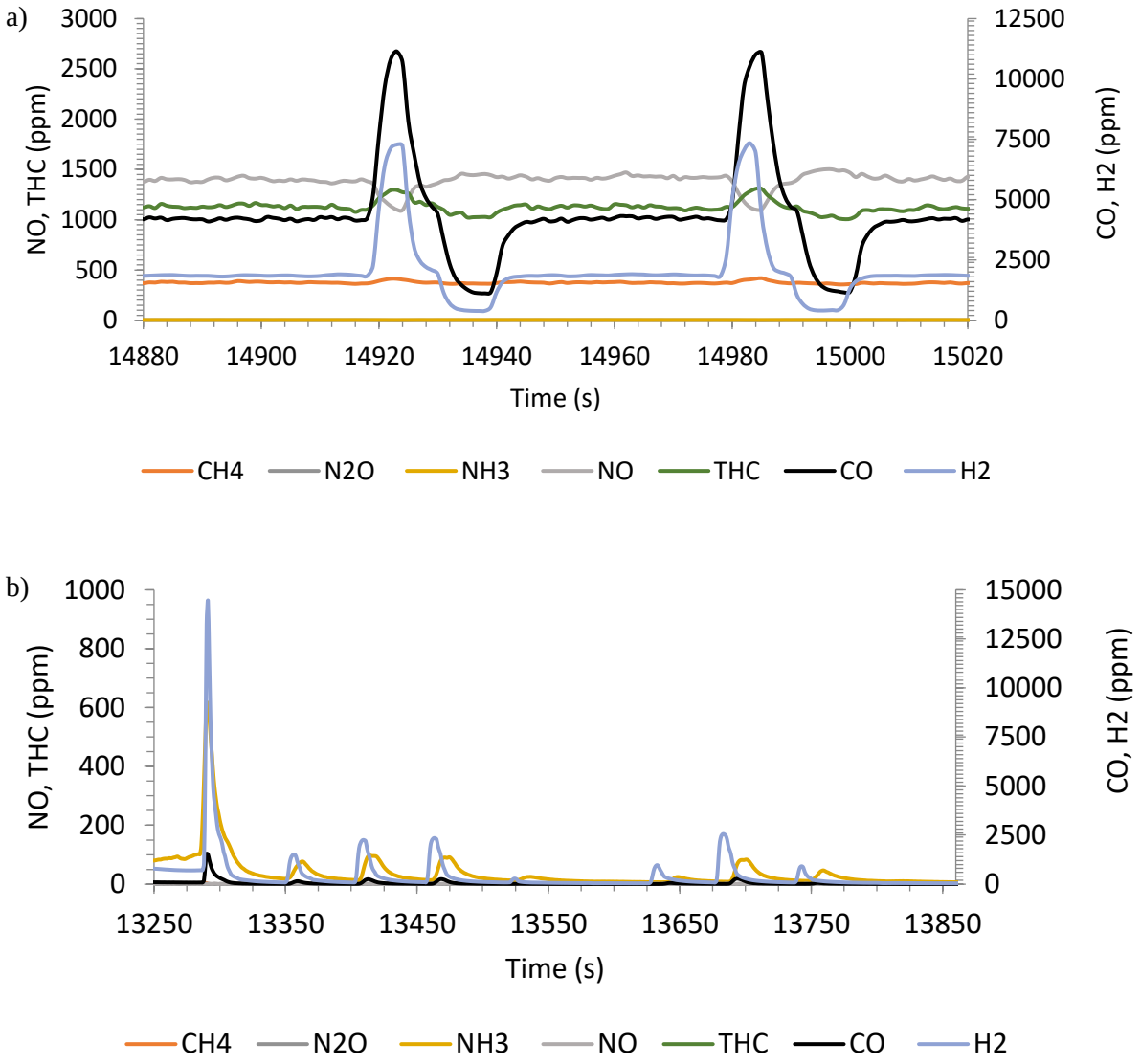


Figure 5.18: a) Engine-out emissions, b) Effect of cycle 5 on post-catalyst-A emissions.

Inspecting Figure 5.18b, a small peak of CO and NH_3 are visible during the initial stage post-catalyst, due to the rich period at the start of the cycle along with approximately 15,000 ppm of H_2. However, the catalyst was able to abate all the exhaust emissions thereafter with no traces of NO or CH_4 throughout the entirety of the cycle, in contrast with cycle 4 (Figure **5.16**b). In addition, cycle 5 achieved a positive fuel economy of 1.02% as presented in Table 5.2. Small traces of CO (<300 ppm) and NH_3 (<100 ppm) were visible across the cycle mainly during the rich phase, which suggests that better tuning of the cycle is possible to further enhance the fuel economy. This result encouraged further investigation to assess the efficiency of such cycle with the Pt/Rh catalyst (Catalyst B) and also using gasoline only (M0 fuel). The results are demonstrated in Figure **5.19**. As can be seen from the figure below, the Pt/Rh

catalyst was also able to achieve comparable results during the cycle using the M40 fuelling, with no tailpipe NO emissions observed (Figure **5.19**a). Again, an average of 5000 ppm of H_2 was detected downstream the catalyst along with some negligible traces of CO and NH_3. As explained in section 4.3.3.4, the presence of high concentrations of CH_4 with the M40 fuelling increases the formation of H_2 through steam reforming reactions [Eq. 4.6] and subsequently results in the formation of NH_3. The fuel effect over the catalyst is also demonstrated by comparing it against the M0 fuelling condition (Figure 5.19b) where no H_2 or NH_3 levels were seen across the cycle.

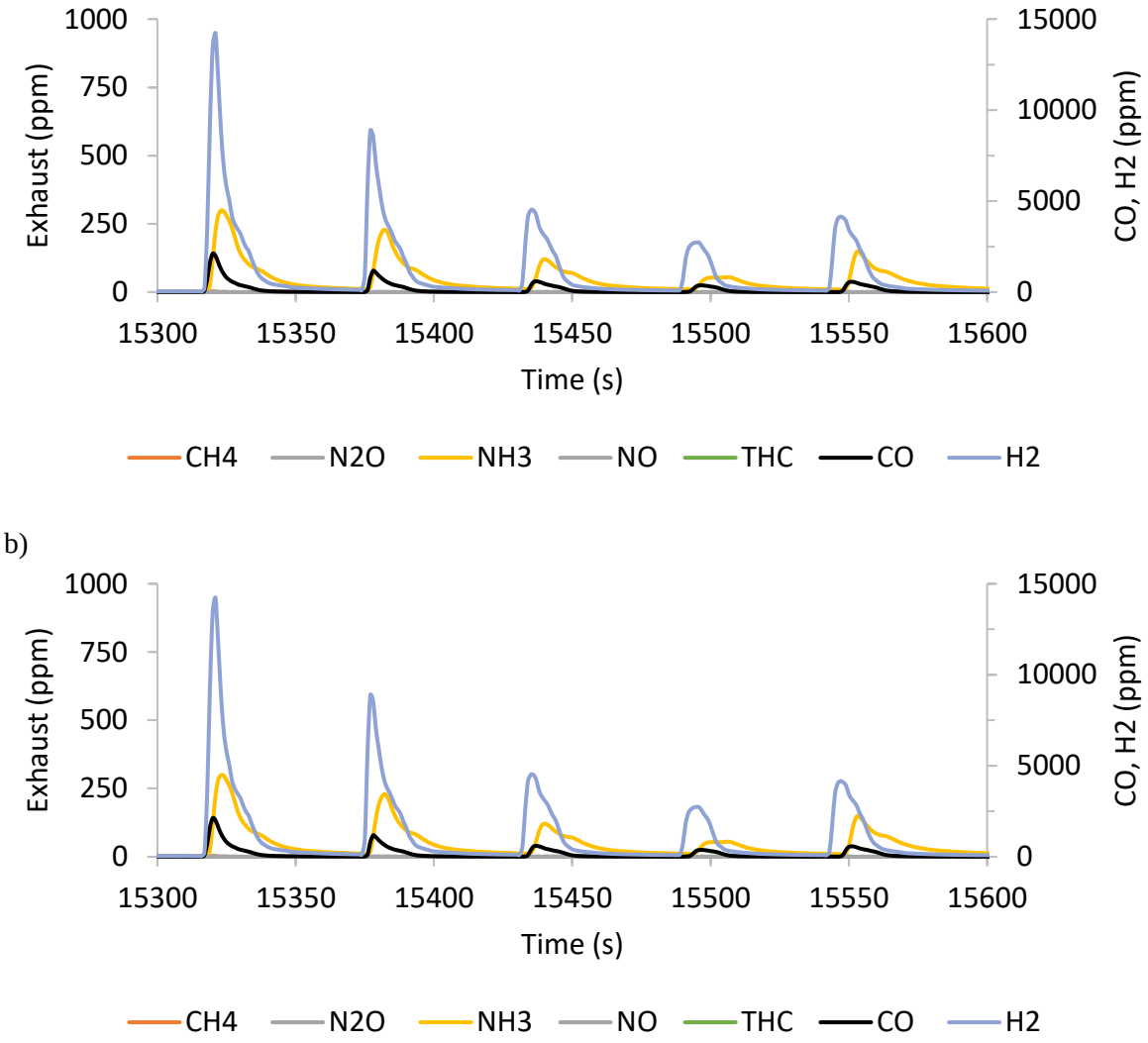


Figure 5.19: Effect of cycle on post-catalyst-B emissions using a) M40 fuelling, b) M0 fuelling.

5.4. Summary

The performance of two full-scale CNG catalysts with different PGM loadings under various engine lambda conditions and cyclic air/fuel ratio was evaluated and compared. Generally, the results demonstrated that the two catalysts perform very similarly and both Pd and Pt were very effective at oxidising harmful exhaust species at stoichiometric engine conditions. However, at engine rich conditions the efficiency of the Pd catalyst in oxidising CH4 significantly drops while the Pt catalyst showed considerably better performance. On the other hand, Pd catalyst slightly outperformed Pt at engine lean conditions. This highlights the need to have both PGMs for a more efficient aftertreatment system for CNG engines across various lambda settings. Moreover, both catalysts demonstrated good recovery of performance after a series of rich or lean cycles while the tailpipe emissions emitted were analysed and identified. More CH4 slippage was seen for the M40 condition compared to M0 during the lean cycles with the Pd/Rh catalyst showing better efficiency in this regard.

In addition, cycles have been developed with the aim to offset or even reduce the fuel penalty incurred under real-life driving conditions once the pedal is suddenly pressed and the car accelerates, while reducing tailpipe emissions simultaneously. From the preliminary studies it was found that it's beneficial to run the engine at lean for longer duration to offset fuel consumption after a sudden rich spike. The combination of the OSC of the catalyst and also the introduction of a short rich duration was able to deal with the excess oxygen produced and maintain the catalyst at close to stoichiometric condition. However, it is necessary to have an intermediary stoichiometric point between the rich and lean periods to prevent NOx overshoot later on in the cycle. It is suggested that the cycles can be further enhanced by increasing the OSC of the catalyst and extending the lean period in the cycle thus achieving even better fuel economy.

6. Impact of Dual-Fuel Methane-Gasoline Combustion on PM Emissions

6.1. Introduction

There are several studies in the literature that has characterised PM emissions in GDI engines. In contrast, there are limited studies reporting the effect of natural gas-gasoline dual-fuelling on PM mass and number in GDI engines [109, 134], while the effect on PM reactivity, nanostructure and morphology is unexplored. The aim of this paper is to obtain an improved understanding of the combined synergy effect of dual methane (the main constituent of natural gas) -gasoline fuel injection on gaseous and particulate matter emissions in GDI engines. Soot samples collected from neat gasoline (M0), 20% methane (M20) and 40% methane (M40), energy-based substitution, are analysed and compared to understand the effect of methane addition on the PM oxidative reactivity and its impact on the different morphological and nanostructure parameters. To the authors knowledge, this is the first comprehensive study on PM characterisation of methane dual-fuel in GDI engines.

6.2. Experimental Procedure

The engine was operated at idle conditions for 30 minutes to bring the oil and coolant temperatures to operational levels of 90 ± 1 ^{o}C and 95 ± 2 ^{o}C respectively, to avoid cold start effects and minimize emission fluctuation. The experiments were run in a static state with a fixed speed of 2100 ± 2 rpm and a load of 90 ± 1 Nm, which corresponded to a medium load condition from the Worldwide harmonized Light vehicles Test Cycles (WLTC) for vehicles. The experimental apparatus used in this section is demonstrated in Figure **6.1**.

The level of gasoline substitution by methane was evaluated under three different conditions: 0% (M0), 20% (M20), and 40% (M40) replacement. M40, was chosen as a compromise between avoiding start-up problems and lower engine performance associated with methane fuelling while still containing a substantial amount of methane to reap the particle reduction benefits of the fuel. Methane gas was port-injected into the engine cylinder and the spark timing was adjusted in order to phase the Mass Fuel Burn 50% (MFB50%) of the dual-fuel to that of the baseline gasoline. This was done in order to observe how the addition of methane influenced gaseous and particle emissions independently. The temperature

and flow rate of methane gas were monitored throughout the experiment to ensure there was no significant variations in density. Microfibre glass filters were used to collect soot samples directly from the engine exhaust by the means of a pump with a flowrate of 10 l/min over a period of 45 minutes. Prior to loading, the filters were baked in the oven for six hours at 500^{o}C to prevent moisture absorption. The loaded filters for pure gasoline and the two dual-fuel conditions are shown in Figure **6.2**. In addition, TEM investigation was carried out by exposing 3.05 mm TAAB Formvar coated grids to the engine exhaust stream for 10 seconds. A minimum of 3 samples were taken for each fuelling condition to ensure that the PM was properly captured by the grids.

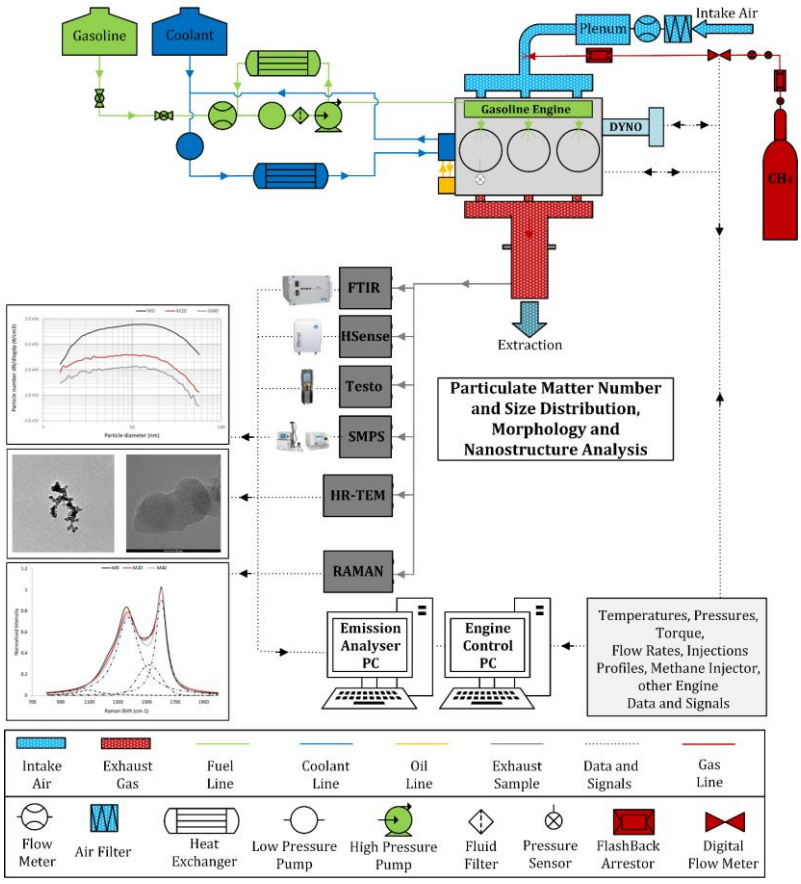


Figure 6.1: Experimental apparatus.

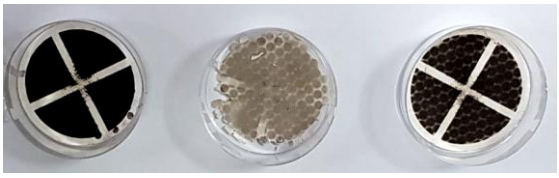


Figure 6.2: Loaded soot filters for M0, M40 and M20 respectively.

6.3. Results and Discussion

6.3.1. Engine Combustion and Gaseous Emissions

As in the previous experiments, MFB50 % was maintained at the same level allowing for unbiased comparisons of the engine-out emissions of the various fuelling compositions. Table 6.1 shows several data resulted from the combustion of the gasoline and dual-fuel mode. Exhaust gas emissions data for gasoline and dual fuel (M20 and M40) are shown in Figure **6.3**. The given data are the averages of over 200 sample runs, with error bars indicating a standard variation of one standard deviation from the mean value. The CO reduction of 21% and 42% for M20 and M40, respectively, from the plain gasoline baseline, is the most significant variation in gaseous emission composition across the fuelling techniques. CO_2 emissions were also drastically lowered, with M20 emitting 5% less CO_2 and M40 emitting 10% less CO_2.

NOx and THC emissions seem to be unaffected by the switch to M20 in terms of gaseous emissions. A significant rise in NOx emissions was seen at the highest level of methane fuelling, M40, with a net increase of 9 percent. By comparison to the plain gasoline baseline, M40 fuelling resulted in an 18 percent decrease in total hydrocarbons. In contrast, one significant shift was the apparent rise in methane (CH_4) emissions with increased CH_4 replacement, which may be explained mostly to non-combusted methane fuel exiting the combustion chamber. CH_4's total global warming potential is 25 times larger than that of CO_2 despite the fact that it accounts for a negligible fraction of exhaust emissions. The gaseous form of methane fuel explains the decrease in CO, CO_2 and unburned non-methane hydrocarbon emissions [111]. Compared to direct-injected gasoline, gas enters the cylinder as a gas, improving the forming quality and homogeneity of the mixture. As a consequence, the amount of unburned fuel that may contribute to these gaseous emissions generating processes is reduced. Another advantage of using methane over gasoline is that its atomic H/C ratio is four times larger than gasoline's which means that methane reduces CO2, and HC emissions as a result of its lower carbon content. Methane's higher adiabatic flame temperature and the increase in in-cylinder temperature with the dual-fuel mode also contribute significantly in the formation of NOx emissions [109].

Table 6.1: Combustion data resulted from different methane replacement.

Fuel	COV of IMEP (%)	MFB50 (CAD)	Exhaust gas temperature (°C)	Spark timing (CAD bTDC)	Oxygen (%)
M0	1.45	7.8	624	24.5	0.85
M20	1.13	7.6	623	23	0.75
M40	0.85	7.5	620	21.5	0.65

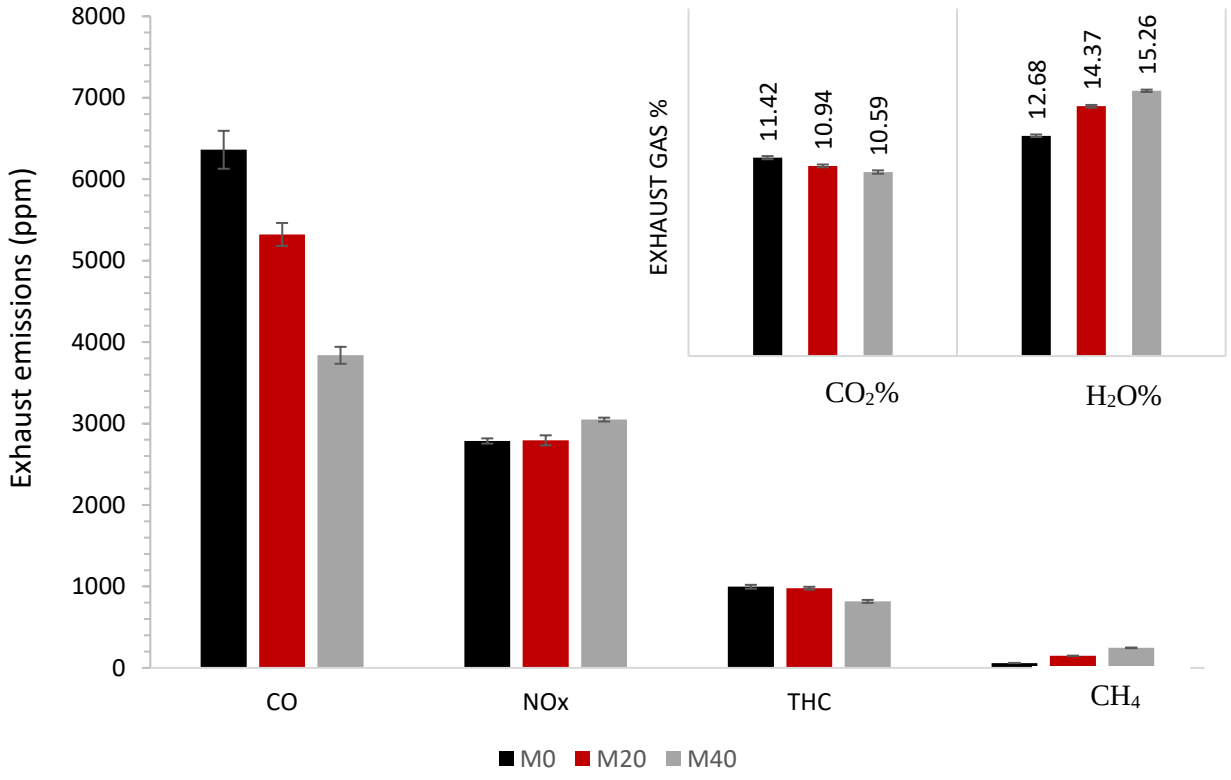


Figure 6.3: Engine-out emissions resulted from the different methane % replacement

6.3.2. Particle Size Distribution

The effect of increasing methane fuel replacement on the particle number distribution of the GDI engine is illustrated in Figure 6.4. The addition of methane gas to the combustion chamber caused a significant reduction in peak particle concentration compared to the base gasoline mode with 96% and 98% reduction observed for M20 and M40 respectively. This can be directly related to the reduction in aromatic content of the fuel mixture with the addition of methane. The initial production of particles in direct-injection engines and the subsequent increase caused by condensation and adsorption are intimately tied to the presence of aromatics in the gasoline fuel. Contrary to gasoline, methane's atomic structure lacks C-C bonds, thereby significantly lowering the formation of soot precursor species such as aromatic hydrocarbons and PAH production [106, 123]. In addition to this, the incorporation of the gaseous fuel and the subsequent reduction of the quantity of gasoline fuel delivered via direct injection coupled with a delay in the spark timing improved the mixing conditions inside the combustion chamber leading to a more homogenous mixture. This in turn reduced the fuel-rich areas in which the carbonaceous primary particles are formed and the availability of these particles to undergo pyrolysis reaction naturally reduced (123).

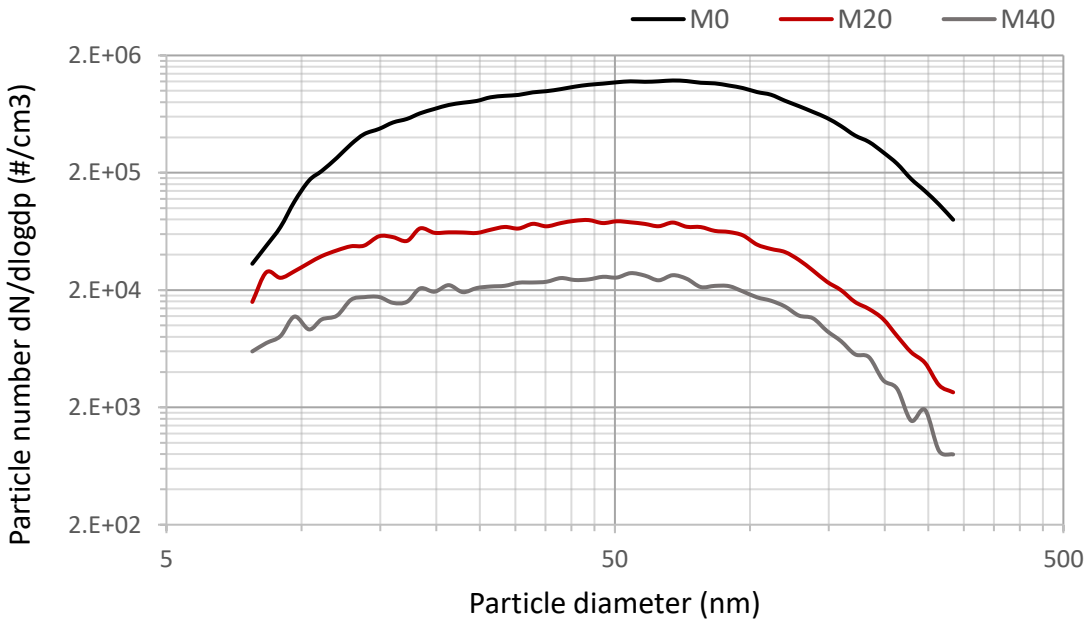


Figure 6.4: SMPS measurements of particle size distribution.

As can be seen from the figure, maximum gasoline agglomerate diameter was at 67 nm, while M20 exhibited a peak of 44 nm agglomerates, and M40 had a 55 nm peak. Similar to what J. Alanen et al. [109] found while using NG alone. M20 and M40 distributions were rather flat, suggesting a varied range of agglomeration sizes, with a median size of 40-60 nm. It is hypothesized that using methane dual-fuelling would reduce peak agglomeration size, which agrees with results from the literature for NG engines [109]. Morphological study of the collected soot will support this notion (shown later in section 6.4.). The accumulation of gas-phase hydrocarbons and precursors (like PAH) is the primary contributor to the increase in particle size as well as their surface area [106]. Due to the lower C/H ratio of the gaseous fuel, the quantity of carbonaceous species that can undergo pyrolysis reactions was significantly reduced, therefore hindering the formation of primary particles. Moreovoer, the lower particle concentration with the dual-fuel reduces the likelihood of collisions that produces bigger agglomerates.

6.3.3. Soot Oxidative Reactivity (TGA)

TGA analysis was performed to calculate the soot ignition temperature, defined as the temperature at which maximum mass loss occurs, and soot activation energy, which are means to evaluate the sample oxidative reactivity. The thermogravimetric profiles of the different soot samples are detailed in Figure 6.5.

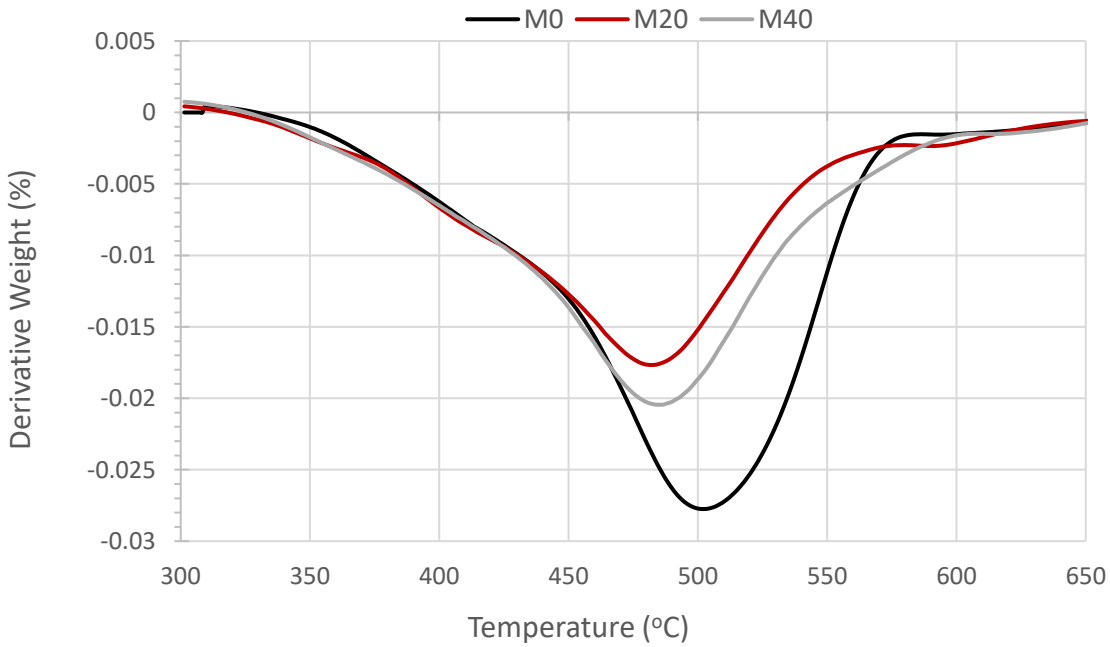


Figure 6.5: Mass profile and weight loss rate of the collected soot samples.

The maximum mass loss rate temperature (MMLRT) was determined by plotting the mass loss rate (dm/dt). From the results obtained, the MMLRT peak for both methane loaded samples has shifted towards lower temperatures. However, soot oxidation for all three samples started at approximately the same temperature (335 ºC ± 2 ºC) and the mass loss rate was maintained the same until approximately 445 ºC ± 3 ºC. This trend indicates that the difference shown in the MMLRT across the three samples is due to the differences in the mass of the analysed soot as demonstrated in a previous study [130].

Table 6.2: Start of oxidation, MMLRT and elemental soot fraction of the different samples.

Soot sample	Start of oxidation (°C)	MMLRT (°C)	Elemental soot (%)
M0	337 ± 3	511 ± 3	78.0 ± 1
M20	335 ± 3	483 ± 3	71.3 ± 1
M40	335 ± 2	473 ± 3	74.4 ± 1

A simple kinetic analysis has been carried out to estimate the soot activation energy (Ea) of the three samples in order to further assert the difference in the particles reactivity displayed in Figure **6.6**. The temperature range that leads to the most linear data trend was used to calculate the Ea with a correlation coefficient greater than 0.98 for all cases. As shown from the figure, the three samples had similar gradients indicating similar activation energies and the slight difference at higher temperatures is due to the difference in mass of the collected PM as stated in [130] rather than due to particle characteristics. These results suggest that the soot produced from the combustion of dual methane-gasoline present the same oxidation potential to that of the neat gasoline soot and infers that gasoline particles are also the predominant source in the dual-fuel mode. These findings evidently imply that GPFs can be efficiently employed in the aftertreatment system of the dual-fuel system and due to the lower elemental soot concentration (Table 6.2), their regeneration process will prove more effective. Nithyanandan et al. [126] characterised soot from diesel-CNG combustion and found that soot reactivity

with 40% CNG (energy based substitution) was similar to that for neat diesel. However, soot reactivity significantly increased when increasing CNG substitution rate to 70%. From their work we can suggest that higher methane substitutions in gasoline engines might have an impact on the particle's reactivity. However, further research should be conducted before reaching this conclusion.

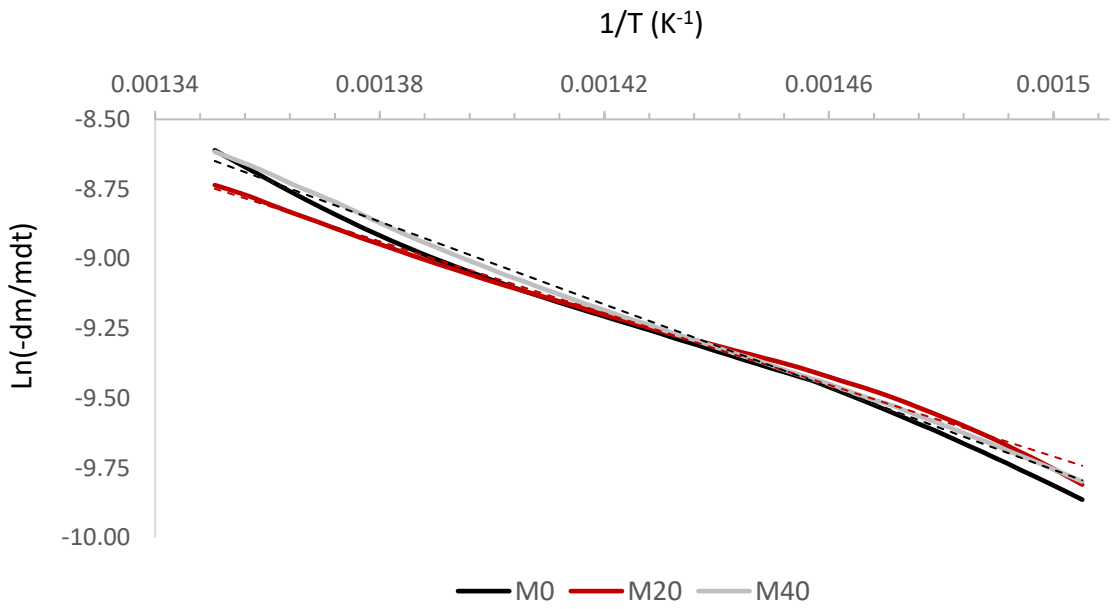


Figure 6.6: Impact of the fuelling condition on soot activation energy.

6.3.4. Particle Morphology Analysis

6.3.4.1. TEM Micrograph Images

Figure **6.7** illustrates the TEM micrographs of the particles obtained for the M0, M20, and M40 tests. As can be seen from the figure, M20 and M40 grids exhibited comparable particle counts, but gasoline grids had significantly more agglomerates, even though the sampling times were similar. This agrees with the particle reduction seen in the SMPS section (**Error! Reference source not found.**). S oot aggregate size is determined by the accumulation of numerous spherules (collisional aggregation) which is lower in the dual-fuel case compared to the gasoline only [131]. The addition of methane significantly lowers the formation of soot precursor species during combustion, hence particles collide less frequently, resulting in smaller soot aggregates. A characteristic aciniform-like shape similar to diesel soot could be seen in the agglomerates from all fuelling cases, with only minor differences

between the samples. Gasoline soot had large overall agglomerate size which are more compact and clustered compared to the CNG cases. The addition of methane reduced the number of particles and as a result the dual-fuel soot have smaller overall agglomerate size with more open loops, often only comprising of single chain of particles. In order to quantify any visual differences that were seen, statistical analysis was performed and discussed in the following sections.

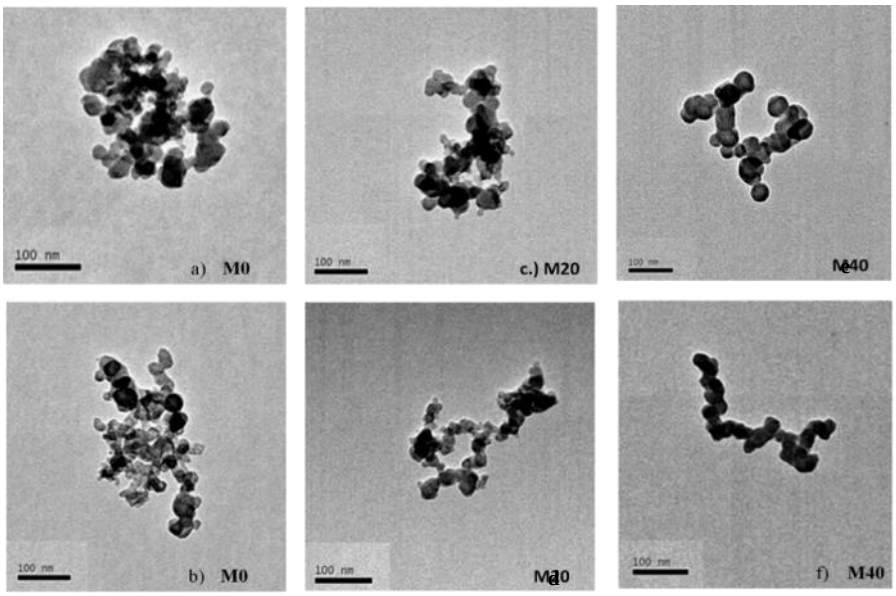


Figure 6.7: TEM micrographs collected from a-b.) M0, c-d.) M20 and e-f.) M40.

6.3.4.2. Primary Particle Size (dp0)

Transmission electron microscopy (TEM) was used to examine roughly a minimum of 200 primary particles randomly selected from at least 30 agglomerates collected on TAAB Formvar copper grids for each fuelling condition. This was done to ensure enough sample data is collected for a log-normal distribution and to determine the relevance of results relative to initial conditions. For this purpose, a One-sample Kolmogorov Smirnov test was performed using IBM statistical package for social sciences (SPSS) software (Table **6.3**). Figure **6.8** demonstrates a histogram and log-normal distribution for the primary particles resulted from the combustion of the different fuelling conditions.

The results showed that the mean dp0 for the M20 and M40 fuelling conditions were 29.22 nm and 27 nm respectively. On the other hand, the gasoline sample contained the highest proportion of particles with a diameter of less than or equal to 25 nm which is similar to other work reported in the literature [132-136]. ANOVA testing indicated a statistical difference in dpo (nm) between the three samples particularly between the M0 and M40 cases. These results indicate a slight increase in primary particle size as the amount of methane susbtitution increases. The size of primary particles is determined by a combination of surface growth, and soot oxidation mechanisms [135]. The substitution of gasoline fuel with methane gas reduced the oxygen content of the fuel mixture due to the chemical structure of methane which only contains C/H atoms. This reduced the net oxidation potential of the primary particles in the dual-fuel mode.

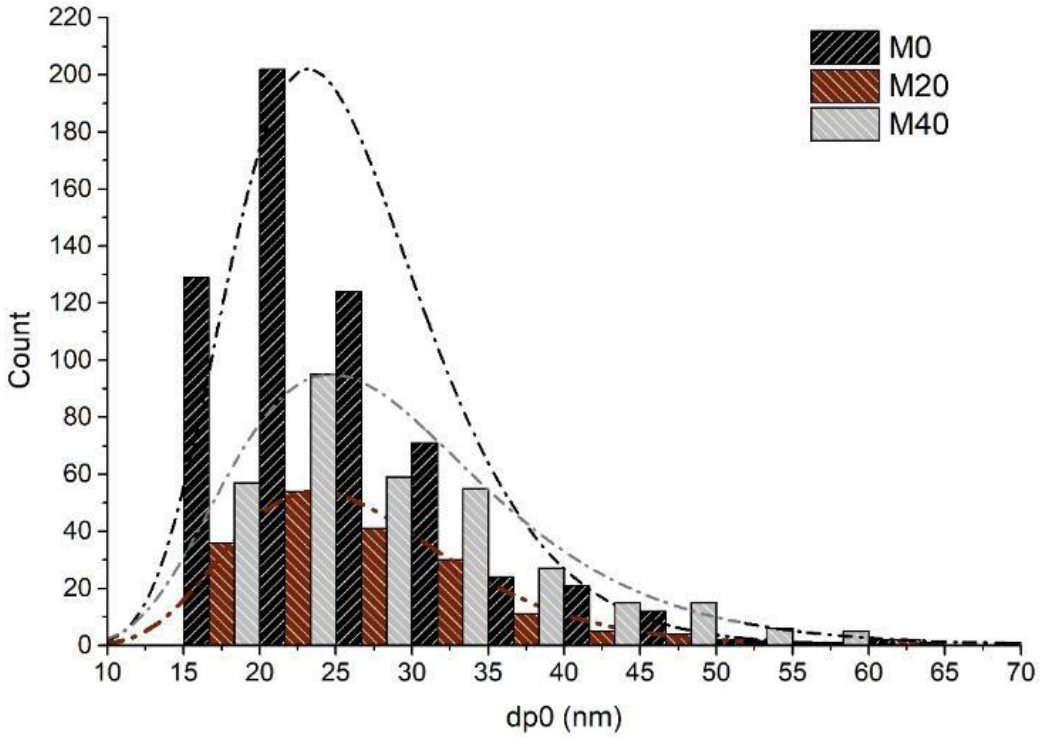


Figure 6.8: Log-normal primary particle distribution for M0, M20 and M40 cases.

Table 6.3: Statistical normality of distribution

Fuel	M0	M20	M40
Primary particles count	602	200	368
Average dpo (nm)	25.34	27.13	29.45
Standard deviation (nm)	7.13	8.42	12.25

6.3.4.3. PM Morphology Characteristics

Figure **6.9** demonstrate an average result of the morphological data obtained from at least 30 images for each fuelling case. In general, the number of primary particles (npo) is reduced as a result of using methane dual-fuel. Primary particles agglomerated in methane were approximately 25-26 whereas those in gasoline were on the order of 30. Only a small difference existed between the M20 and M40 cases. This illustrates that the main particles are smaller in M20 and M40 than they are in gasoline, further supporting SMPS data. Conversely, the increase in methane substitution in the fuel mixture lead to a slight increase in the radius of gyration (R_g), which is a measure of the aggregate's inertial size. ANOVA analysis, on the other hand, discovered no significant differences between the tested samples and the error bars overlap as shown in the figure. This suggest that methane substitution had minimal effect on R_g which is contrary to the findings of SMPS in section 6.3.2 where gasoline particles were of larger diameters. This difference might be attributed to differences in the sampling conditions between TEM (raw exhaust gas) and SMPS (diluted exhaust gas) analysis. The requirement of a dilution process in the case of SMPS might impact surface growth, adsorption of liquid particles on the soot surface and dynamic collision reactions [111,124-126] and thus particle size [46].

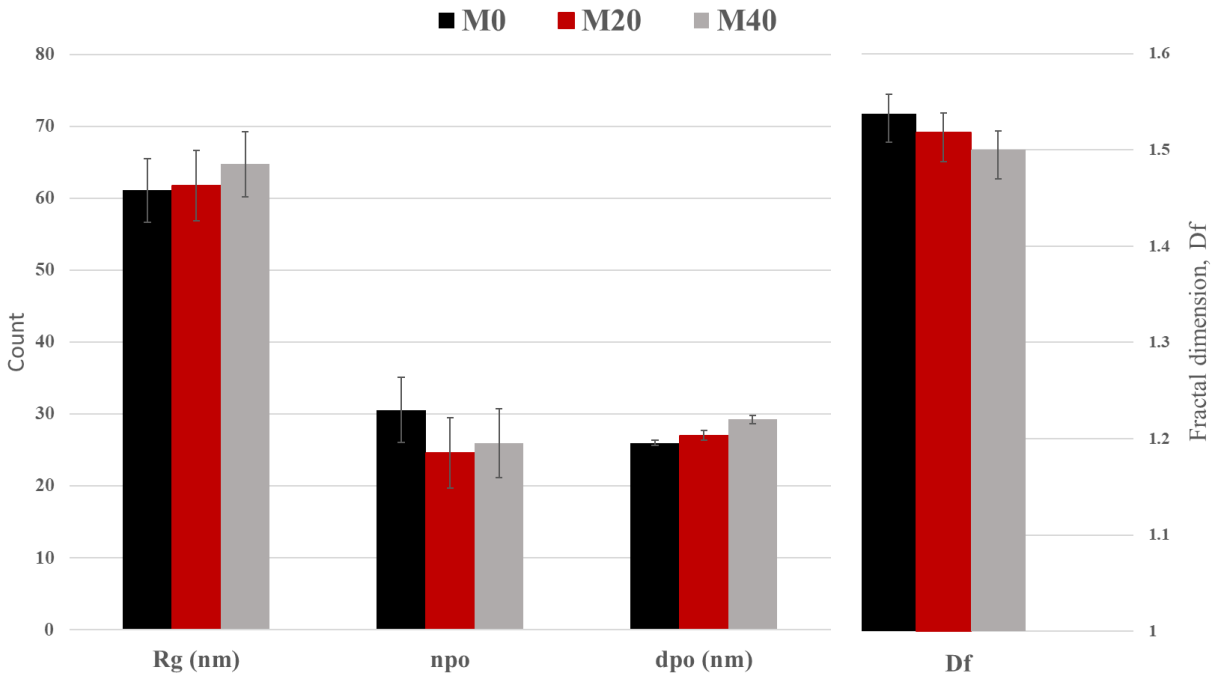


Figure 6.9: Data count for the respective morphological parameters with M0, M20 and M40.

The effect of increasing methane substitution on the particle's fractal dimension (D_f) is shown in Figure **6.9**. Typically, the higher the D_f value the more spherical and clustered the particles are likely to be, while longer chainlike structures have lower D_f values [131]. The results show a decreasing trend in D_f value with the addition of methane. Gasoline particles had the highest mean fractal dimension value of 1.54 followed by M20 (1.52) and M40 (1.5) respectively. This is in agreement with the TEM micrograph images seen in section 6.3.4.1 where gasoline particles were visibly more compact. An overall drop in primary particle numbers per agglomerate, as well as a shift toward larger chain-like particles, were shown to be the most significant effects of methane fueling addition on the size of primary particles. On the other hand, methane fueling had no effect on the Rg data, suggesting that the agglomeration formation mechanisms were primarily caused by locally gasoline-rich processes.

6.3.5. Primary Particle Nanostructure Analysis

In order to analyse the effect of methane substitution on the nanostructure of the primary particles, High-resolution TEM images of the three soot samples were studied (Figure **6.10**).

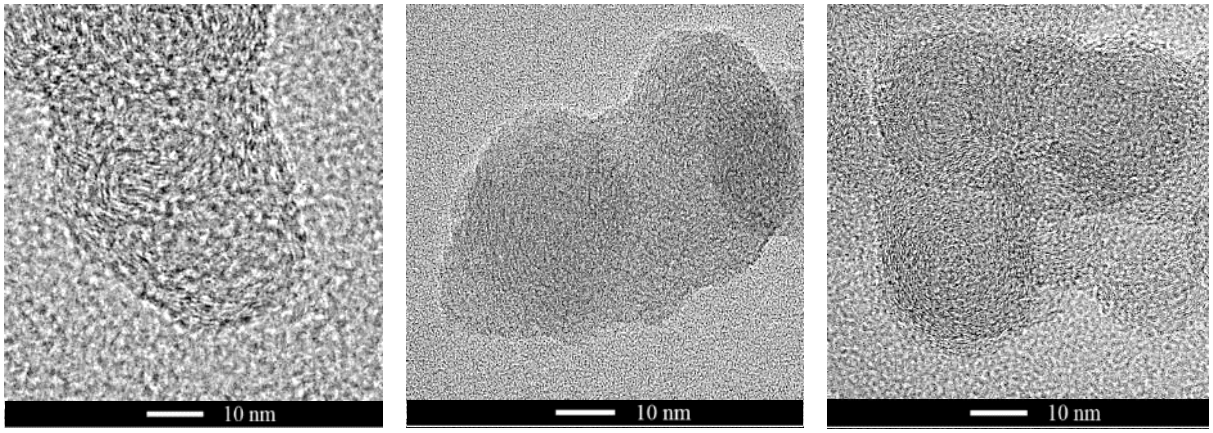


Figure 6.10: HR-TEM micrographs of primary particle nano-structure: a) M0, b) M20, and c) M40.

All three samples showed a characteristic onion-like fringes surrounding an amorphous core, typical of GDI engine particles described in the literature [134-138]. The inner cores (formed due to curved short fringes) demonstrate a typical disordered structure containing one or several nucleation sites [139]. The outer shell consists of inter-connected parallel graphene layers concentrically arranged to form a shell-like structure, although they are not generally as well ordered as compared to diesel soot [140-144].

Quantitative analysis of the HRTEM images were conducted as it provides several statistical data describing the particles nanostructure parameters. The interlayer spacing, fringe length and tortuosity normal distribution results are illustrated in Figure **6.11** a, b and c respectively to clearly show the variation across the particles, while the mean values are presented in Table **6.4**.

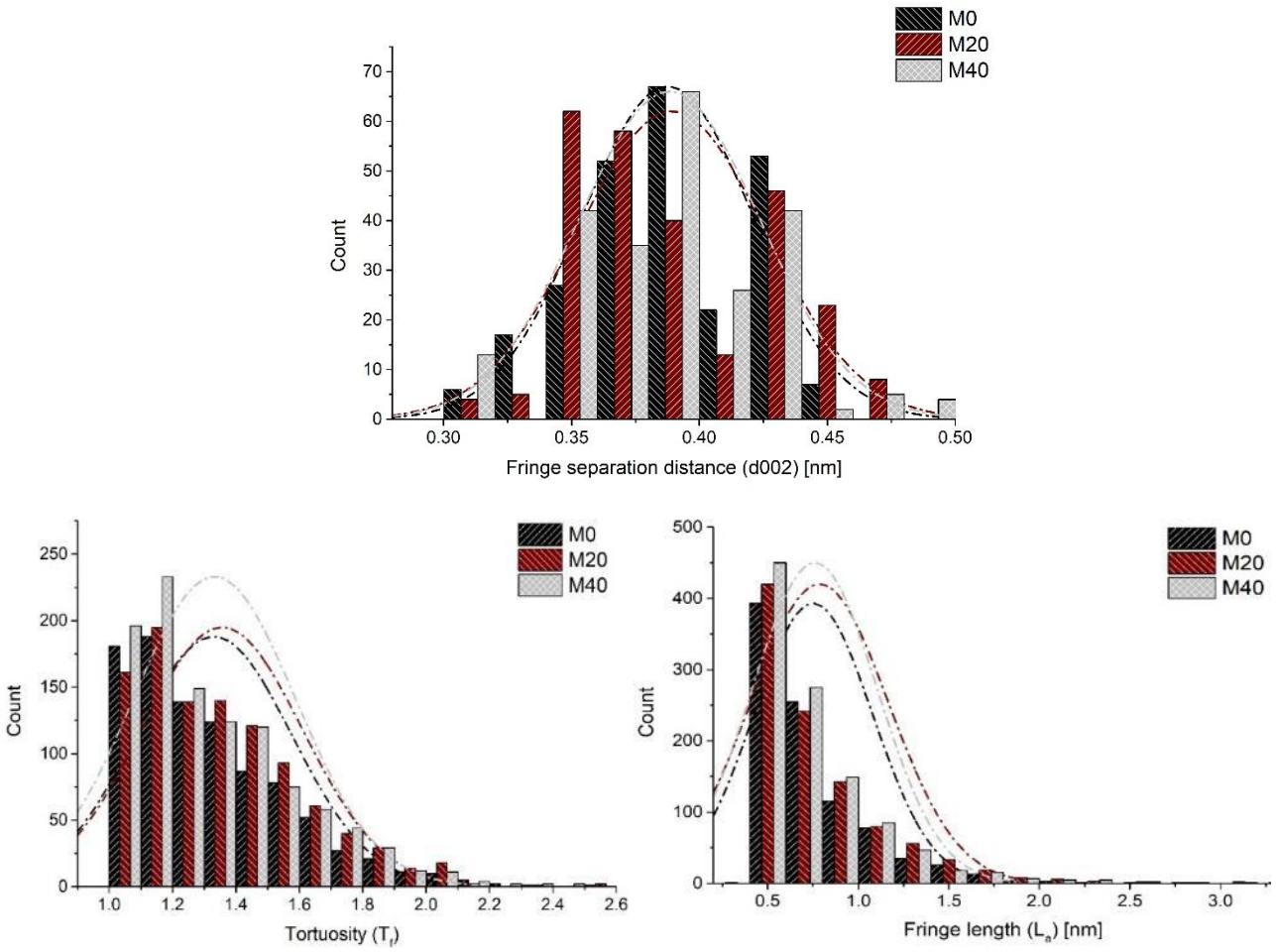


Figure 6.11: Associated nanostructure parameters of the three samples a) fringe separation distance, d002 b) Tortuosity, Tf and c) Fringe length, La.

Table 6.4: Median values of the nano structural parameters for the different fuelling conditions.

Sample	Fringe separation distance (d002)	Fringe length (L_a)	Tortuosity (T)
M0 **(St. dev)**	0.388 ± 0.002	0.751 ± 0.326	1.329 ± 0.247
M20 **(St. dev)**	0.389 ± 0.002	0.786 ± 0.379	1.356 ± 0.254
M40 **(St. dev)**	0.388 ± 0.002	0.759 ± 0.345	1.332 ± 0.256

The results show that methane substitution into the cylinder have insignificant impact on the fringe separation distance, fringe length and tortuosity with all values falling within a similar range. Nanostructure parameters are normally associated with particle reactivity. Overall, a larger percentage of more reactive carbon atoms may be found at the edge-site of longer La whereas higher Tf (more

curved fringes) has more bond strain than flat lamella, suggesting that the carbon atoms are more reactive [145]. Since no changes in the particle's nanostructure can be seen with methane substitution in this work, it is apparent that the particles have similar oxidative potential. This supports the TGA findings reported earlier in section 3.3.

Following the results, it can be concluded that nanostructure analysis has shown that the dual fuel soot samples have similar carbon nanostructures to GDI soot irrespective of methane substitution quantity. However, Nithyanandan et al. [126] who studied the nanostructure of particles collected from 40% and 70% CNG combustion in a CI engine found that while CNG40 showed no significant differences to neat diesel, CNG70 demonstrated signs of immature soot. Therefore, in light of their work, further research should be conducted to assert whether higher substitution of methane will have any impact on the particle's nanostructure in a GDI engine.

6.3.6. Raman Spectroscopy

The Raman spectra produced from the gasoline and dual-fuel samples is illustrated in Figure **6.12** and was deconvoluted using the 3 Lorentzian and one Gaussian band (3L1G). Additionally, the various spectra fittings used to characterise the structural properties and reactivity of the soot samples are presented in Table **6.5**.

Table 6.5: Representative Raman spectra fittings for each fuel condition.

Sample	**FWHM D1**	**I_{D1}/I_G**	**A_{D1}/A_G**	**A_{D3}/A_G**	**A_{D4}/A_G**
M0	151.145	0.914	2.004	0.440	0.618
(Std. dev)	±0.42	±0.0048	±0.033	±0.049	±0.0013
M20	145.681	0.905	1.998	0.507	0.526
(Std. dev)	±4.01	±0.015	±0.068	±0.019	±0.012
M40	122.584	0.891	1.982	0.693	0.370
(Std. dev)	±8.41	±0.015	±0.039	±0.050	±0.016

The FHWM D1 band can provide information about the crystallite size where a lower value indicates a higher level of soot order [146, 147]. Similarly, the ratios of I_{D1}/I_G and A_{D1}/A_G have been utilised to analyse the nanostructure and establish a connection with soot's reactivity. Analysing the results presented in Table **6.5**, it can be concluded that there is statistically insignificant difference between soot order and reactivity of M0 and M20 samples with both values overlapping each other. A noticeable decrease in the height and area of the D1 and G bands can however be seen from the M40 sample. This implies a lower amount of carbon structural disorder compared to M0 and hence a decrease in the number of carbon edge sites vulnerable to oxidation [148, 149]. Furthermore, the ratio of I_{D3}/I_G or A_{D3}/A_G can reveal the percentage of amorphous nanostructure in PM, hence these ratios were also evaluated in the study. A lower amount of amorphous carbon was likely responsible for the higher D3 band in the dual-fuelling modes compared to the pure gasoline mode, once more implying that the nanostructure of the carbon particles was more structured at M40.

These findings suggest that a decrease in the net oxygenated content of the dual-fuel may have contributed to the more ordered structure of the primary particles in M40. The substitution of gasoline (which contains 5% oxygenated ethanol) with CH_4 resulted in primary particles with a reduced oxygen content decreasing the potential of undergoing partial or capsule-style oxidation [150-152]. This is evidenced by the dpo analysis presented earlier in section 6.3.4.2, which indicates that larger, more complete, and more highly organised primary particles were created. Hence, Raman results insinuate soot's oxidation reactivity decreases with dual-fuel mode, which does not correspond well with the absence of differences between the HR-TEM and soot reactivity results obtained from TGA analysis when particles for M0, M20 and M40 were compared. Dissimilarities between Raman and TGA results have been previously reported in the literature [135].

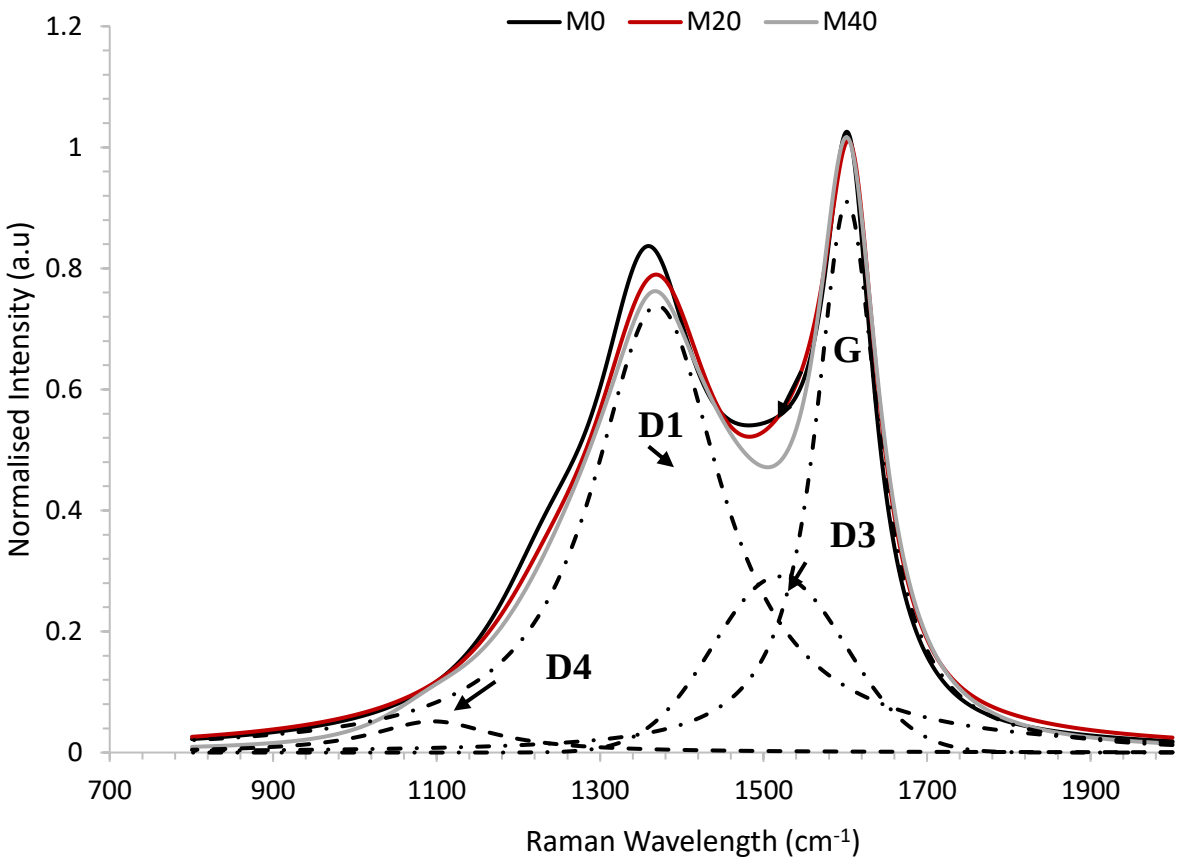


Figure 6.12: Average Raman spectrum representative for each fuelling condition.

6.4. Summary

In this study, gaseous emissions and particulate matter were analysed and evaluated to determine the effect of dual-fuelling in a GDI engine and compared to a gasoline-only mode. Physicochemical characterisation of the PM emitted from the dual-fuel combustion was carried out using SMPS, TGA, TEM, HRTEM and Raman.

The research showed that by lowering the C/H fuel ratio and enhancing the mixing mechanics within the engine, the addition of gaseous methane fuel may eliminate in-cylinder pyrolysis processes and drastically cut down on engine particle numbers. Results from SMPS and TEM showed that the number of agglomerates was reduced by 98% and primary particle numbers by 20%, respectively for the M40 condition. According to TEM pictures, there was minimal variation in the particle shapes presented between the cases; with all displaying the characteristic fractal-like shape. However, particles produced from the dual-fuelling were more chain-like in structure. With methane dual-fueling, the

primary particle size distribution shifted toward larger particle sizes, leading to a greater mean primary particle diameter. This was attributed to higher surface growth rate due to the lowered oxidation mechanisms in the dual-fuel case. This is consistent with the findings of the Raman analysis, which indicates that more highly organised soot was created at higher methane fractions. No statistically significant difference was detected between the two cases when other morphological parameters, such radius of gyration, were compared.

Particles emitted from the dual-fuel combustion showed no difference in soot oxidation reactivity compared to neat gasoline soot. The findings from this study imply that GPFs can be efficiently employed in the aftertreatment of the dual-fuel system. The lower PM concentration resulted from the dual-fuel mode eases the back pressure induced on GPFs and reduces the frequency of regeneration events required to oxidise the accumulated particles. High-resolution TEM images of the samples showed a characteristic onion-like fringes surrounding an amorphous core, typical of GDI engine particles. No clear difference in the nano-structure across the different soot samples can be deduced. The lack of effect on soot oxidation and nanostructure by methane substitution suggests that gasoline was instrumental in driving the primary particle and agglomerate producing mechanisms in the cylinder.

The research findings suggest that using methane gas as an alternative to gasoline could significantly reduce the quantity of particles released by GDI engines. Since this is the first study toward quantifying the particle morphological impact of methane dual-fuelling, it should encourage further investigation into the development of dual-fuelling strategies with natural gas and provide additional insight into the performance of the particles and gaseous emissions produced in aftertreatment systems.

7. Conclusion and Future Work

7.1. Conclusion

The European Union target of 95 g CO2/km and the further 37.5% emissions reduction target expected by 2030 urge the need to find low carbon footprint solutions. Consequently, a dual-fuelled system was examined in this Thesis to reap the benefits of both a highly efficient and power-dense GDI system and the reduction of particle emissions and gaseous emissions with natural gas. The main aim of this work was to fill the literature gap in the aftertreatment system of dual-fuel engines by simultaneously reducing CO_2 and CH_4 emissions without considerable losses in engine performance and fuel economy.

The main challenges of the CNG engine fuelling in terms of methane abatement in the aftertreatment system is addressed in this study by the use of different loaded PGM catalysts and engine control strategies. The dual-fuel injection of methane-gasoline provides an alternative solution for vehicle manufacturers to meet future emission targets, possibly using only a CNG catalyst. Results indicate that increasing the Pd loading led to significantly earlier light-off temperatures achieved at relatively lower temperatures of 340, 350 and 395ºC respectively. However, the benefit diminishes above Pd loading >142.5 g ft. The study has also demonstrated that NH_3 is formed over the CNG catalyst due to steam-reforming reactions from the increased levels of methane in the exhaust with the dual-fuelling. Hence aftertreatment technologies such as SCR should be adopted to remove them. This further highlights the need to regulate the harmful NH_3 emissions from future passenger cars fuelled with CNG. In addition, the benefits of the dual-fuel system in terms of lower engine output CO_2, non-methane hydrocarbon (NMHC) and particulate matter (PM) emissions compared to the GDI mode alone were emphasised in the study.

Two full-scale Pd/Rh and Pt/Rh catalysts performance were assessed and compared under varied engine lambda conditions and cycle air/fuel ratios. The results showed that, in general, the two catalysts work quite similarly and that, under stoichiometric engine settings, both Pd and Pt were very efficient at oxidising hazardous exhaust emissions, in particular methane. However, under lean/rich conditions

the catalysts efficiency dropped which emphasised the importance of utilising a combination of all three PGMs (Pd, Pt and Rh) in order to have an efficient aftertreatment system across different lambda settings. Moreover, the study investigated the possibility of improving fuel economy by developing rich/lean cycles in combination with catalyst characteristics (oxygen storage capacity, PGM content etc.). It was demonstrated that the introduction of short rich spikes can aid the catalyst to regain its performance after the lean period, while the importance of an intermediary stoichiometric point to prevent NOx overshoot was highlighted. The positive results yielded in this study should encourage further development in aftertreatment test cycles corresponding to the Worldwide Light-duty Test Cycle (WLTC) and Real Driving Emissions (RDE).

Gasoline Direct Injection (GDI) engines present significant advantages in terms of fuel economy, CO_2 and other gaseous emissions with respect to their port fuel injection (PFI) counterparts, but still produce pollutants that contribute to greenhouse effects and higher particulate matter (PM) levels than PFI. The use of natural gas as an alternative fuel can greatly reduce the environmental impact of GDI engines as it produces significantly lower PM emissions compared to petroleum fuels. This is due to its low carbon content, good mixing capabilities and cleaner combustion. Natural gas entering the cylinder pre-mixed with air provides a more homogenous air-fuel mixture, and reduces particle producing pyrolysis reactions. Particle size distribution, reactivity, nanostructure, and morphology were studied at three different energy densities of gasoline substitution for methane, M0, M20 and M40. The study demonstrated that due to the more uniform combustion and lower carbon ratio in the fuel, methane-gasoline dual-fueling can result in a 98 percent reduction in particle emissions. Transmission electron microscopy (TEM) indicated that primary particle sizes increased slightly with increased methane fuel fraction, whereas the number of primary particles per agglomerate decreased. In addition, radius of gyration, and nanostructure characteristics for the soot particles formed by gasoline and the dual fuel modes were indistinguishable. This indicates that the more concentrated gasoline fuel is the primary source of soot formation and shape. Consistently, soot reactivity, characterised by TGA, showed no difference in the oxidation potential of the collected PM samples across all fuelling conditions.

Moreover, a 10% reduction in CO_2 was achieved by utilising the dual-fuel system. However, after-treatment considerations must be made to contain the increase in methane emissions with this strategy.

By using methane gas, the results of the research have shown that GDI engines may significantly reduce the quantity of particles they produce. Initial findings in assessing the morphological effect of methane dual-fuelling are likely to inspire further studies on how the particles and gaseous emissions generated by methane dual-fuelling systems will perform in aftertreatment systems.

7.2. Future Work

The work from this research can be further enhanced through the following suggestions:

- To investigate the use of higher concentrations of methane replacement and at higher engine speed and loads, coupled with careful engine lambda control. The results from this research have shown positive trends can be achieved with 40% CH_4 replacement in terms of engine-out emissions and fuel economy at low-medium loads. However, the advantages and/or limitations of the dual-fuel strategy should be investigated further across various engine speed and load.
- The aftertreatment system for the dual-fuel strategy should be further developed considering the results achieved in this work. Firstly, a Tri-metallic (containing Pt, Pd and Rh) catalyst formulation should be developed and investigated across a wide engine lambda. Secondly, the use of a GPF in the aftertreatment system can reduce the particle number even further especially at higher loads, which can help further in meeting emission targets.
- To investigate and address the challenge of the dual-fuel system identified in this study, Ammonia slip. The use of Urea Selective Catalytic Reduction (SCR) catalyst can be a possible solution to mitigate this problem.
- To improve and further optimise the Stoichiometric/Rich/Lean cycles proposed in this research study to achieve better fuel economy. In addition, catalyst with different oxygen storage capacity (OSC) should be used for this work to investigate the effect of OSC in greater detail during the various cycles.

Appendix 1: Publications, Projects and Awards

❖ Publications

1. Wahbi A, Tsolakis A, Herreros J. Emissions Control Technologies for Natural Gas Engines. In Energy, Environment, and Sustainability; 2019. p. 359–79. **Published**
2. Serhan, N., Tsolakis, A., Wahbi, A., Martos, F. and Golunski, S., 2019. Modifying catalytically the soot morphology and nanostructure in diesel exhaust: Influence of silver De-NOx catalyst (Ag/Al2O3). *Applied Catalysis B: Environmental*, 241, pp.471-482. **Published**
3. Mardani, M., Tsolakis, A., Nozari, H., Martin Herreros, J., Wahbi, A. and Sittichompoo, S., 2021. Synergies in renewable fuels and exhaust heat thermochemical recovery in low carbon vehicles. *Applied Energy*, 302, p.117491. **Published**
4. A. Wahbi, A. Tsolakis, J.M. Herreros, S.Z. Rezaei, A. Raj, P.J. Millington. Advanced Catalytic Technologies for CNG – Gasoline Fuelled Engines. **Submitted** to Johnson Matthey Technology Review Journal.
5. A. Wahbi, A. Tsolakis, J.M. Herreros, S.Z. Rezaei, J. Chan, K. Holland, F.J. Martos, A. Raj, P.J. Millington. Characterisation of Particulate Emissions from Methane-Gasoline Dual-Fuel Combustion in a GDI Engine. **Submitted** to Fuel Journal.

❖ Planned Future Publication

1. Wahbi, A. Tsolakis, J.M. Herreros, S.Z. Rezaei, A. Raj, P.J. Millington. Full-Scale Aftertreatment Technologies for Dual-Fuel Gasoline-Natural Gas Engine. **Submit** to Fuel Journal.
2. Wahbi, A. Tsolakis, J.M. Herreros. Effect of Water Injection on Combustion and Exhaust Emissions of Gasoline Engines.

❖ Conference

1. Wahbi, A. Tsolakis, J.M. Herreros, A. Raj, P.J. Millington. After-Treatment emissions control system for Methane-Gasoline dual fuel engines. Poster Conference, Johnson Matthey Academic Conference, JMAC 2019.
2. Wahbi, A. Tsolakis, J.M. Herreros, A. Raj, P.J. Millington. Aftertreatment System Technologies For Next- Generation IC Engines Fuelled with Methane. Johnson Matthey Academic Conference, JMAC 2020.
3. Wahbi, A. Tsolakis, J.M. Herreros, A. Raj, P.J. Millington. Emissions Control Technologies for Dual Fuel Natural Gas Engines. Johnson Matthey Academic Conference, JMAC 2021.
4. Wahbi, A. Tsolakis, J.M. Herreros. Emissions Control Technologies for Dual Fuel Natural Gas Engines. International Workshop, Technologies for Emissions Control, 2021.

❖ Projects

1. Repsol, Consultancy Project: Fuel effects on Three-Way Catalyst Durability, 2018 and 2019.
2. Hyundai Motor Companu, Consultancy Project: Exhaust Fuel Reformer for Gasoline Engines, 2019
3. Johnson Matthey, Consultancy Project: Effect of Water Injection on Exhaust Emissions of Gasoline Engines, 2019.

❖ Awards

1. Fully funded Doctoral research scholarship at the University of Birmingham, 2017-2022.
2. PhD research funded by Johnson Matthey, 2018-2022.
3. TI Postgraduate Scholarship for academic achievement, 2017-2021

References

1. Eia.gov. (2018). International Energy Outlook 2016-Executive Summary - Energy Information Administration. [online] Available at: https://www.eia.gov/outlooks/ieo/exec_summ.php
2. Communication From the Commission to the European Parliament, the Council, the European Economic and Social Committee and the Committee of the Regions: A Roadmap for Moving to a Competitive Low Carbon Economy in 2050', Brussels, Belgium, 8th March, 2011.
3. BP statistical review of world energy, June 2017. Available at: https://www.bp.com/content/dam/bp/en/corporate/pdf/energy-economics/statistical-review-2017/bp-statistical-review-of-world-energy-2017-full-report.pdf
4. World energy resources, 2016. Available at: https://www.worldenergy.org/wp-content/uploads/2016/10/World-Energy-Resources-Full-report-2016.10.03.pdf
5. A.H. Kakaee, A. Paykani, Research and development of natural-gas fueled engines in Iran, Renew. Sustain. Energy Rev. 26 (2013), pp. 805-821.
6. H. Chen, J. He, X. Zhong. Engine combustion and emission fuelled with natural gas: A review. Journal of the Energy Institute (2018).
7. T. Korakianitis, A.M. Namasivayam, R.J. Crookes, Natural-gas fueled spark-ignition (SI) and compression-ignition (CI) engine performance and emissions. Prog Energy Combust Sci, 37 (2011), pp. 89-112.
8. R. L. Evans, J Blaszczyk. A comparative study of the performance and exhaust emissions of a spark ignition engine fuelled by natural gas and gasoline. Proc Inst Mech Eng Part D: J Automob Eng, 211(1) (1997), pp. 39 – 47.
9. T. Thurnheer, P. Soltic, P.D. Eggenschwiler. SI engine fuelled with gasoline, methane and methane/hydrogen blends: heat release and loss analysis. International Journal of Hydrogen Energy, 34 (5) (2009), pp. 2494-2503.

10. C. Ji, S. Wang. Effect of hydrogen addition on combustion and emissions performance of a spark ignition gasoline engine at lean conditions. International Journal of Hydrogen Energy, 34 (2009), pp. 7823-7834

11. H.M. Cho, B. He. Spark ignition natural gas engines – a review. Energy Conversion and Management, 48 (2) (February 2007), pp. 608-618.

12. J. Sevik, M. Pamminger, T. Wallner, R. Scarcelli, R. Reese, A. Iqbal, B. Boyer, S. Wooldridge, C. Hall, S. Miers. Performance, efficiency and emissions assessment of natural gas direct injection compared to gasoline and natural gas port-fuel injection in an automotive engine. SAE Int. J. Engines 9(2) (2016), pp. 1130–1142.

13. P. Bielaczyc, A. Szczotka, J. Woodburn. A Comparison of Exhaust Emissions from Vehicles Fuelled with Petrol, LPG and CNG. IOP Conference Series: Materials Science and Engineering, 148, (2016).

14. Semin, Rosli Abu Bakar. "A Technical Review of Compressed Natural Gas as an Alternative Fuel for Internal Combustion Engines ". American Journal of Engineering and Applied Sciences, 1 (4) (2008), pp. 302-311.

15. M.I. Jahirul, H.H. Masjuki, R. Saidur, M.A. Kalam, M.H. Jayed, M.A. Wazed. Comparative engine performance and emission analysis of NG and gasoline in a retrofitted car engine, Applied Thermal Engineering, 30 (14–15) (2010), pp. 2219-2226.

16. M.U. Aslam, H.H. Masjuki, M.A. Kalam, H. Abdesselam, T.M.I. Mahlia, M.A. Amalina. An experimental investigation of CNG as an alternative fuel for a retrofitted gasoline vehicle. Fuel, 85 (5) (2006), pp. 717-724.

17. US EPA. (2018). Atmospheric Lifetime and Global Warming Potential Defined | US EPA. [online] Available at: https://www.epa.gov/climateleadership/atmospheric-lifetime-and-global-warming-potential-defined.

18. M. Ehsan. Effect of spark advance on a gas run automotive spark ignition engine. J Chem Eng Jpn, 24 (1) (2006), pp. 42-49.

19. C. Reynolds, R.L. Evans, Improving emissions and performance characteristics of lean burn natural gas engines through partial stratification, Int. J. Engine Res. 5 (1) (2004) 105e114.

20. J. Alanen, E. Saukko, K. Lehtoranta, T. Murtonen, H. Timonen, R. Hillamo, et al.The formation and physical properties of the particle emissions from a natural gas engine Fuel, 162 (2015), pp. 155-161.

21. G. Karavalakis, M. Hajbabaei, Y. Jiang, J. Yang, K. Johnson, D. Cocker, T. Durbin. Regulated, greenhouse gas, and particulate emissions from lean-burn and stoichiometric natural gas heavy-duty vehicles on different fuel compositions, Fuel, 175 (2016), pp. 146-156.

22. M. Hajbabaei, G. Karavalakis, K. Johnson, L. Lee, T. Durbin. Impact of natural gas fuel composition on criteria, toxic, and particle emissions from transit buses equipped with lean burn and stoichiometric engines, Energy, 62 (2013), pp. 425-434.

23. P. Einewall, P. Tunestål, B. Johansson. Lean Burn Natural Gas Operation vs. Stoichiometric Operation with EGR and a Three Way Catalyst. SAE Technical Paper (2005) (2005-01-0250).

24. I. Saanum, M. Bysveen, P. Tunestål, B. Johansson. Lean Burn Versus Stoichiometric Operation with EGR and 3-Way Catalyst of an Engine Fueled with Natural Gas and Hydrogen Enriched Natural Gas. SAE Technical (2007) (2007-01-0015).

25. H.M. Cho, B.Q. He. Combustion and emission characteristics of a lean burn natural gas engine. Int J Automotive Technol, 9 (2008), pp. 415-422

26. R.M. Heck, R.J. Farrauto. Automobile exhaust catalysts. Appl Catal A Gen, 221 (2001), pp. 443-457.

27. U.G. Alkemade, B. Schumann. Engines and exhaust after treatment systems for future automotive applications. Solid State Ion, 177 (2006), pp. 2291-2296.

28. M.M. Abdelaal, A.H. Hegab. Combustion and emission characteristics of a natural gas-fueled diesel engine with EGR. Energy Conversion and Management, 64 (2012), pp. 301-312.

29. P. Dimopoulos, C. Bach, P. Soltic, K. Boulouchos. Hydrogen–natural gas blends fuelling passenger car engines: Combustion, emissions and well-to-wheels assessment. International Journal of Hydrogen Energy, 33 (23) (2008), pp. 7224-7236.

30. HM. Cho, B.Q. He. Combustion and Emission Characteristics of a Natural Gas Engine under Different Operating Conditions. Environmental Engineering Research, 14 (2009), pp. 95-101.

31. H. Alrazen, K. Ahmad. HCNG fueled spark-ignition (SI) engine with its effects on performance and emissions. Renew Sustain Energy Rev, 82 (1) (2018), pp. 324-342

32. B. Açıkgöz, C. Çelik, H.S. Soyhan, B. Gökalp, B. Karabağ. Emission characteristics of a hydrogen-CH4 fuelled spark ignition engine. Fuel, 159 (2015), pp. 298-307

33. R.K. Mehra, H. Duan, R. Juknelevičius, F. Ma, J. Li. Progress in hydrogen enriched compressed natural gas (HCNG) internal combustion engines — a comprehensive review. Renew Sustain Energy Rev, 80 (2017), pp. 1458-1498

34. S. Lee, C. Kim, Y. Choi, G. Lim, C. Park. Emissions and fuel consumption characteristics of an HCNG-fueled heavy-duty engine at idle. Int J Hydrogen, 39 (2014), pp. 8078-8086.

35. A. Raj, Johnson Matthey Technol. Rev., 2016, 60, (4), 228 doi:10.1595/205651316x692554

36. D. Adouane, S. Capela, P. Da Costa, On the efficiency of NH3eSCR catalysts for heavy duty vehicles running on compressed natural gas in synthetic gas bench scale, Top. Catal. 56 (1e8) (2013) 45-49.

37. I. Gogolev, J. Wallace. Performance and emissions of a compression-ignition direct-injected natural gas engine with shielded glow plug ignition assist, Energy Conversion and Management, (164) (2018), pp. 70-82.

38. M. Khan, T. Yasmin, A. Shakoor. Technical overview of compressed natural gas (CNG) as a transportation fuel. Renewable and Sustainable Energy Reviews, 51 (2015), pp.785-797.

39. K. Bhandari, A. Bansal, A. Shukla, M. Khare. Performance and emissions of natural gas fuelled internal combustion engine: a review. J Sci Ind Res, 64 (2005), pp. 333-338

40. L. Wei, P. Geng. A review on natural gas/diesel dual fuel combustion, emissions and performance. Fuel Processing Technology, 142 (2016), pp, 264-278.

41. L. Sun, Y.F. Liu, K. Zeng, R. Yang, Z.H. Hang. Combustion performance and stability of a dual-fuel diesel–natural-gas engine. Proc. Inst. Mech. Eng. D J. Automob. Eng., 229 (2) (2015), pp. 235-246.

42. J. Liu, F. Yang, H.W. Wang, M.G. Ouyang, S.G. Hao. Effects of pilot fuel quantity on the emissions characteristics of a CNG/diesel dual fuel engine with optimized pilot injection timing. Appl. Energy, 110 (0) (2013), pp. 201-206.

43. G.H. Abd Alla, H.A. Soliman, O.A. Badr, M.F. Abd Rabbo. Effect of pilot fuel quantity on the performance of a dual fuel engine. Energy Conversion and Maagement, 41 (6) (2000), pp. 559-572.

44. O.M.I. Nwafor. Effect of choice of pilot fuel on the performance of natural gas in diesel engines. Renewable Energy, 21 (3–4) (2000), pp. 495-504.

45. S. Imran, D.R. Emberson, B. Ihracska, D.S. Wen, R.J. Crookes, T. Korakianitis. Effect of pilot fuel quantity and type on performance and emissions of natural gas and hydrogen based combustion in a compression ignition engine, International Journal of Hydrogen Energy, 39 (10) (2014), pp. 5163-5175.

46. A.M. Namasivayam, T. Korakianitis, R.J. Crookes, K.D.H. Bob-Manuel, J. Olsen. Biodiesel, emulsified biodiesel and dimethyl ether as pilot fuels for natural gas fuelled engines, Applied Energy, 87 (3) (2010), pp. 769-778.

47. G Abd Alla, H Soliman, O Badr, M. Abd Rabbo. Effect of injection timing on the performance of a dual fuel engine. Energy Conversion and Management, 43 (2002), pp. 269-277.

48. B.B. Sahoo, N. Sahoo, U.K. Saha. Effect of engine parameters and type of gaseous fuel on the performance of dual-fuel gas diesel engines—A critical review, Renewable and Sustainable Energy Reviews, 13 (6–7) (2009), pp. 1151-1184.

49. L. Zhou, Y.-F. Liu, C.-B. Wu, L. Sun, L. Wang, K. Zeng, et al. Effect of the diesel injection timing and the pilot quantity on the combustion characteristics and the fine-particle emissions in a micro-diesel pilot-ignited natural-gas engine. Proc. Inst. Mech. Eng. D J. Automob. Eng., 227 (8) (2013), pp. 1142-1152

50. Cho HM, He BQ. Spark ignition natural gas engines-A review. Energy Conversion and Management. 2007 Feb;48(2):608–18.

51. Korakianitis T, Namasivayam AM, Crookes RJ. Natural-gas fueled spark-ignition (SI) and compression-ignition (CI) engine performance and emissions. Vol. 37, Progress in Energy and Combustion Science. 2011. p. 89–112.

52. Wahbi A, Tsolakis A, Herreros J. Emissions Control Technologies for Natural Gas Engines. In Energy, Environment, and Sustainability; 2019. p. 359–79.

53. Tabar AR, Hamidi AA, Ghadamian H. Experimental investigation of CNG and gasoline fuels combination on a 1.7 L bi-fuel turbocharged engine. International Journal of Energy and Environmental Engineering. 2017 Mar 1;8(1):37–45.

54. Obiols J, Soleri D, Dioc N, Moreau M. Potential of Concomitant Injection of CNG and Gasoline on a 1.6L Gasoline Direct Injection Turbocharged Engine. JSAE. 2011.

55. Singh E, Morganti K, Dibble R. Dual-fuel operation of gasoline and natural gas in a turbocharged engine. Fuel. 2019 Feb 1;237:694–706.

56. Chen Z, Wang L, Zeng K. A comparative study on the combustion and emissions of dual-fuel engine fueled with natural gas/methanol, natural gas/ethanol, and natural gas/n-butanol. Energy Conversion and Management. 2019 Jul 15;192:11–9.

57. Xu Y, Zhang Y, Gong J, Su S, Wei Z. Combustion behaviours and emission characteristics of a retrofitted NG/gasoline duel-fuel SI engine with various proportions of NG-gasoline blends. Fuel. 2020 Apr 15;266.

58. Lehtoranta K, Murtonen T, Vesala H, Koponen P, Alanen J, Simonen P, et al. Natural Gas Engine Emission Reduction by Catalysts. Emission Control Science and Technology. 2017 Jun 1;3(2):142–52.

59. Raj A. Methane emission control. Vol. 60, Johnson Matthey Technology Review. Johnson Matthey Public Limited Company; 2016. p. 228–35.
60. Chen H, He J, Zhong X. Engine combustion and emission fuelled with natural gas: A review. Vol. 92, Journal of the Energy Institute. Elsevier B.V.; 2019. p. 1123–36.
61. Tree DR, Svensson KI. Soot processes in compression ignition engines. Vol. 33, Progress in Energy and Combustion Science. 2007. p. 272–309.
62. Karavalakis G, Durbin TD, Villela M, Miller JW. Air pollutant emissions of light-duty vehicles operating on various natural gas compositions. Journal of Natural Gas Science and Engineering. 2012 Jan;4:8–16.
63. Alanen J, Saukko E, Lehtoranta K, Murtonen T, Timonen H, Hillamo R, et al. The formation and physical properties of the particle emissions from a natural gas engine. Fuel. 2015 Dec 15;162:155–61.
64. Nithyanandan K, Lin Y, Donahue R, Meng X, Zhang J, Lee C fon F. Characterization of soot from diesel-CNG dual-fuel combustion in a CI engine. Fuel. 2016 Nov 15;184:145–52.
65. Dhainaut F, Pietrzyk S, Granger P. Kinetic investigation of the NO reduction by H2 over noble metal based catalysts. Catalysis Today. 2007 Jan 15;119(1–4):94–9.
66. Salaün M, Kouakou A, da Costa S, da Costa P. Synthetic gas bench study of a natural gas vehicle commercial catalyst in monolithic form: On the effect of gas composition. Applied Catalysis B: Environmental. 2009 May 20;88(3–4):386–97.
67. Monai M, Montini T, Gorte RJ, Fornasiero P. Catalytic Oxidation of Methane: Pd and Beyond. Vol. 2018, European Journal of Inorganic Chemistry. Wiley-VCH Verlag; 2018. p. 2884–93.
68. Marques R, Capela S, da Costa S, Delacroix F, Djéga-Mariadassou G, da Costa P. Methane oxidation by NO and O2 from reverse spillover on alumina supported palladium catalysts. Catalysis Communications. 2008 Apr 20;9(8):1704–8.
69. Ren Y, Lou D, Tan P, Zhang Y, Sun X. Emission reduction characteristics of after-treatment system on natural gas engine: Effects of platinum group metal loadings and ratios. Journal of Cleaner Production. 2021 May 20;298.

70. ’Sakai T’ ’Choi, B-C ’Osuga, R ’Ko, Y. Purification Characteristics of Catalytic Converters for Natural Gas Fueled Automotive Engine. SAE Tech. 1991;
71. Trivedi S, Prasad R, Mishra A, Kalam A, Yadav P. Current scenario of CNG vehicular pollution and their possible abatement technologies: an overview. Available from: https://doi.org/10.1007/s11356-020-10361-7
72. Chen J, Wu Y, Hu W, Qu P, Zhang G, Jiao Y, et al. Evolution of Pd Species for the Conversion of Methane under Operation Conditions. Industrial and Engineering Chemistry Research. 2019 Apr 24;58(16):6255–65.
73. Bogarra M, Herreros JM, Hergueta C, Tsolakis A, York APE, Millington PJ. Influence of three-way catalyst on gaseous and particulate matter emissions during gasoline direct injection engine cold-start. Johnson Matthey Technology Review. 2017 Oct 1;61(4):329–41.
74. Rusu AO, Dumitriu E. DESTRUCTION OF VOLATILE ORGANIC COMPOUNDS BY CATALYTIC OXIDATION [Internet]. Vol. 2, Environmental Engineering and Management Journal. 2003. Available from: http://omicron.ch.tuiasi.ro/EEMJ/
75. Pradhan S, Thiruvengadam A, Thiruvengadam P, Demirgok B, Besch M, Carder D, et al. Development of an Ammonia Reduction Aftertreatment Systems for Stoichiometric Natural Gas Engines. Source: SAE International Journal of Engines [Internet]. 2017;10(1):104–9. Available from: https://www.jstor.org/stable/10.2307/26285018?seq=1&cid=pdf-
76. Zhang Q, Li M, Shao S, Li G. Ammonia emissions of a natural gas engine at the stoichiometric operation with TWC. Applied Thermal Engineering. 2018 Feb 5;130:1363–72.
77. Suarez-Bertoa R, Zardini AA, Astorga C. Ammonia exhaust emissions from spark ignition vehicles over the New European Driving Cycle. Atmospheric Environment. 2014 Nov 1;97:43–53.
78. Oh SH, Triplett T. Reaction pathways and mechanism for ammonia formation and removal over palladium-based three-way catalysts: Multiple roles of CO. Catalysis Today. 2014 Aug 1;231:22–32.

79. Ramanathan K, Sharma CS, Kim CH. Global kinetics for ammonia formation and oxidation reactions in a commercial three-way catalyst. Industrial and Engineering Chemistry Research. 2012 Jan 25;51(3):1198–208.
80. Teixeira Malaquias, A., da Costa, R.B., Netto, N.A., Coronado, C.J., & Baêta, J.G. (2021). A review of dual-fuel combustion mode in spark-ignition engines. Journal of the Brazilian Society of Mechanical Sciences and Engineering.
81. Singh, E., Morganti, K., & Dibble, R. (2019). Dual-fuel operation of gasoline and natural gas in a turbocharged engine. Fuel, 237, 694-706. doi: 10.1016/j.fuel.2018.09.158
82. Zhang, P.; Ni, J.; Shi, X.; Yin, S.; Zhang, D. Effects of Ignition Timing on Combustion Characteristics of a Gasoline Direct Injection Engine with Added Compressed Natural Gas under Partial Load Conditions. Processes 2021, 9, 755. https://doi.org/ 10.3390/pr9050755
83. Sarabi, M., Abdi Aghdam, E. Experimental analysis of in-cylinder combustion characteristics and exhaust gas emissions of gasoline–natural gas dual-fuel combinations in a SI engine. *J Therm Anal Calorim* **139**, 3165–3178 (2020). https://doi.org/10.1007/s10973-019-08727-2
84. Lee, J., Park, C., Bae, J., Kim, Y., Lee, S., & Kim, C. (2020). Comparison between gasoline direct injection and compressed natural gas port fuel injection under maximum load condition. Energy, 197, 117173.
85. Xu, Y., Zhang, Y., Gong, J., Su, S., & Wei, Z. (2020). Combustion behaviours and emission characteristics of a retrofitted NG/gasoline duel-fuel SI engine with various proportions of NG-gasoline blends. *Fuel*, *266*, 116957. doi: 10.1016/j.fuel.2019.116957
86. Zhao, Z., Huang, Y., Yu, X., Guo, Z., Yu, L., & Li, D. (2021). Experimental Study on Combustion and Emission of an Si Engine with Natural Gas/ Ethanol Combined Injection. *SSRN Electronic Journal*. doi: 10.2139/ssrn.3981397
87. Liu, Z., Yu, X., Sun, P., & Xu, S. (2021). Experimental investigation of the performance and emissions of a dual-injection SI engine with natural gas direct injection plus gasoline port injection under lean-burn conditions. *Fuel*, *300*, 120952. doi: 10.1016/j.fuel.2021.120952

88. Wang, M., Dimopoulos Eggenschwiler, P., Franken, T., Agote-Arán, M., Ferri, D., & Kröcher, O. (2022). Investigation on the Role of Pd, Pt, Rh in Methane Abatement for Heavy Duty Applications. *Catalysts*, *12*(4), 373. doi: 10.3390/catal12040373

89. Ren, Y., Lou, D., Tan, P., Zhang, Y., & Sun, X. (2021). Emission reduction characteristics of after-treatment system on natural gas engine: Effects of platinum group metal loadings and ratios. *Journal Of Cleaner Production*, *298*, 126833. doi: 10.1016/j.jclepro.2021.126833

90. Wang, M., Dimopoulos Eggenschwiler, P., Franken, T., Ferri, D., & Kröcher, O. (2021). Reaction pathways of methane abatement in Pd-Rh three-way catalyst in heavy duty applications: A combined approach based on exhaust analysis, model gas reactor and DRIFTS measurements. *Chemical Engineering Journal*, *422*, 129932. doi: 10.1016/j.cej.2021.129932

91. Ferri, D., Elsener, M., & Kröcher, O. (2018). Methane oxidation over a honeycomb Pd-only three-way catalyst under static and periodic operation. *Applied Catalysis B: Environmental*, *220*, 67-77. doi: 10.1016/j.apcatb.2017.07.070

92. Gremminger, A., Pihl, J., Casapu, M., Grunwaldt, J., Toops, T., & Deutschmann, O. (2020). PGM based catalysts for exhaust-gas after-treatment under typical diesel, gasoline and gas engine conditions with focus on methane and formaldehyde oxidation. *Applied Catalysis B: Environmental*, *265*, 118571. doi: 10.1016/j.apcatb.2019.118571

93. Cooper, J., & Beecham, J. (2013). A Study of Platinum Group Metals in Three-Way Autocatalysts. *Platinum Metals Review*, *57*(4), 281-288. doi: 10.1595/147106713x671457

94. David B. Kittelson (1998). Engines and nanoparticles: a review. Journal of Aerosol Science, Volume 29, Issues 5–6, Pages 575-588, ISSN 0021-8502, https://doi.org/10.1016/S0021-8502(97)10037-4.

95. Catapano, F., Di Iorio, S., Sementa, P., & Vaglieco, B. (2022). Particle Formation and Emissions in an Optical Small Displacement SI Engine Dual Fueled with CNG DI and Gasoline PFI. SAE Technical Paper 2017-24-0092, 2017, https://doi.org/10.4271/2017-24-0092.

96. Alanen, J., Saukko, E., Lehtoranta, K., Murtonen, T., Timonen, H., & Hillamo, R. et al. (2015). The formation and physical properties of the particle emissions from a natural gas engine. *Fuel*, *162*, 155-161. doi: 10.1016/j.fuel.2015.09.003

97. Nithyanandan, K., Lin, Y., Donahue, R., Meng, X., Zhang, J., & Lee, C. (2016). Characterization of soot from diesel-CNG dual-fuel combustion in a CI engine. *Fuel*, *184*, 145-152. doi: 10.1016/j.fuel.2016.06.028

98. Gaddam, C., Huang, C., & Vander Wal, R. (2016). Quantification of nano-scale carbon structure by HRTEM and lattice fringe analysis. *Pattern Recognition Letters*, *76*, 90-97. doi: 10.1016/j.patrec.2015.08.028

99. Mc Grane, L., Douglas, R., Irwin, K., Woods, A., Stewart, J., Pedlow, A., Elliott, M. (2021). Oxygen Storage Capacity (OSC) Measurement of 3-Way Automotive Catalysts Using the CATAGEN OMEGA Test Reactor. SAE Technical paper, DOI: https://doi.org/10.4271/2021-24-0083.

100. Zhou, Z., Harold, M., & Luss, D. (2019). NOx reduction on Ceria: Impact of lean-rich cycling. *Applied Catalysis B: Environmental*, *240*, 79-91. doi: 10.1016/j.apcatb.2018.08.050

101. Guillén-Hurtado, N., Rico-Pérez, V., García-García, A., Lozano-Castelló, D., & Bueno-López, A. (2012). THREE-WAY CATALYSTS: PAST, PRESENT AND FUTURE. *Dyna*, *79*, 114-121.

102. Potenza M, Milanese M, de Risi A. Effect of injection strategies on particulate matter structures of a turbocharged GDI engine. Fuel. 2019 Feb 1;237:413–28.

103. Benajes J, García A, Monsalve-Serrano J, Boronat V. Gaseous emissions, and particle size distribution of dual-mode dual-fuel diesel-gasoline concept from low to full load. Appl Therm Eng. 2017 Jun;120:138–49.

104. Bogarra M, Herreros JM, Tsolakis A, York APE, Millington PJ, Martos FJ. Impact of exhaust gas fuel reforming and exhaust gas recirculation on particulate matter morphology in Gasoline Direct Injection Engine. J Aerosol Sci. 2017 Jan;103:1–14.

105. Heywood J. Internal Combustion Engine Fundamentals. New York: McGraw-Hill Education; 1988. 960 p.

106. Eastwood P. Particulate Emissions from Vehicles [Internet]. Chichester, UK: John Wiley & Sons, Ltd; 2007 [cited 2019 Apr 9]. (Wiley-Professional Engineering Publishing Series). Available from: http://doi.wiley.com/10.1002/9780470986516

107. Luo Y, Zhu L, Fang J, Zhuang Z, Guan C, Xia C, et al. Size distribution, chemical composition, and oxidation reactivity of particulate matter from gasoline direct injection (GDI) engine fueled with ethanol-gasoline fuel. Appl Therm Eng. 2015 Oct;89:647–55.

108. Climate Action. 2022. CO_2 emission performance standards for cars and vans. [online] Available at: <https://ec.europa.eu/clima/eu-action/transport-emissions/road-transport-reducing-co2-emissions-vehicles/co2-emission-performance-standards-cars-and-vans_en> [Accessed 7 June 2022].

109. Alanen J, Saukko E, Lehtoranta K, Murtonen T, Timonen H, Hillamo R, et al. The formation and physical properties of the particle emissions from a natural gas engine. Fuel. 2015 Dec;162:155–61.

110. Lehtinen KEJ, Zachariah MR. Energy accumulation in nanoparticle collision and coalescence processes. J Aerosol Sci. 2002 Feb;33(2):357–68.

111. Korakianitis T, Namasivayam AM, Crookes RJ. Natural-gas fueled spark-ignition (SI) and compression-ignition (CI) engine performance and emissions. Prog Energy Combust Sci. 2011 Feb;37(1):89–112.

112. Tahir MMohd, Ali MS, Salim MA, Bakar RA, Fudhail AM, Hassan MZ, et al. Performance Analysis of A Spark Ignition Engine Using Compressed Natural Gas (CNG) as Fuel. Energy Procedia. 2015 Apr;68:355–62.

113. Wahbi A, Tsolakis A, Herreros J. Emissions Control Technologies for Natural Gas Engines. In Energy, Environment, and Sustainability; 2019. p. 359–79.

114. Theicct.org. 2022. [online] Available at: <https://theicct.org/sites/default/files/publications/ICCT_Euro6-VI_briefing_jun2016.pdf> [Accessed 7 June 2022].

115. Singh E, Morganti K, Dibble R. Dual-fuel operation of gasoline and natural gas in a turbocharged engine. Fuel. 2019 Feb;237:694–706.

116. Momeni Movahed M, Basirat Tabrizi H, Mirsalim M. Experimental investigation of the concomitant injection of gasoline and CNG in a turbocharged spark ignition engine. Energy Convers Manag. 2014 Apr;80:126–36.

117. Pipitone E, Beccari S. PERFORMANCES IMPROVEMENT OF A S. I. CNG BI-FUEL ENGINE BY MEANS OF DOUBLE-FUEL INJECTION. In 2009 [cited 2019 Apr 9]. p. 2009-24–0058. Available from: http://papers.sae.org/2009-24-0058/

118. Delpech V, Obiols J, Soleri D, Mispreuve L, Magere E, Kermarrec S. Towards an Innovative Combination of Natural Gas and Liquid Fuel Injection in Spark Ignition Engines. SAE Int J Fuels Lubr. 2010 May 5;3(2):196–209.

119. Obiols J, Soleri D, Dioc N, Moreau M. Potential of Concomitant Injection of CNG and Gasoline on a 1.6L Gasoline Direct Injection Turbocharged Engine. In 2011 [cited 2019 Apr 9]. p. 2011-01–1995. Available from: http://papers.sae.org/2011-01-1995/

120. Tabar AR, Hamidi AA, Ghadamian H. Experimental investigation of CNG and gasoline fuels combination on a 1.7 L bi-fuel turbocharged engine. Int J Energy Environ Eng. 2017 Mar;8(1):37–45.

121. Una Trivanovic, Joel C. Corbin, Alberto Baldelli, Weihan Peng, Jiacheng Yang, Patrick Kirchen, J. Wayne Miller, Prem Lobo, Stéphanie Gagné, Steven N. Rogak. Size and morphology of soot produced by a dual-fuel marine engine. Journal of Aerosol Science, Volume 138, December 2019, Pages 105448

122. Hergueta C, Bogarra M, Tsolakis A, Essa K, Herreros JM. Butanol-gasoline blend and exhaust gas recirculation, impact on GDI engine emissions. Fuel. 2017 Nov;208:662–72.

123. Serhan N, Tsolakis A, Martos FJ. Effect of propylene glycol ether fuelling on the different physico-chemical properties of the emitted particulate matters: Implications of the soot reactivity. Fuel. 2018 May;219:1–11.

124. Serhan N, Tsolakis A, Wahbi A, Martos FJ, Golunski S. Modifying catalytically the soot morphology and nanostructure in diesel exhaust: Influence of silver De-NOx catalyst (Ag/Al2O3). Appl Catal B Environ. 2019 Feb;241:471–82.

125. An Y, Teng S, Pei Y, Qin J, Li X, Zhao H. An experimental study of polycyclic aromatic hydrocarbons and soot emissions from a GDI engine fueled with commercial gasoline. Fuel. 2016 Jan;164:160–71.

126. Nithyanandan K, Lin Y, Donahue R, Meng X, Zhang J, Lee CF. Characterization of soot from diesel-CNG dual-fuel combustion in a CI engine. Fuel. 2016 Nov;184:145–52.

127. Seong HJ, Boehman AL. Evaluation of Raman Parameters Using Visible Raman Microscopy for Soot Oxidative Reactivity. Energy Fuels. 2013 Mar 21;27(3):1613–24.

128. Ess MN, Ferry D, Kireeva ED, Niessner R, Ouf F-X, Ivleva NP. In situ Raman microspectroscopic analysis of soot samples with different organic carbon content: Structural changes during heating. Carbon. 2016 Aug;105:572–85.

129. Nirendra N. Mustafi & Robert R. Raine (2009) Electron Microscopy Investigation of Particulate Matter from a Dual Fuel Engine, Aerosol Science and Technology, 43:9,951-960, DOI: 10.1080/02786820903067210

130. Bogarra-Macias, M., Herreros-Arellano, J., Tsolakis, A., York, A. et al., "Reformate Exhaust Gas Recirculation (REGR) Effect on Particulate Matter (PM), Soot Oxidation and Three Way Catalyst (TWC) Performance in Gasoline Direct Injection (GDI) Engines," SAE Int. J. Engines 9(1):2016, doi:10.4271/2015-01-2019.

131. M. Bogarra, J.M. Herreros, A. Tsolakis,, A.P.E. York, P.J. Millington, F.J. Martos. Influence of on-board produced hydrogen and three way catalyst on soot nanostructure in Gasoline Direct Injection engines. Carbon, Volume 120, 2017, Pages 326-336, ISSN 0008-6223, https://doi.org/10.1016/j.carbon.2017.05.049.

132. Hergueta C, Tsolakis A, Herreros JM, Bogarra M, Price E, Simmance K, et al. Impact of bio-alcohol fuels combustion on particulate matter morphology from efficient gasoline direct injection engines. Appl Energy. 2018 Nov;230:794–802.

133. Lee KO, Seong H, Sakai S, Hageman M, Rothamer D. Detailed Morphological Properties of Nanoparticles from Gasoline Direct Injection Engine Combustion of Ethanol Blends. In 2013 [cited 2019 Apr 9]. p. 2013-24–0185. Available from: http://papers.sae.org/2013-24-0185/

134. Distaso E, Amirante R, Tamburrano P, Reitz RD. Steady-state Characterization of Particle Number Emissions from a Heavy-Duty Euro VI Engine Fueled with Compressed Natural Gas. Energy Procedia. 2018 Aug;148:671–8.

135. Mühlbauer W, Zöllner C, Lehmann S, Lorenz S, Brüggemann D. Correlations between physicochemical properties of emitted diesel particulate matter and its reactivity. Combust Flame. 2016 May;167:39–51.

136. C.K. Gaddam, R.L. Vander Wal, Physical and chemical characterization of SIDI engine particulates, Combust. Flame 160 (11) (2013) 2517e2528.

137. Chen H, He J, Zhong X. Engine combustion and emission fuelled with natural gas: A review. J Energy Inst. 2018 Jun;S1743967118304446.

138. Jahirul MI, Masjuki HH, Saidur R, Kalam MA, Jayed MH, Wazed MA. Comparative engine performance and emission analysis of CNG and gasoline in a retrofitted car engine. Appl Therm Eng. 2010 Oct;30(14–15):2219–26.

139. Tree DR, Svensson KI. Soot processes in compression ignition engines. Prog Energy Combust Sci. 2007 Jun;33(3):272–309.

140. Pan J, Li N, Wei H, Hua J, Shu G. Experimental investigations on combustion acceleration behavior of methane/gasoline under partial load conditions of SI engines. Appl Therm Eng. 2018 Jul;139:432–44.

141. Karavalakis G, Durbin TD, Villela M, Miller JW. Air pollutant emissions of light-duty vehicles operating on various natural gas compositions. J Nat Gas Sci Eng. 2012 Jan;4:8–16.

142. Barone TL, Storey JME, Youngquist AD, Szybist JP. An analysis of direct-injection spark-ignition (DISI) soot morphology. Atmos Environ. 2012 Mar;49:268–74.

143. Lapuerta M, Martos FJ, Herreros JM. Effect of engine operating conditions on the size of primary particles composing diesel soot agglomerates. J Aerosol Sci. 2007 Apr;38(4):455–66.

144. Neer A, Koylu U. Effect of operating conditions on the size, morphology, and concentration of submicrometer particulates emitted from a diesel engine. Combust Flame. 2006 Jul;146(1–2):142–54.

145. Constantine MM, Richard AD. Comparison of Soot Growth and Oxidation in Smoking and Non–Smoking Ethylene Diffusion Flames. Combust Sci Technol. 1989 Jul 1;66(1–3):1–16

146. Armas O, Gómez A, Herreros JM. Uncertainties in the determination of particle size distributions using a mini tunnel–SMPS system during Diesel engine testing. Meas Sci Technol. 2007 Jul 1;18(7):2121–30.

147. Martos FJ, Martín-González G, Herreros JM. Semi-empirical model for indirect measurement of soot size distributions in compression ignition engines. Measurement. 2018 Aug;124:32–9.

148. Meakin P, Donn B, Mulholland GW. Collisions between point masses and fractal aggregates. Langmuir. 1989 Mar;5(2):510–8.

149. Lapuerta M, Ballesteros R, Martos FJ. A method to determine the fractal dimension of diesel soot agglomerates. J Colloid Interface Sci. 2006 Nov;303(1):149–58

150. Maricq MM. Coagulation dynamics of fractal-like soot aggregates. J Aerosol Sci. 2007 Feb;38(2):141–56.

151. Seong, H., Lee, K., and Choi, S., "Effects of Engine Operating Parameters on Morphology of Particulates from a Gasoline Direct Injection (GDI) Engine," SAE Technical Paper 2013-01-2574, 2013, https://doi.org/10.4271/2013-01-2574.

152. Song J, Alam M, Boehman A, Kim U. Examination of the oxidation behavior of biodiesel soot. Combust Flame. 2006 Sep;146(4):589–604.